Doctoral Dissertation

Studies on Lightning IC/CG Ratio and Effects of Lightning and Rainfall Currents on Global Electric Circuit

雷放電の IC/CG 比及びグローバルサーキットへの雷・降雨電流の影響に関する研究

Bandholnopparat Kittanapat

Graduate School of Science, Hokkaido University

Department of Cosmosciences

March 2020

The dissertation of Bandholnopparat Kittanapat is approved by the examination committee.

Supervisor: Dr. Sato Mitsuteru

Committee Chairperson: Professor Takahashi Yukihiro

Committee Member: Professor Kuramoto Kiyoshi

Committee Member: Professor Ishiwatari Masaki

Abstract

The ratio of intracloud (IC) discharges to cloud-to-ground (CG) discharges, which is denoted by Z-value, is one of the key parameters in the lightning physics because it has close relation to the climatological difference in the thundercloud formation and structure in the tropical, subtropical and temperature regions and because it is one of the major parameters for the quantitative evaluation of lightning contributions to the global electric circuit (GEC). However, the latitudinal, regional and seasonal dependences of Z-value are not fully clarified so far. In order to estimate the effects of lightning and rainfall currents on GEC, a simple 2D model was developed in the previous study. However, it only treats the extremely simplified input parameters, such as constant lightning and rainfall currents and constant atmospheric conductivity, with relatively low temporal and spatial resolutions. The purpose of this dissertation is to estimate more statistically reliable Z-value and its latitudinal, regional and seasonal dependences and to quantitatively evaluate the effects of lightning and rainfall currents on GEC with more appropriate input parameters and with more high temporal and spatial resolutions. For this purpose, firstly, we have developed new methods to classify IC, positive CG (+CG) discharges, and negative CG (-CG) discharges using the lightning optical data obtained by the Global Lightning and Sprite Measurements on Japanese Experiment Module (JEM-GLIMS) mission and ground-based lightning data. Secondly, we have estimated Z-value and its latitudinal, regional, and seasonal dependences. Finally, we have quantitatively evaluated the contribution of lightning and rainfall currents to GEC using newly developed 3D GEC model. In this study, a

total of 8354 JEM-GLIMS lightning events detected in the period from November 2012 to August 2015 are analyzed. These lightning events are first classified into the three discharge types,*i.e.*, IC, -CG, and +CG discharges by compared to the ground-based lightning data provided by the JLDN, NLDN, WWLLN, and GEON. Then, the identified discharge events are used to estimate Z-value, and we have first estimated its latitudinal, regional and seasonal dependences. It is found that the Z-ratio in the continental region is slightly higher than that in the oceanic region. The average of Z-ratio over continental and oceanic region are 1.7 and 1.1, respectively. In addition, the averaged Z-value in the local summer season (1.2) is higher than that in the local winter season (0.6). The latitudinal dependence of the Z-value estimated in this study shows a good agreement with the results shown in the previous studies. The estimated Z-ratio varies in the range of 2.9 - 0.19 from the equator to 50° latitude, and the global mean value is 1.6. As a next step, we have developed a new 3D GEC model, which can calculate atmospheric electric field with 5 min time resolution and $0.2^\circ \times 0.2^\circ$ spatial resolution. In this model, lightning and rainfall activities are regarded as the electric current generator. In addition, this model uses the input parameters of time-variable lightning and rainfall activities and time-variable column resistance and associated atmospheric conductivity. First, the regional dependence of Z-ratio derived from this study is applied to the CG lightning data provided by the WWLLN network in order to estimate the occurrence number of IC discharges. Then, the estimated occurrence number of IC and CG discharges and the precipitation data obtained by the global precipitation measurement (GPM) project are used for the 3D GEC model. Finally, the total upward current from thunderclouds to the ionosphere is calculated. It is found that the average lightning and precipitation currents in the GEC are estimated to be ∼70 A ($\sim 6\%$) and ∼1080 A ($\sim 94\%$), respectively. We have also compared the fair weather electric field predicted by the GEC model to that observed at Syowa station in Antarctica and Reading station in UK. It is found that the absolute amplitude of the fair weather electric field estimated by

the model is comparable to that observed at Syowa and Reading stations. It is also found that the diurnal variation of the fair weather electric field estimated by the model is well correlated with that observed at the two stations. We found that the regional dependence of Z-value obtained by the combination of the ground-based and space-based observations greatly contributes to more accurate estimation of the total lightning and rainfall currents in the GEC. It is first quantitatively presented that the upward current from thundercloud to the ionosphere generated by lightning activities is only 6% and that the rainfall activity play a crucial role in the GEC.

Acknowledgements

First of all, I would like to express my sincere gratitude to my advisor Dr. Mitsuteru Sato for the continuous support of my Ph.D study and related research, for his patience, motivation, and immense knowledge. His guidance helped me in all the time of research and writing of this dissertation. I could not have imagined having a better advisor and mentor for my Ph.D study.

Besides my advisor, I would like to thank the rest of my dissertation committee: Prof. Yukihiro Takahashi, Prof.Kiyoshi Kuramoto, and Prof. Masaki Ishiwatari, for their insightful comments and encouragement, but also for the hard question which incented me to widen my research from various perspectives.

I would like to thank Professor Akira Kadokura, Dr. Yasuhiro Minamoto, and all staff at the Syowa station for providing the fair weather electric field at Syowa station, and giving me good comments for my work. I also would like to thank Associate Professor Dr. Keri Nicoll and all of the staff at Reading university atmospheric observatory for providing the fair weather electric field at Reading, The United Kingdom.

I thank all of the EP, PSG staffs and students for your comments and suggestion in my work.

Last but not the least, I would like to thank my family for supporting me spiritually throughout writing this thesis and my life in general.

This work was supported by JSPS KAKENHI Grant-in-Aid for Scientific Research (B) Number 16H04055 and 24340117,MEXT KAKENHI Grant- in-Aid for Specially Promoted Research Number 19002002, and the Rajamangala University of Technology Thanyaburi.

Contents

Abstract iii

Acknowledgements vi

List of Figures viii

List of Table xvi

1 Introduction 1

1.1 Lightning discharges 1

1.2 Ratio between intracloud and cloud-to-ground discharges 3

1.3 Global Electric Circuit 5

1.4 Limitation of the previous studies and the Purposes of this study 10

2 Estimation of the ratio between intracloud discharges and cloud-to-ground discharges 12

2.1 Satellite-based lightning data 12

2.2 Ground-based lightning data 15

2.2.1 Japanese Lightning Detection Network 15

2.2.2 National Lightning Detection Network 16

2.2.3 World Wide Lightning Location Network 16

2.2.4 Global ELF Observation Network 17

2.3 Estimation of the ratio between intracloud versus cloud-to-ground discharges 18

3 Regional, Seasonal, and Latitudinal dependences of Z-ratio 26
3.1 Example of -CG, +CG and IC discharge 26
3.1.1 Example of -CG discharge 26
3.1.2 Example of +CG discharge 30
3.1.3 Example of IC discharge 33
3.2 PH intensity ratio and LSI intensity ratio of lightning discharges . 36
3.3 Regional Dependence of Z-ratio 40
3.4 Seasonal Dependence of Z-ratio 43
3.5 Latitudinal Dependence of Z-ratio 46
3.6 Relationship between Z-ratio and +CG discharges 49

4 The 3-dimensional model of the global electric circuit 51
4.1 Calculation of the upward electric current by lightning discharges 51
4.2 Calculation of the upward electric current by rainfall 55
4.3 Calculation of the fair weather resistance 57

5 Contribution of lightning and rainfall to the global electric circuit 61
5.1 Calculation of the fair weather electric field on May 17, 2013 . . . 61
5.2 Calculation of the fair weather electric field on March 16, 2014 . . 67
5.3 Contribution of lightning to the global electric circuit 74
5.4 Contribution of rainfall to the global electric circuit 77
5.5 Fair-weather resistance 79
5.6 Simulation of a fair-weather electric field 80

6 Summary 89

A The absolute intensity of LSI image 91

B Lightning Detection Efficiency of JEM-GLIMS 95

List of Figures

1.1 Common type of lightning discharges are the IC, +CG, and -CG discharge. 2

1.2 Previous ensemble observations of regional Z-ratio and its inferred dependence on latitude (Boccippio et al., 1999) 4

1.3 Schematic diagram showing the upward electric current to the ionosphere generated by thunderstorms and electrified rain/shower clouds in the global electric circuit. 6

1.4 Potential gradient of the fair weather electric field measured by Carnegie Cruise III (points). The dotted line is a fitted line from the data. The greyed area is the standard errors (Harrison, 2005). 7

1.5 Circuit diagram of the global electric circuit (Rycroft et al., 2007). In this circuit, thunderstorms and electrified rain/shower clouds are the main currents generators. 8

1.6 Electric conductivity profile of the air ($\sigma(z)$) for calculating the values of resistance in the global electric circuit (Rycroft et al., 2007). 9

2.1 JEM-GLIMS optical instruments (PHs and LSI) and electromagnetic waves receiver (VLFR) (Sato, 2015). 13

2.2 Global distribution of the 8354 lightning events detected by JEM-GLIMS between November 2012 and August 2015. 15

2.3 Flow chart showing how the discharge type of JEM-GLIMS lightning events were classified into IC, -CG, +CG, ambiguous flash using the ground-based lightning data. 19
2.4 Schematic illustration showing the field of view of PHs and a distance between JEM-GLIMS nadir point and a ground-based lightning event (D) 20
2.5 Electromagnetic waves obtained by orthogonal search coil for identifying the polarity of lightning discharge. 21
2.6 Model of atmospheric transmittance in the wavelength range of 200-1000 nm calculated by the MODTRAN code. The blue, green and red lines show the transmittance from a light source located at the 4, 8, and 12 km altitude to the zenith direction, respectively. . 23
2.7 The difference of the altitude of IC, +CG, and -CG discharge channel that might be used for classify the discharge types. 24

3.1 (a) -CG Lightning event detected by JEM-GLIMS optical instruments at 20:15:48.80348 UT on 24 March 2014. Figure (b) and (c), plot of the ELF magnetic field waveform data acquired at Syowa and Kuju station, respectively. 27
3.2 Electromagnetic waves signal on H-component and D-component for considering the polarity of CG event of Figure 3.1. 28
3.3 An example of (a) lightning discharge image on LSI-1(b) Same as (a) except for LSI-2.Figure (c) and (d) is the plot of raw count for each y-pixel for LSI-1 and LSI-2. 29
3.4 (a) Positive cloud-to-ground lightning event detected by JEM-GLIMS optical instruments 03:25:22.383 UT on September 13, 2014. Figure (b) and (c), plot of the ELF magnetic field waveform data acquired at Syowa and Kuju station, respectively. 31

3.5 Electromagnetic waves signal on H-component and D-component for considering the polarity of CG event of Figure 3.4. 32
3.6 An example of (a) lightning discharge image on LSI-1(b) Same as (a) except for LSI-2.Figure (c) and (d) is the plot of raw count for each y-pixel for LSI-1 and LSI-2. 33
3.7 (a) IC Lightning event detected by JEM-GLIMS optical instruments at 08:10:46.352 UT on 12 March 2014. Figure (c) – (d), plot of the ELF magnetic field waveform data acquired at Syowa and Kuju station, respectively. 34
3.8 An example of (a) lightning discharge image on LSI-1(b) Same as (a) except for LSI-2.Figure (c) and (d) is the plot of raw count for each y-pixel for LSI-1 and LSI-2. 35
3.9 Histograms of the PH intensity ratios with the logarithmic scale. The blue, red and green bars correspond to the ratio of IC, +CG, and -CG discharges, respectively. In this figure, (a)-(f) are the ratios of PH2/PH3, PH5/PH3, PH6/PH3, PH2/PH4, PH5/PH4, and PH6/PH4, respectively. 37
3.10 Histograms of the LSI intensity ratio of 45 IC (blue), 12 +CG (red), and 17 -CG (green) discharges. 38
3.11 Global distribution of the identified IC, +CG,and (c) -CG discharges detected by JEM-GLIMS in the period from November 2012 – August 2015 41
3.12 Spatial distribution of the Z-ratio over the latitudinal range of $\pm 51^{\circ}$ used for calculating the occurrence number of IC discharges . . . 43
3.13 Spatial distribution of the Z-ratio in the period of (a) December-February, (b) March-May, (c) June-August, and (d) September-November, respectively. 45

3.14 Latitudinal dependences of the Z-ratio in the northern hemisphere. (b) Same as (a) except for the southern hemisphere. In these figures, the zonal-mean Z-ratio values are calculated every 3° latitudinal range and plotted. Vertical bars at each data point represent the $\pm 1\sigma$ of Z-ratio values 47

3.15 Scatter plot of the estimated Z-ratio and the occurrence percentage of (a) IC discharges, (b) +CG discharges, and (c) -CG discharges, respectively. 50

4.1 (a) Flow chart showing how the input parameters of the global electric circuit were calculated using CG lightning data provided by WWLLN, rainfall data provided by GPM, and the average column resistance map 52

4.2 (a) The occurrence number of CG discharges provided by WWLLM were composited into a $0.2° \times 0.2°$ cell for estimating the occurrence number of +CG, -CG, and IC lightning. (b)The relative detection efficiency of WWLLN. Stations are shown as triangles with operational stations in white, non-operational in black, and operational for part of the day in grey (Hutchins et al., 2012). 54

4.3 Example of the rainfall data provided by the GPM on June 4, 2014, which was used to calculate the upward electric current to the ionosphere. 56

4.4 Schematic diagram of the three resistors in the generator cell. The accompanying resistance are R_A, R_T, and R_B represent the resistance between cloud-top and the ionosphere, the resistance of the thunderstorm, and the resistance between the cloud-based and the ground, respectively. 58

4.5 Average column resistance map that was used for calculating the fair-weather resistance (Baumgaertner et al., 2013). 59

4.6 The 3-dimensional model that was used to estimated the fair-weather field. 60

5.1 (a) Occurrence number of lightning around the world on March 16, 2014. (b) Electric current generated by +IC(blue), -IC(purple), +CG(red), and -CG(green) lightning. 62

5.2 (a) Rainfall over continental, oceanic, and global which calculated from the GPM on May 17, 2013 (b) Electric current from rainfall which calculated from the precipitation data in Figure 5.2(a). . . 64

5.3 Fair weather resistance on May 17, 2013, calculated from the average column resistance. 65

5.4 (a)Comparison between the estimated fair-weather electric field and the observed fair-weather electric field at the Syowa station on May 17, 2013. (b) similar to (a) but for at the Kakioka station. 66

5.5 (a) The number of +IC(blue), -IC(purple), +CG(red), and -CG(green) lightning around the world on March 16, 2014. (b) Electric current generated by +IC(blue), -IC(purple), +CG(red), and -CG(green) lightning. 68

5.6 (a) Rainfall over land, ocean, and global which calculated from the GPM on March 16, 2014 (b) Electric current from rainfall which calculated from the precipitation data in Figure 5.6(a). 70

5.7 (a) Fair weather resistance on March 16, 2014, calculated from the average column resistance. 71

5.8 Comparison between the estimated fair-weather electric field and the observed fair-weather electric field at the Syowa station on March 16, 2014. 73

5.9 (a) Lightning flashes as a function of UTC. (b) The estimated lightning current as a function of UTC. The $\pm 1\sigma$ values are indicated in Gray area. 76

5.10 (a) The average of global rainfall over continental and oceanic areas. (b) The comparison between the Carnegie curve (gray curve) and the diurnal variations of total rainfall (black solid) over land (dashed) and over ocean (dotted). (c) Upward electric currents generated by global rainfall calculated from Figure 5.10(a). 78
5.11 Diurnal variations of total global resistance. The black line shows the mean value, and the gray area presents the $\pm 1\sigma$. 79
5.12 Comparison between the estimated fair-weather electric filed (black dot) and observed fair-weather electric filed (red, green, and blue) at the Syowa Station. The red, blue, and green lines in the Figure represents the observed fair-weather electric fields obtain from Sensor 1, 2, and 3 respectively. 81
5.13 Average of the estimated fair weather electric field at Syowa station. The average E_{ZE} in this Figure calculated using the data as shown in Figure 5.12. 82
5.14 Comparison between the estimated fair-weather electric filed (black dot) and observed fair-weather electric filed (blue line) at the Reading Station, located in the United Kingdom. 84
5.15 Average of the estimated fair weather electric field at Reading station. The average E_{ZE} in this Figure calculated using the data as shown in Figure 5.14. 85
5.16 Comparison between the estimated fair weather electric filed (black dot) and observed fair weather electric filed (blue line) at the Kakioka Station, Japan. 87
5.17 Average of the estimated fair weather electric field at Reading station. The average E_{ZE} in this Figure calculated using the data as shown in Figure 5.16. 88

A.1 Schimetic diagram for calibrating the LSI-1 and LSI-2 cameras. . 91

A.2 The variation of the absolute and relative intensities for (a) LSI-1 and (b) LSI-2) Bandholnopparat et al. (2019). 93

B.1 Optical energy distribution of lightning events detected by JEM-GLIMS optical instruments in the wavelength range of 400 - 1000 nm. 96

B.2 Optical energy distribution of lightning events detected by JEM-GLIMS optical instruments in the wavelength range of 400 - 1000 nm. 98

List of Tables

2.1 JEM-GLIMS optical instruments 14

2.2 Electromagnetic waves signal in D and H component for considering the polarity of CG discharge. 22

3.1 Summary of the PH and LSI intensity ratios of 75 IC, 102 +CG, and 394 -CG discharges. In this table, the median value of the logarithmic PH and LSI intensity ratios and the standard deviation (σ) are listed. 39

3.2 Comparison between the Z-ratios derived from this study and the previous studies. 48

4.1 The input parameters for calculating the upward current to the ionosphere by lightning discharges. 55

5.1 Selected date for estimating the fair weather electric field. 75

A.1 Absolute intensity from a standard light source (I_S) and the relative intensity (I_R) obtained by LSI-1 and LSI-2 camera (Bandholnopparat et al., 2019). 92

Chapter 1

Introduction

1.1 Lightning discharges

Lightning, produced by a thunderclouds (cumulonimbus clouds), is a powerful and sudden electrostatic discharge. It is believed that lightning occurs on average 44 $\pm$5 times per second over the entire Earth or 1400 millions discharges for one year (Christian et al., 2003; Cecil et al., 2013). The averages lightning discharges per one square kilometre or the flash rate is 1.5 km^2/year. Of course, the flash rate is much higher in certain areas (***i.e.***, the Central Africa, with a rate of 80 per km^2/year), while other areas have almost zero lightning discharges (***i.e***, near the North Pole and the South Pole).

The most common type of lightning discharges is an intracloud (IC) discharge, which typically occurs between a main positive and a main negative charge region inside a thundercloud (López et al., 2016; Mecikalski and Carey, 2018). Approximately 1/3 of lightning discharges is a cloud-to-ground (CG) discharge. Most of the CG discharges are the negative cloud-to-ground (-CG) discharge that primarily originate from a main negative charge region inside a thundercloud and carry negative charges to the Earth's surface (Williams et al., 1991; Orville, 1994; Orville and Huffines, 2001). Meanwhile, the rest of the CG discharges are called the positive cloud-to-ground (+CG) discharge because they would transfer posi-

tive charges from a thundercloud to the Earth's surface.

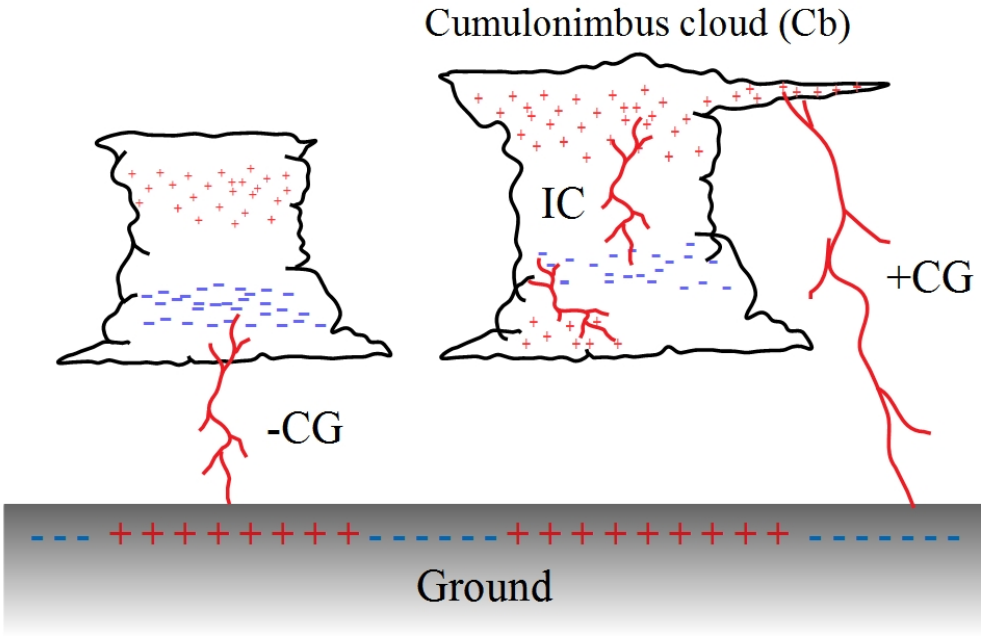

Figure 1.1: Common type of lightning discharges are the IC, +CG, and -CG discharge.

Typical -CG discharges have a peak current of 10-100 kA with 30 kA of median, and $30-200\mu s$ of decay time with a median of $75\mu s$. The +CG discharges are normally stronger than -CG discharges, the peak current of typical +CG discharges varies from 5 to 300 kA with a median of 35 kA, and decay time varies from $25\mu s$ to 2 ms with a median of $230\mu s$ (Berger et al., 1975). Besides those two main discharges, IC discharges are relatively less understood than +CG and -CG discharges because of several reasons, *i.e.*, the observation of IC discharge is more difficult due to it occurs inside a thundercloud, and the currents of IC discharges cannot be measured directly because a discharge channel of IC discharge does not contact with the ground.

1.2 Ratio between intracloud and cloud-to-ground discharges

One of interesting parameter in thunderclouds is the ratio between IC and CG discharges. This ratio is important to be known supporting by several standpoints: (i) to evaluate regional or global NO_X production by lightning discharge (Pickering et al., 1998; Rakov et al., 2004; Ott et al., 2007), (ii) to estimate the contribution of lightning to the global electrical circuit (Williams, 2009; Rycroft and Odzimek, 2010; Mareev and Volodin, 2014), (iii) to study kinematics and microphysics of thunderstorms (Williams et al., 1999; Buechler et al., 2000). The ratio is denoted by $Z = N_{IC}/N_{CG}$, where N_{IC} and N_{CG} are the occurrence number of IC and CG discharges, respectively.

In recent years, many pieces of research show an advance technique in determining regional or global estimates of variability in Z-ratio (Cummins et al., 1998; Shindo and Yokoyama, 1998; Christian et al., 1999; Goodman et al., 2000; Orville et al., 2001). The variation of the Z-ratio with latitude was firstly reported by Pierce (1970). It was found that Z-ratio decreases with the increment of latitude, as shown in Figure 1.2. Prentice and MacKerras (1977) used Z-ratios obtained from 29 ground-based stations located in different places around the world to analyze the correlation of Z-ratio and latitude, and confirm the latitudinal dependences of Z-ratio. It decreases from the equator to the mid-latitudes in the range of 9.0 to 1.5, while the average of Z-value is 3.4. Mackerras et al. (1998) used the lightning data provided by the cloud-ground ratio 3 for studying a worldwide ratio of cloud discharges to ground discharges in thunderstorms. The instruments at sites covering a latitude range from 59.9°N to 27.3°S. They found that the Z-ratio decrease from 3.96 near the Equator to 1.96 at the mid-latitude.

The observation of lightning discharges from space by using satellites such as the Optical Transient Detector (OTD) and the Lightning Images Sensor (LIS) could be easily conducted over wider regions and long periods with a high detection efficiency (Christian et al., 2003; Koshak, 2010). Boccippio et al. (1999)

compared OTD data obtained during the four-years-observation period to ground-based lightning data collected by the National Lightning Detection Network and determined the geographical distribution of the climatological lightning flashes and Z-ratio over the continental of the United States. They reported that the value of Z over this region varies from 2.6 to 3.0. It is also found an unusual low Z-ratio over the mountain, while high Z-ratio can be found over the great plains. The larger values of Z-ratio are found in the regions where the occurrence rates of +CG discharges and severe storms are high. They also investigated the dependence of the Z-ratio on latitude, longitude, and orographic effects. However, they did not find out the apparent geographical dependence of Z-ratio.

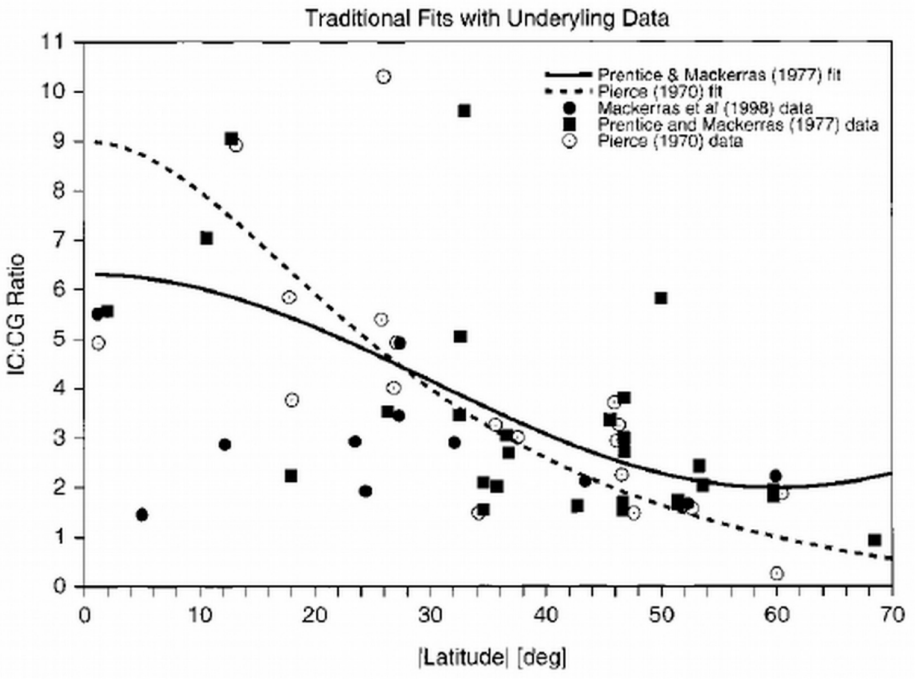

Figure 1.2: Previous ensemble observations of regional Z-ratio and its inferred dependence on latitude (Boccippio et al., 1999)

.

Kuleshov et al. (2006) analyzed the ground-based lightning data obtained by the lightning flash counters (CIGRE-500 and CGR3) and the satellite-based lightning data obtained by the OTD and LIS in order to estimate the Z-ratio over

Australia using the same methodology as Boccippio et al. (1999). They found the values of Z-ratio ranged from 0.75 to 7.7 and concluded that the most representative Z-ratio is $\sim 2 \pm 30\%$ in the latitudinal range of Australia; however, the clear dependence with latitudinal effect was not indicated. Rivas Soriano and Dávila (2007) also analyzed both the satellite-based lightning data obtained by the OTD and the ground-based lightning data obtained by the Spanish lightning detection networks to estimate the Z-ratio over the Iberian Peninsula (35°N – 44°N). It is found that the estimated Z-ratio decreased with respect to an increment of the latitude. It is also found that the Z-ratio varies from 2.2 to 6.0 and the spatial and annual average of the Z-ratio in this latitudinal range was 3.48. de Souza et al. (2009) used the OTD data and the ground-based lightning data from the Brazilian Lightning Detection Network (BrazilDat) to estimate Z-ratio over the southern part of Brazil (14°S - 25°S). In their studies, the dependence of latitudinal effect on Z-ration was not confirmed in this area, as well as and that there is no clear relation between Z-ratio and the population of +CG discharges.

1.3 Global Electric Circuit

The global electrical circuit (GEC) is formed between the ionosphere and the Earth's surface. As shown in Figure 1.3, lightning and rainfall play as important electrical sources of upward currents through the ionosphere and maintain the potential 250 kV between the Earth's surface and the ionosphere (Williams, 2009).

It is believed that each of the 1000 thunderstorms active at any one time generates an upward D.C. (Wilson) current of 1 kA to the ionosphere (Rycroft et al., 2000; Liu et al., 2010; Mach et al., 2011). Then, the global electric circuit closes in the fair-weather (*i.e.*, non-cloudy) regions remote from thunderstorms and electrified rain/shower clouds, creating a downward electric current density and electric field. A typical value of the fair weather field and current density in clean and unpolluted air is ∼120 V/m and 2pA/m^2, respectively (Rycroft et al.,

2000; Harrison, 2005; Nicoll, 2012).

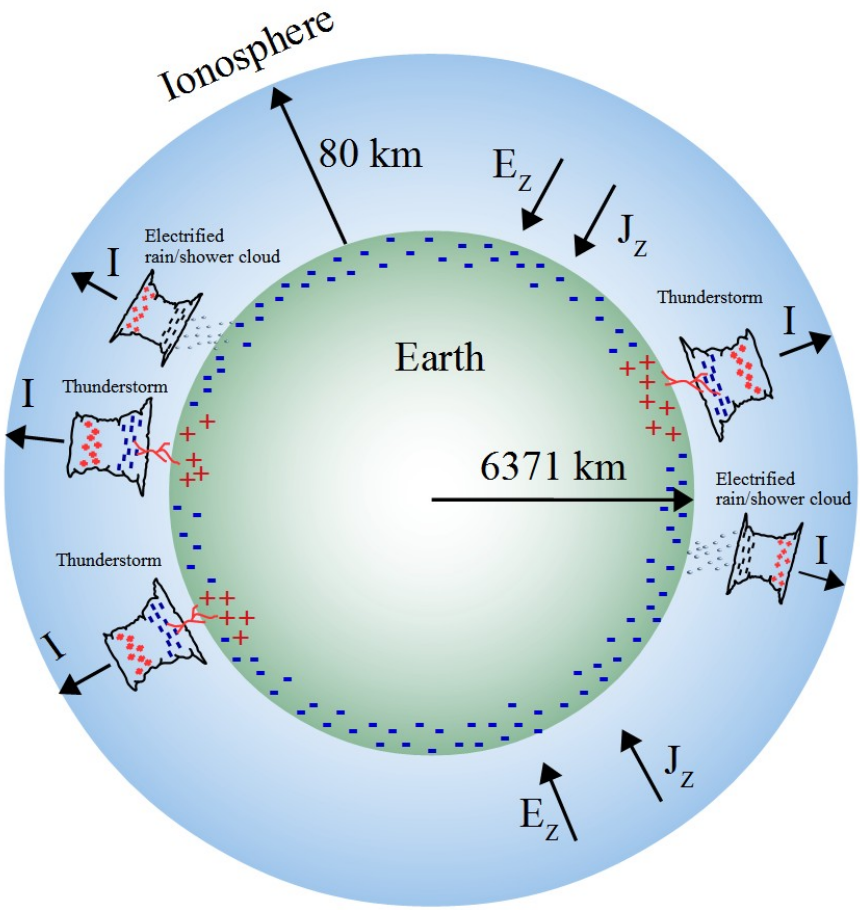

Figure 1.3: Schematic diagram showing the upward electric current to the ionosphere generated by thunderstorms and electrified rain/shower clouds in the global electric circuit.

The fair weather electric field normally shows a daily variation that follows the universal time. This diurnal cycle variation is widely known as the Carnegie curve. The maximum fair weather electric field around 19:00 UTC and minimum around 03:00 UTC as shown in Figure 1.4. The Carnegie curve is named after the geophysical survey boat of the Carnegie Institution of Washington which measures the fair weather electric field around the world (Harrison, 2005). It is believed

that the daily variations in atmospheric electrification associates with the different global disturbed weather regions (Harrison, 2012).

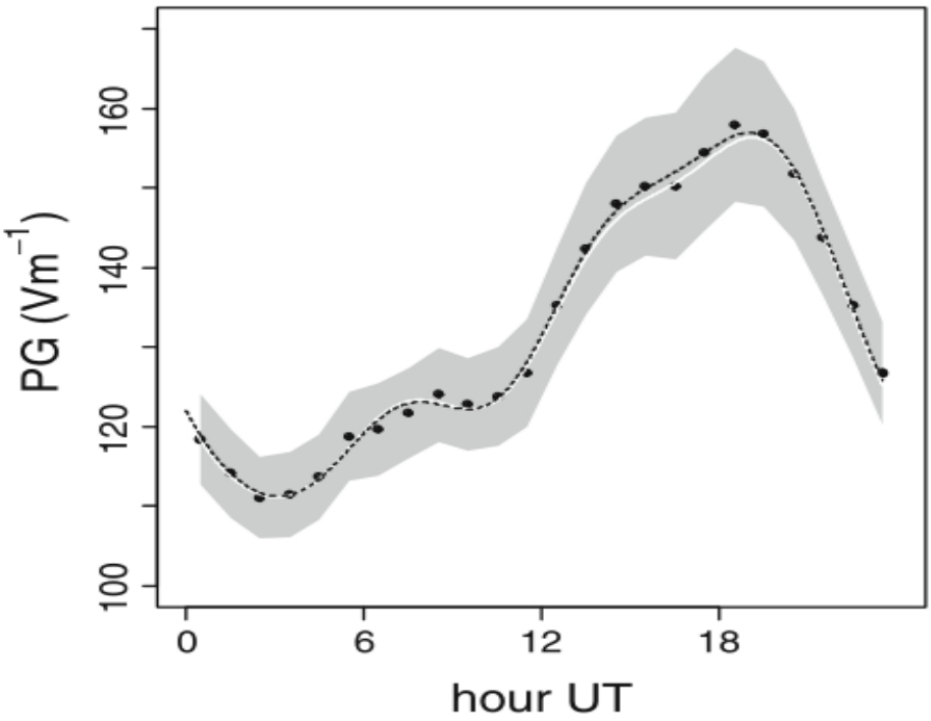

Figure 1.4: Potential gradient of the fair weather electric field measured by Carnegie Cruise III (points). The dotted line is a fitted line from the data. The greyed area is the standard errors (Harrison, 2005).

Rycroft et al. (2007) introduced the simple 1-dimensional equivalent circuit of the global electric circuit. As illustrated in Figure 1.5, they described that both thunderstorms and electrified rain/shower clouds are the main current generators. These generators behave as small batteries that drive upward electric currents to the ionosphere. Figure 1.5 could describe that a thunderstorm is represented in the circuit as a structure of resistances, and capacitors in parallel with them. A thunderstorm is assumed to be a cylindrical shape whose diameter is approximately 20 km. The top and bottom of the thundercloud are located at an altitude of 15 km and 5 km respectively. At the bottom of the thundercloud, there is a charge of -26C and, at the top +14C (Mach et al., 2009). The electrified rain/shower

cloud is also presented in this circuit, as a two series resistors (R_5 and R_6), and a constant current source I_{PC} in parallel with a resistor R_6.

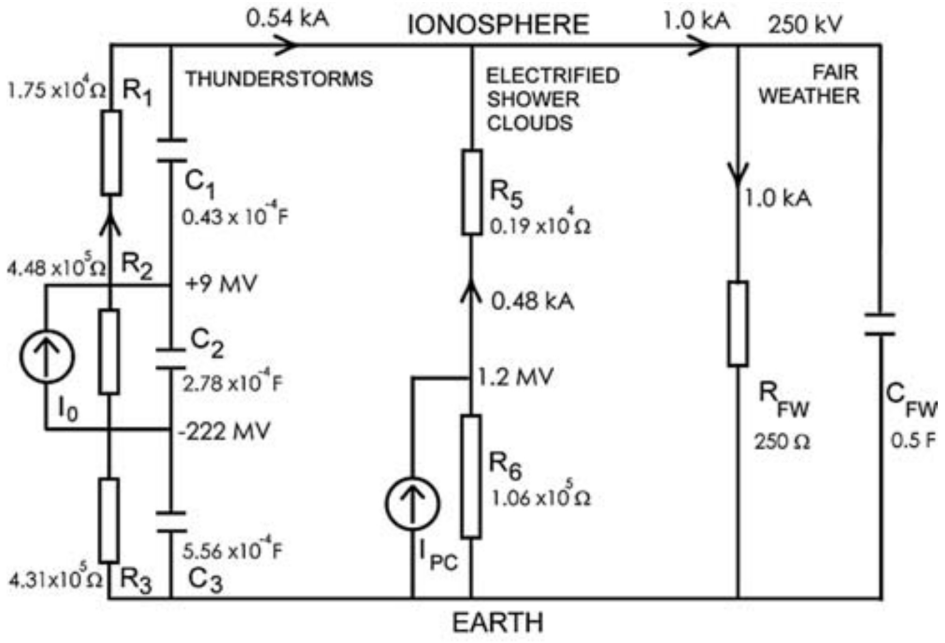

Figure 1.5: Circuit diagram of the global electric circuit (Rycroft et al., 2007). In this circuit, thunderstorms and electrified rain/shower clouds are the main currents generators.

One of the important parameter for calculating the contribution of lightning and rainfall to the global electric circuit is the resistance of the areas where do not have thunderclouds. This resistance is called the fair-weather resistance, and it is represented by R_{FW} in the circuit in Figure 1.5. The value of R_{FW} was calculated using the model of atmospheric conductivity profile as shown in Figure 1.6 (Makino and Ogawa, 1985; Nickolaenko et al., 2016). Assuming there are 1000 thunderstorms active at the same time all over the world, the values of fair-weather resistance was calculated by:

$$R_{FW} = \frac{1}{A_E - 1000A_T} \int_{Z_g}^{Z_{ion}} \frac{dz}{\sigma(z)} \tag{1.1}$$

where A_E is the area of the Earth's surface ($5.101 \times 10^{14} m^2$), A_T is the area of a thunderstorm (constant value of 314km^2), and z is a height. Using the model of atmospheric conductivity profile (Figure 1.6), Rycroft et al. (2007) introduced that the global resistance was 250 Ω. Baumgaertner et al. (2013) included the effect of galactic cosmic ray flux, radon emissions from the Earth's surface, aerosol number concentrations, cloud, and temperature in the electric conductivity model, and calculated the yearly average column resistance using the Community Earth System Model (CERM1). They found that the total global resistance varied from 220 to 245 Ω.

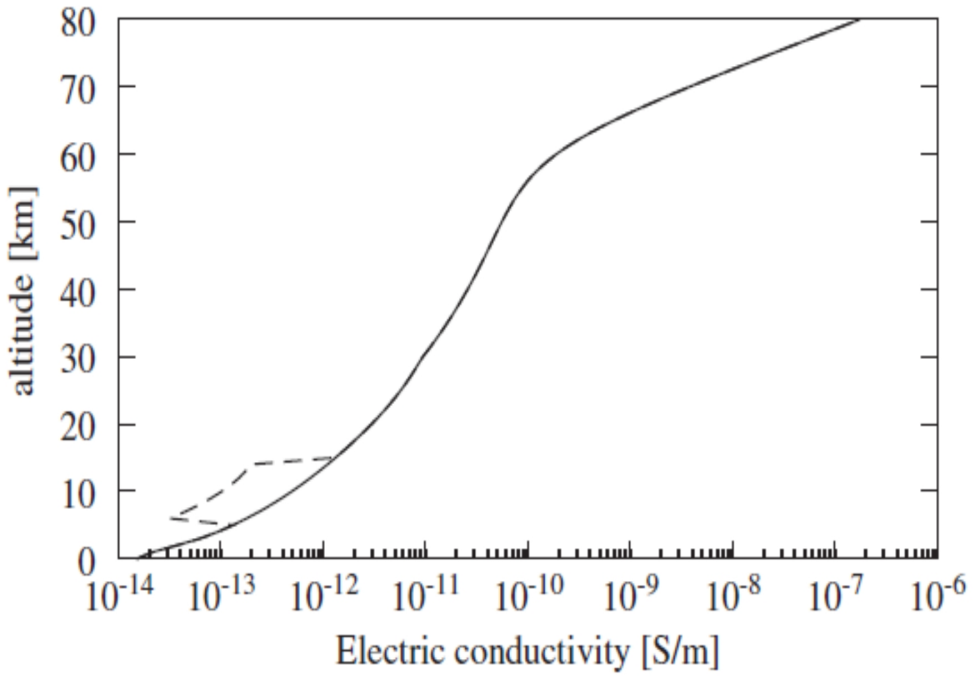

Figure 1.6: Electric conductivity profile of the air ($\sigma(z)$) for calculating the values of resistance in the global electric circuit (Rycroft et al., 2007).

Using the 1-dimensional equivalent circuit of the global electric circuit as shown in Figure 1.5, Rycroft and Odzimek (2010) found that all thunderstorms generate 600 A upward current to the ionosphere, while electrified rain/shower clouds could generate only 400 A, leading to a total upward current of 1kA to the ionosphere.

It was also found that lightning discharges from the global electric circuit is only ∼40 A. This number has a good agreement with those reports in Mareev et al. (2008), they used a numerical model to estimate the contribution of lightning to the global circuit, and found that lightning discharges contribute between 50 and 400 A to the global circuit. Consequently, global rainfall contribute $\sim 960A$ to the global electric circuit.

1.4 Limitation of the previous studies and the Purposes of this study

Although the lightning data obtained by the space-borne and ground-based observations were combined for clarifying the geographical distribution of Z-ratios with a high detection efficiency, these studies focused on only a specific and limited region where the ground-based lightning data was available. Consequently, the regional, seasonal, and latitudinal variations of Z-ratios in the global scale are not fully understood yet. The purposes of the first part in this study are (i) to develop a new method classifying a discharge type using satellite-based lightning observation data obtained by JEM-GLIMS and ground-based lightning data obtained by the Japanese lightning detection network, the national lightning detection network, the world wide lightning location network, and the global ELF observation network, and (ii) to estimate the Z-value and its latitudinal, regional, and seasonal dependences.

As discussed in Section 1.3, the contribution of lightning and rainfall to the global electric circuit are not fully understood due to the difficulty in estimation the occurrence number of lightning discharges especially intracloud discharges. In addition, it is difficult to quantitatively estimate the contribution of global rainfall current to the global electric circuit due to the difficulty of identifying the rainfall volume and its global distribution. Therefore, the purposes of the second part of

this work are (i)to develop the 3-dimensional circuit model for the global electric circuit using the CG discharges data provided by the world wide lightning location network and the global rainfall data provided by the global precipitation project, (ii) After that, the new model will be used for estimating the contribution of lightning and precipitation activities to the global electric circuit. (iii) Apart of the estimation, the new model will also be used to simulate the fair-weather electric fields and compared with the observation fair weather electric fields observed at the Syowa station, Antarctica, Reading station, United Kingdom, and Kakioka station, Japan.

This thesis will be divided into 6 main chapters, which could be described as follows. The first part of Chapter 2 of this work presents the optical instruments of JEM-GLIMS space-based mission used for measuring the lightning emission. In addition, ground-based lightning detection networks are also described. The second part of Chapter 2 explains the method for identifying the lightning discharge type using the lightning data provided by JEM-GLIMS and the ground-based networks. Besides, the method for calculating the Z-ratio is also presented. Chapter 3 discusses the optical properties of the identified IC, +CG, and -CG discharges obtained from JEM-GLIMS optical instruments. In this chapter, the latitudinal, regional, and seasonal dependences of Z-ratio were also discussed. Chapter 4 explains the 3-dimensional model of the global electric circuit, which was newly developed. The method for calculating the upward electric currents by lightning and rainfall is also presented in this chapter. Besides, the method for calculating the fair-weather resistance using the average column resistance map is also presented. Chapter 5 gives the results on the contribution of lightning and rainfall to the global atmospheric circuit. It also discusses the correlation between the lightning and precipitation activities and the fair-whether electric filed. Finally, chapter 6 summarizes the main points of this work.

Chapter 2

Estimation of the ratio between intracloud discharges and cloud-to-ground discharges

2.1 Satellite-based lightning data

In order to study the regional, seasonal, and latitudinal dependence of Z-ratio, the lightning events obtained by the Global Lightning and Sprite Measurements on Japanese Experiment Module (JEM-GLIMS) observation were used. JEM-GLIMS is a spaced-based mission which was designed to study lightning discharges and lightning-associated transient luminous events (TLEs), *i.e.*, sprites, elves, blue Jets, from the International Space Station (ISS) in the nadir direction (Sato, 2015).

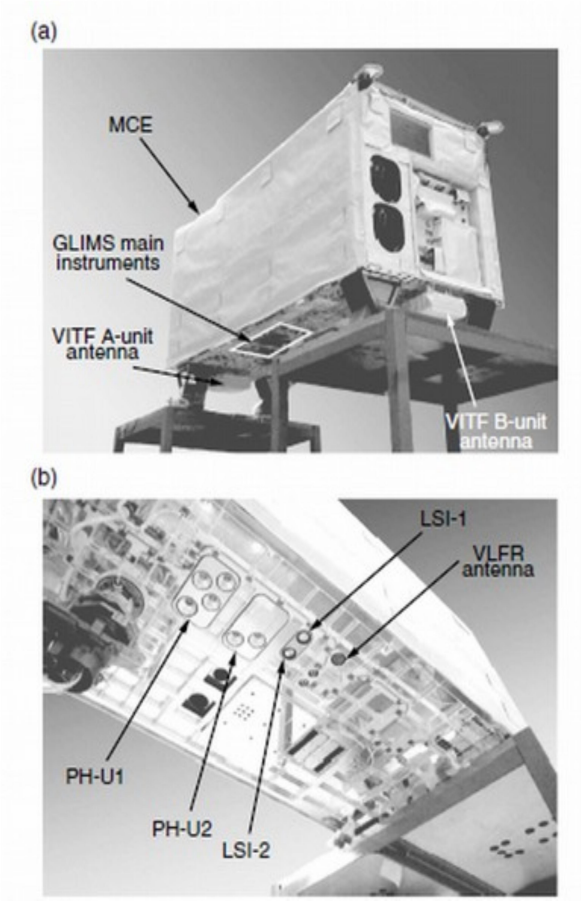

Figure 2.1: JEM-GLIMS optical instruments (PHs and LSI) and electromagnetic waves receiver (VLFR) (Sato, 2015).

As illustrated in Figure 2.1, the instruments onboard JEM-GLIMS are the optical instruments and electromagnetic waves receivers. The main optical instruments are the six-channel spectrophotometers (PHs) and the Lightning and Sprite Imager (LSI). The PHs measure the absolute optical intensity of lightning discharges in the wavelength range of 150-280 nm (PH1), 310-321 nm (PH5), 332-342 nm (PH2), 386-397 nm (PH6), 599-900 nm (PH4), 755-766 nm (PH3), respectively (Sato et al., 2011b; Adachi et al., 2016). Meanwhile, the LSI consists of wideband (LSI-1) and narrowband (LSI-2) Complementary Metal Oxide Semiconductor (CMOS) cameras. The LSI-1 acquires the optical images of lightning discharges in the wavelength range of 768-830 nm, while the LSI-2 acquires the optical images of lightning discharges in the wavelength range of 760-775 nm (Sato

et al., 2011a; Sato, 2015; Sato et al., 2016). JEM-GLIMS conducted the lightning and TLE optical observations in the local time (LT) range of $19:00-05:00$ LT (Sato, 2015). The detail of the optical instrument of JEM-GLIMS are summarised in table 2.1

Table 2.1: JEM-GLIMS optical instruments

Name	ID	Specification
CMOS Camera	LSI	Two CMOS cameras
		512× 512 pixels
		FOV=28.3° × 28.3°, fps = 29,
		10 bit resolution,
		LSI-1:λ = 765-830nm, LSI-2:λ = 762±5nm,
Photometer	PH	6-channel photometers
		λ_{PH1} = 150-280nm, λ_{PH5} = 316±5nm,
		λ_{PH2} = 337±5nm, λ_{PH6} = 392±5nm,
		λ_{PH3} = 762±5nm, λ_{PH4} = 600-900nm

JEM-GLIMS measured the optical emissions of the 8354 lightning discharges, over 32 months in total, during November 2012-August 2015. These lightning events were mainly detected in the latitudinal range from 51°S to 51°N over both oceanic and continental regions as shown in Figure 2.2. It must be noted that, the gray hatched area in Figure 2.2 represents the region where the observations using JEM-GLIMS were not conducted due to the limitation of the orbital inclination angle of the ISS.

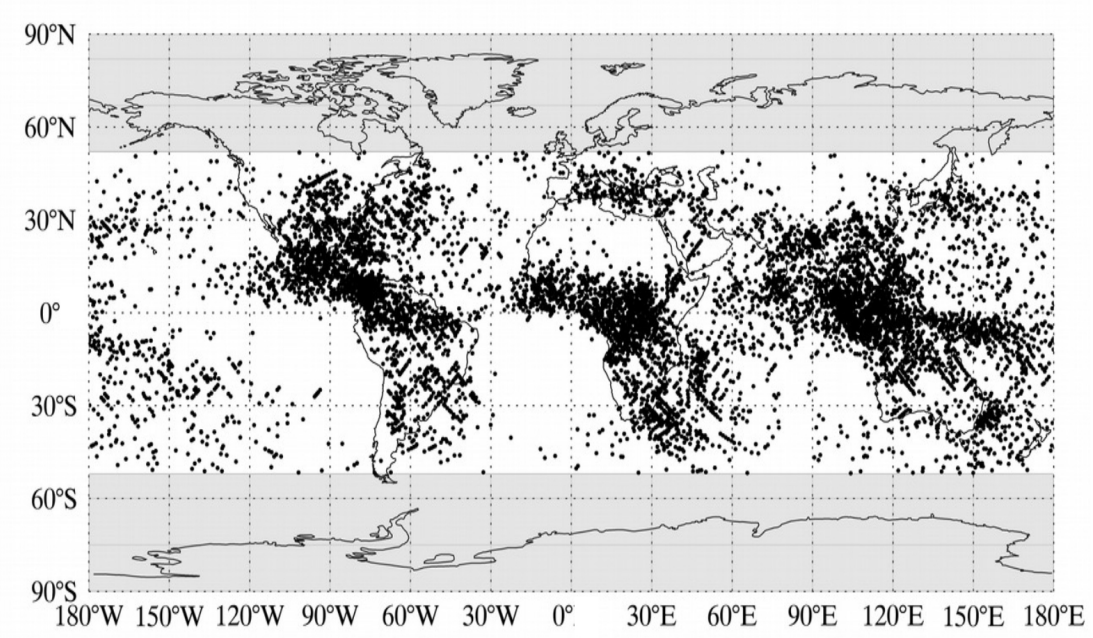

Figure 2.2: Global distribution of the 8354 lightning events detected by JEM-GLIMS between November 2012 and August 2015.

2.2 Ground-based lightning data

The ground-based lighting data in this study is provided by the Japanese Lightning Detection Network, the National Lightning Detection Network, the World Wide Lightning Location Network, and the Global ELF Observation Network. The detailed information on the specifications and operation of details of each ground-based network would be explained as follows:

2.2.1 Japanese Lightning Detection Network

Japanese Lightning Detection Network (JLDN) consists of thirty lightning detection sensors that are installed nationwide for detecting lightning discharges in the whole extent of Japan. These sensors are divided into two categories, *i.e.*, the

IMPACT-ESP sensor and the LPATS-IV sensor (Matsui and Hara, 2011). These sensors observe waveforms of electromagnetic impulses from lightning discharges in a wide frequency band ranging from VLF to LF frequency, and estimates location, peak current, discharge types, and polarity of lightning discharge, *i.e.*, IC, +CG, and -CG discharges. The detection efficiency of JLDN over Japan continental is more than 90% with the location accuracy less than 500 m. More detailed information on the specifications and operation of JLDN can be found in the papers of (Ishii et al., 2005; Matsui and Takano, 2010; Matsui and Hara, 2011).

2.2.2 National Lightning Detection Network

The U.S. National Lightning Detection Network (NLDN), consisting of a set of LS7002 sensors located in different part of the United States, has been providing lightning data since 1989 (Nag et al., 2014). The NLDN was originally established for monitoring lightning hazards (Cummins et al., 1998; Cummins and Murphy, 2009). More than 100 LS7002 sensors over the US continental report lightning discharges in near real time (Cummins et al., 2006). This network works with a combination of the magnetic direction finding and time of arrival techniques to geolocate lightning discharges, and uses multiple waveform parameters to classify cloud and cloud-to-ground lightning polarity, amplitude of lightning flashes (Orville, 1994; Orville and Huffines, 2001; Nag et al., 2011). The detection efficiency for cloud-to-ground and intracloud discharge over the entire United States is approximately 95% and 50%, respectively. Meanwhile, median location accuracy of 150-250 m over the majority of the United States is confirmed (Cummins and Murphy, 2009; Zhang et al., 2016).

2.2.3 World Wide Lightning Location Network

The World Wide Lightning Location Network (WWLLN), has been providing global lightning data since 2004 (Rodger et al., 2009), has been developed using

existing researches by a number of all-over-the-world research institutes. So far, more than 60 sensors were installed in the network (Nag et al., 2011). These sensors observe lightning discharges using the time of group arrival for the electromagnetic wave packets from individual lightning discharges (Dowden et al., 2002). The WWLLN provides real-time locations of cloud-to-ground and cloud discharges occurring anywhere on the Earth with the detection efficiency is less than 50% and mean location accuracy is less than 10 km. However, WWLLN also has a limitation because lightning was not observed with the same detection efficiency in any area. This is due to variable WWLLN station coverage (Rodger et al., 2009; Abarca et al., 2010).

2.2.4 Global ELF Observation Network

The Global ELF Observation Network (GEON), consisting of the orthogonal search coil magnetometers in the geomagnetic north–south (H-component) and the east–west (D-component) directions, is a network to measure a magnetic field perturbation in the frequency range of 1–100 Hz from a lightning discharge. The network provides a location, peak current, and polarity of CG discharges, *i.e.*, +CG, and -CG discharges, around the world. The main instruments, *i.e.*, the orthogonal search coil magnetometers, of this network have been installed at the Syowa station (69.0°S, 39.6°E), the Onagawa observatory (38.4°N, 141.5°E), in Japan, as well as, the Esrange (67.9°N, 21.1°E) in Sweden (Sato et al., 2003). More detailed information on the specifications and operation of GEON can be found in the papers of Sato et al. (2003).

2.3 Estimation of the ratio between intracloud versus cloud-to-ground discharges

The observation period of 32-month, starting from November 1, 2012, to August 31, 2015, using satellite-based and ground-based lightning was conducted in this study for studying the latitudinal, regional, and seasonal dependences of Z-ratio. Figure 2.3 shows the flow chart for classifying JEM-GLIMS lightning events to be IC, +CG, and -CG discharge by compared JEM-GLIMS lightning events with the ground-based lightning data provided by ground-based networks, *i.e.*, JLDN, WWLLN, GEON, and NLDN.

In order to describe this method, JEM-GLIMS data was firstly compared to the ground-based lightning data to identify discharge types, *i.e.*, IC, +CG, and -CG discharge. There are two adopted conditions for identifying the coincidence between the JEM-GLIMS lightning events and ground-based lightning events: 1) the horizontal distance (D) of JEM-GLIMS lightning events and ground-based lightning events, and 2) time difference (Δt) between the detection time of JEM-GLIMS lightning events (T_{Glims}) and detection time of ground-based lightning events (T_{Ground}). In the case that the value of $D \leq 160$ km and Δt is set to be ≤ 1.5 ms, the JEM-GLIMS lightning event is identified to be the same lightning event detected by the ground-based lightning networks.

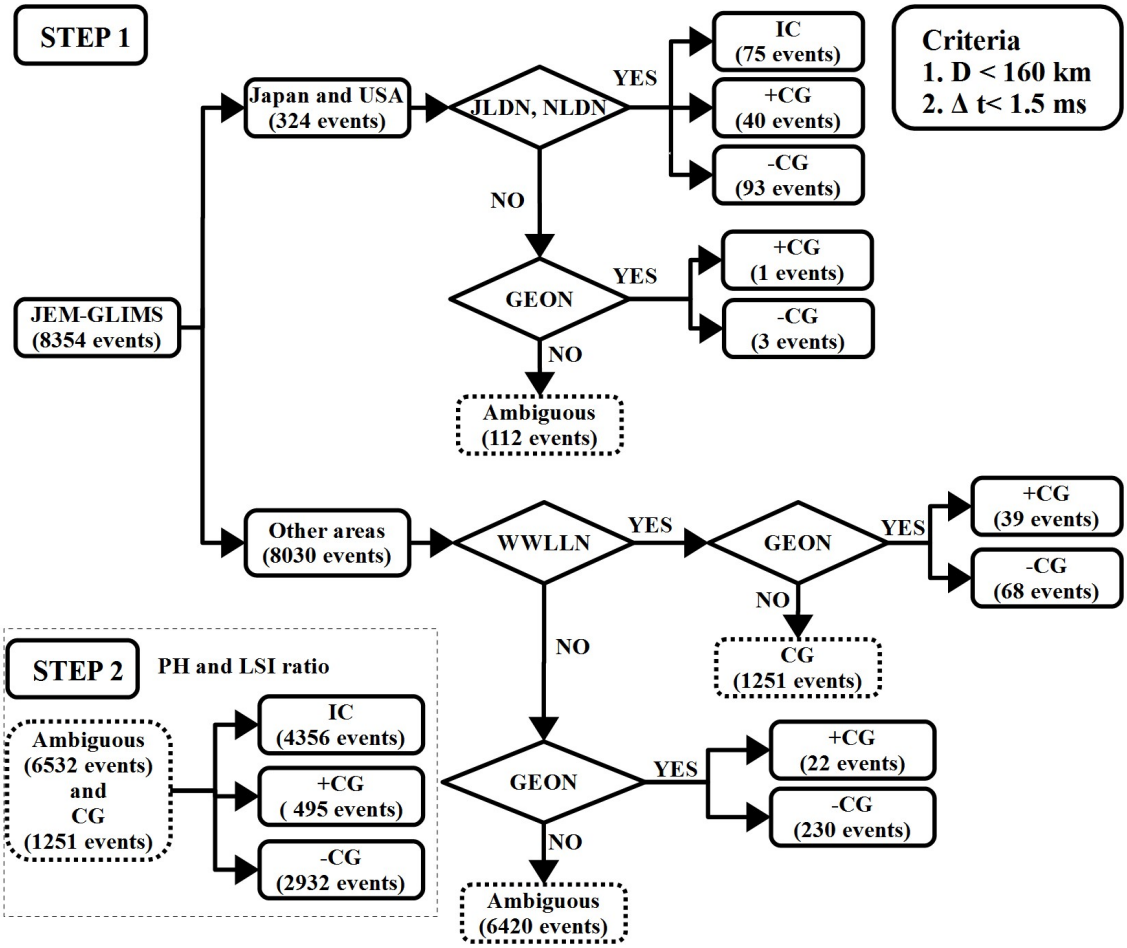

Figure 2.3: Flow chart showing how the discharge type of JEM-GLIMS lightning events were classified into IC, -CG, +CG, ambiguous flash using the ground-based lightning data.

The condition of time (Δt = 1.5 ms) represents the delay time (0.2 ms) from a light source to a cloud top due to the multi-path scattering in thunderclouds (Koshak et al., 1994) and of 1.3 ms which is the average travel time of light from a cloud top to the JEM-GLIMS altitude. While the condition of D is set to be 160 km, because a lightning event could occur anywhere inside the field of view of the JEM-GLIMS optical instruments as shown in Figure 2.4.

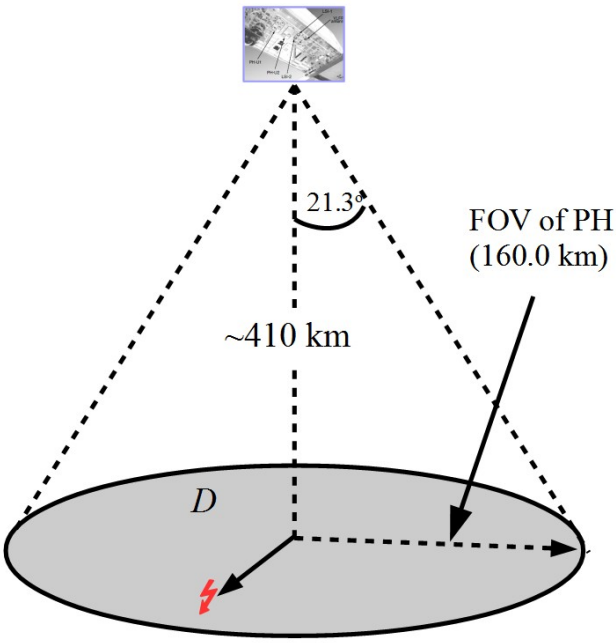

Figure 2.4: Schematic illustration showing the field of view of PHs and a distance between JEM-GLIMS nadir point and a ground-based lightning event (*D*)

The ELF magnetic field waveform data detected by the GEON was further analysed for estimating the polarity of CG discharges, *i.e.*, +CG or -CG discharge, using the magnetic direction-finding method, proposed by Sato et al. (2003). In brief, electromagnetic waves obtained by the orthogonal search coil magnetometers in the geomagnetic north–south (H-component) and the east–west (D-component) directions were used for considering the CG discharges polarity. In Figure 2.5(a), an upward moving return stroke current would come from a -CG discharge. For a +CG discharge, the current would point downward, and the signal from the loop antenna would have the opposite polarity as shown in Figure 2.5(b).

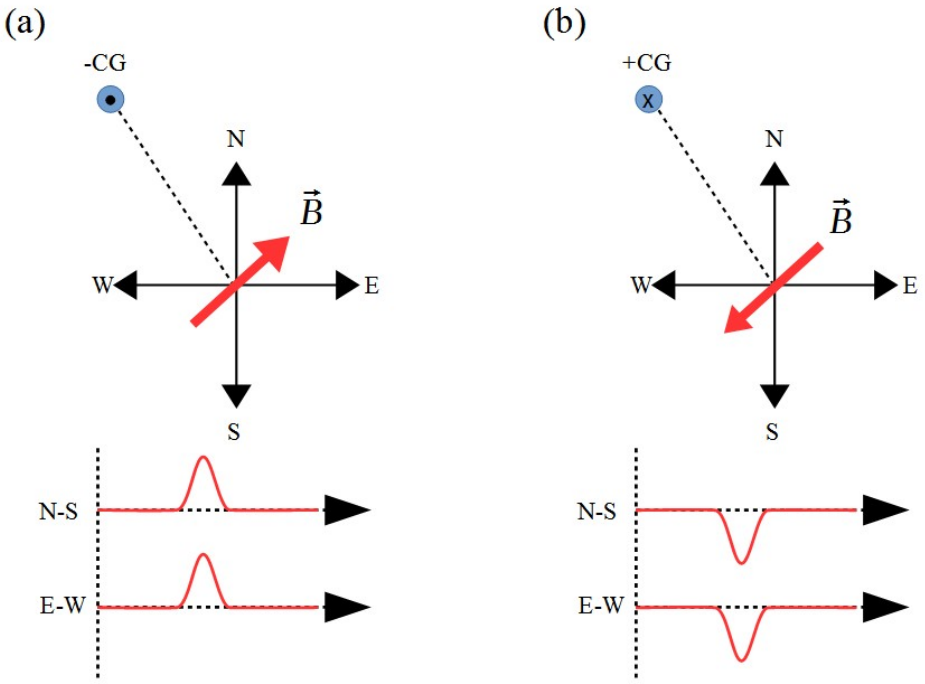

Figure 2.5: Electromagnetic waves obtained by orthogonal search coil for identifying the polarity of lightning discharge.

In Figure 2.5, lightning strikes are located north-west (quadrant 1) of the antenna. Therefore, a large positive signal from a -CG discharge would be detected by H-component and D-component search coil. For a +CG discharge, a large negative signal would be detected by both H-component and D-component search coil as shown in Figure 2.5(b). For the CG discharge occurring at another quadrant, the polarity was considered from Table 2.2

According to these procedures, JEM-GLIMS lightning events would be categorized into five categories: 1) "IC discharge", 2) "+CG discharge", 3) "-CG discharge", 4) CG discharge, and 5) "ambiguous discharge events". It should be noted that JEM-GLIMS lightning events were identified as an ambiguous discharge because these lightning discharges were not reported by the ground-based lightning networks.

By comparing JEM-GLIMS lightning data with ground-based lightning data, 571 of JEM-GLIMS lightning events were classified to be 75 of IC discharges, 102 of

Table 2.2: Electromagnetic waves signal in D and H component for considering the polarity of CG discharge.

	-CG		+CG	
	H-component	D-component	H-component	D-component
Quadrant 1	+	+	-	-
Quadrant 2	-	+	+	-
Quadrant 3	-	-	+	+
Quadrant 4	+	-	-	+

+CG discharges, and of 394 -CG discharges, respectively. However, this method is not applicable for other 7783 JEM-GLIMS lightning events because of two major reasons, as follows: 1) using both JEM-GLIMS lightning data and NLDN, or JLDN is useful for classifying discharges type; however, these lightning networks are specifically available only at the specific area. 2) Even though the comparison of JEM-GLIMS lightning data and WWLLN is possible to classify the discharge type of JEM-GLIMS lightning events for all-over-the-world, WWLLN has much low efficiency in detection (Rodger et al., 2009; Hutchins et al., 2012). Therefore, in order to identify the discharge type of both 6532 of ambiguous lightning events and 1251 of CG events, a new criteria, which is the intensity ratio between blue and red emissions measured by PHs, *i.e.*, PH2/PH3, PH5/PH3, PH6/PH3, PH2/PH4, PH5/PH4, and PH6/PH4 should be used as the indicator of the discharge types.

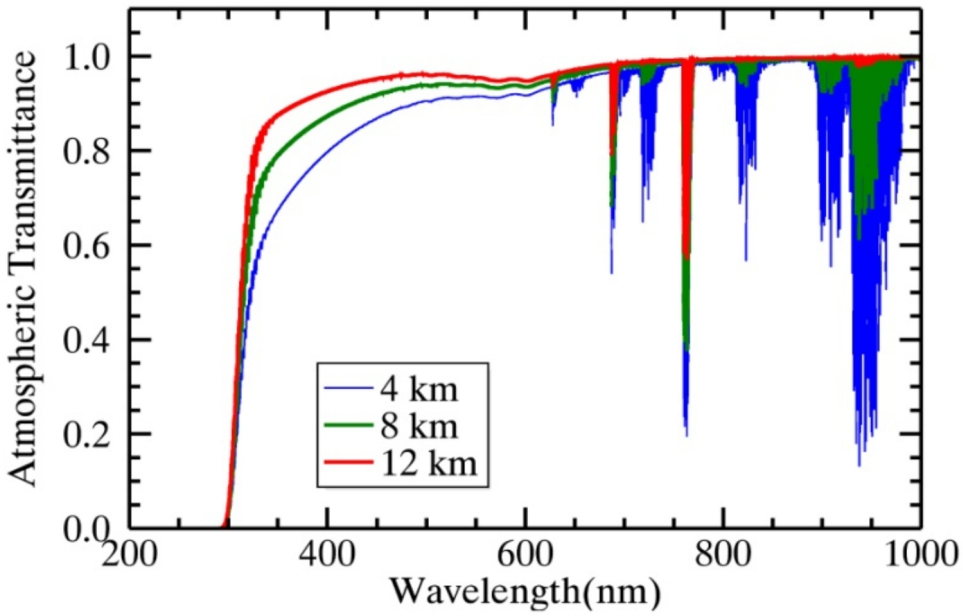

Figure 2.6: Model of atmospheric transmittance in the wavelength range of 200-1000 nm calculated by the MODTRAN code. The blue, green and red lines show the transmittance from a light source located at the 4, 8, and 12 km altitude to the zenith direction, respectively.

The new method for classifying the remaining JEM-GLIMS lightning events is based on the different attenuation rates of blue and red emissions from lightning discharge channels to the ISS as shown in Figure 2.6. Blue emissions from lightning discharges (*i.e.*, 310-321 nm, 332-342 nm, 386-397 nm) are more absorbed and attenuated than red emissions (*i.e.*, 755-766 nm, 599-900 nm). Lu et al. (2012) pointed out that the normal discharge channels of +CG discharges tend to occur at a higher altitude in the thundercloud or near the cloud top (Figure 2.7). Consequently, the PH intensity ratio of +CG discharges becomes the highest since blue emission from +CG lightning discharge channel can escape to the ISS altitude. This can also happen in IC discharges because the discharge channel of IC discharges locates between the cloud top and cloud base where a main positive charge and a main negative charge are located (López et al., 2016;

Lyu et al., 2016). In contrast, the normal discharge channels of -CG discharges occur at the lower altitude or near the cloud-based (Ballarotti and Saba, 2005; Sun et al., 2016). Consequently, the PH intensity ratio of -CG discharges should lower than that of +CG and IC discharges because the optical blue emissions from lightning discharge channels tend to be more absorbed.

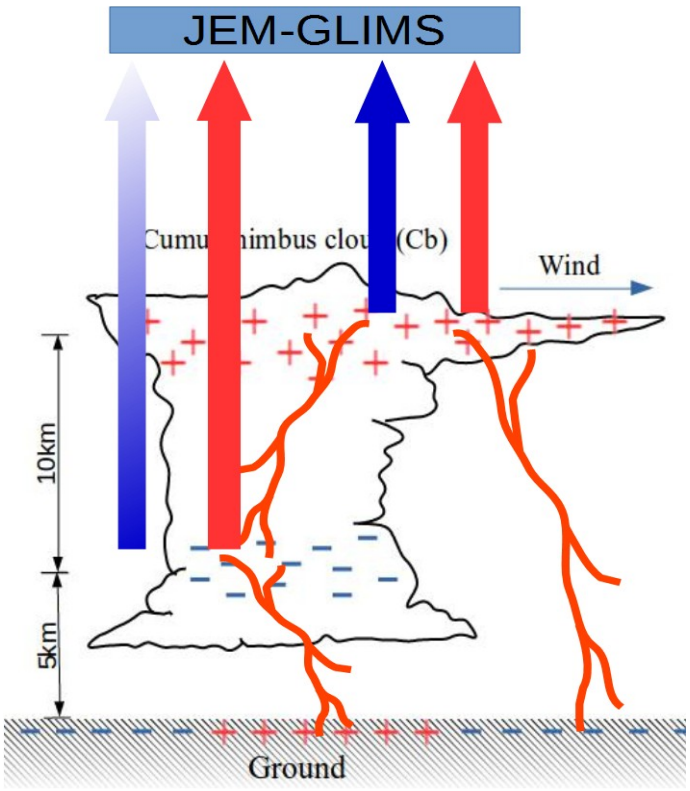

Figure 2.7: The difference of the altitude of IC, +CG, and -CG discharge channel that might be used for classify the discharge types.

In a final step, in order to calculated the *Z*-ratio, the occurrence number of IC, +CG, -CG discharges detected by JEM-GLIMS was counted at each 3.0° × 3.0° grid. After that, the *Z*-ratio at each grid would be calculated by Equation 2.1.

$$Z = \frac{\frac{N_{IC}}{DE_{IC}}}{(\frac{N_{+CG}}{DE_{+CG}} + \frac{N_{-CG}}{DE_{-CG}})} \tag{2.1}$$

where N_{IC}, N_{+CG}, N_{-CG} are the occurrence number of IC, +CG, and -CG discharges, respectively, while DE_{IC}, DE_{+CG}, and DE_{-CG} are the detection efficiency of IC, +CG, and -CG discharges, respectively. The estimated efficiencies of JEM-GLIMS IC, +CG, and -CG flashes detection were approximately 11.2%, 28.3%, and 19.7%, respectively. The detail of how to estimate the detection efficiency of JEM-GLIMS for IC, +CG, -CG discharge will be described in Appendix B.

Chapter 3

Regional, Seasonal, and Latitudinal dependences of Z-ratio

3.1 Example of -CG, +CG and IC discharge

3.1.1 Example of -CG discharge

By comparing JEM-GLIMS lightning data with the ground-based lightning data provided by JLDN, NLDN, WWLLN, and GEON, the total 571 of JEM-GLIMS lightning events were classified to 75 of IC, 102 of +CG, and 394 of -CG discharges, respectively. Then, the ratios between blue and red PH channels for each identified discharge were calculated. Figure 3.1 shows an example of the identified -CG discharge. The event was detected by the JEM-GLIMS optical instruments at 20:15:49.803 UT on March 24, 2014, where JEM-GLIMS was located at (37.212°E, 7.564°N) over Africa.

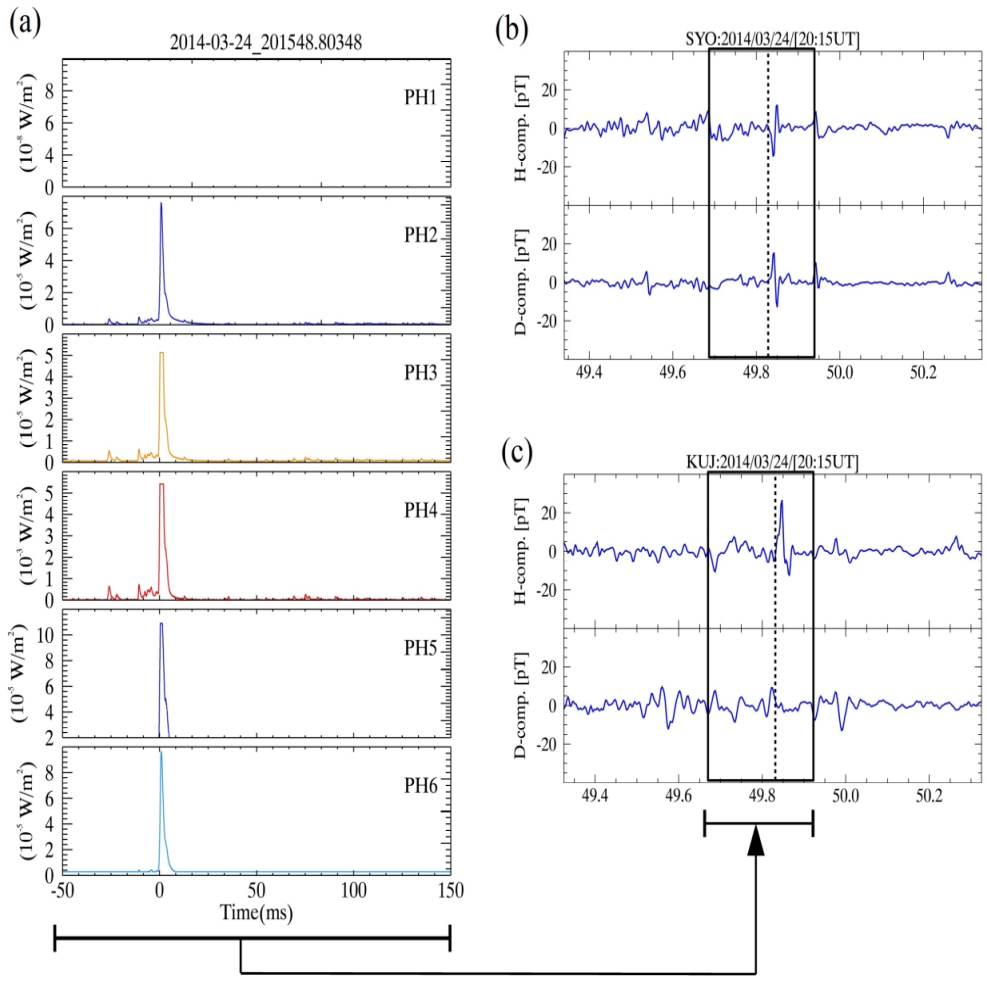

Figure 3.1: (a) -CG Lightning event detected by JEM-GLIMS optical instruments at 20:15:48.80348 UT on 24 March 2014. Figure (b) and (c), plot of the ELF magnetic field waveform data acquired at Syowa and Kuju station, respectively.

As shown in Figure 3.1(a), PH2-PH6 detected optical emissions from the lightning discharges,while Figure 3.1(b) and 3.1(c) is a plot of ELF magnetic field waveform data obtained at Syowa atation, Antarctica, and Kuju stations, Japan, between 20:15:49.35–20:15:50.35 UT. Considering the optical propagation time of 1.35 ms from the assumed light source at the altitude of 10 km to the JEM-GLIMS altitude of 411.6 km, the distance between JEM-GLIMS nadir point and

Syowa station and JEM-GLIMS nadir point to Kuju station is 8527.1 km and 9928.8 km, respectively. Therefore, a wave propagation time from the lightning event to Syowa station and Kuju station is $\Delta t = 35.53$ ms and $\Delta t = 41.37$ ms, respectively. The expected arrival time of the magnetic waves at Syowa and Kuju station would be 20:15:49.838 UT and 20:15:49.844 UT, respectively. As shown in Figure 3.1(b) and 3.1(c), there is a clear transient ELF waveform at the PH trigger time. Note that all PH channels except for PH1$(150-280nm)$ succeeded in detecting the optical emissions of this -CG discharge. The possible explanation is that the FUV emitted by this -CG discharge is severely absorbed by the Earth's atmosphere. Therefore, the FUV emitted by this -CG discharge could not escape to JEM-GLIMS optical instruments.

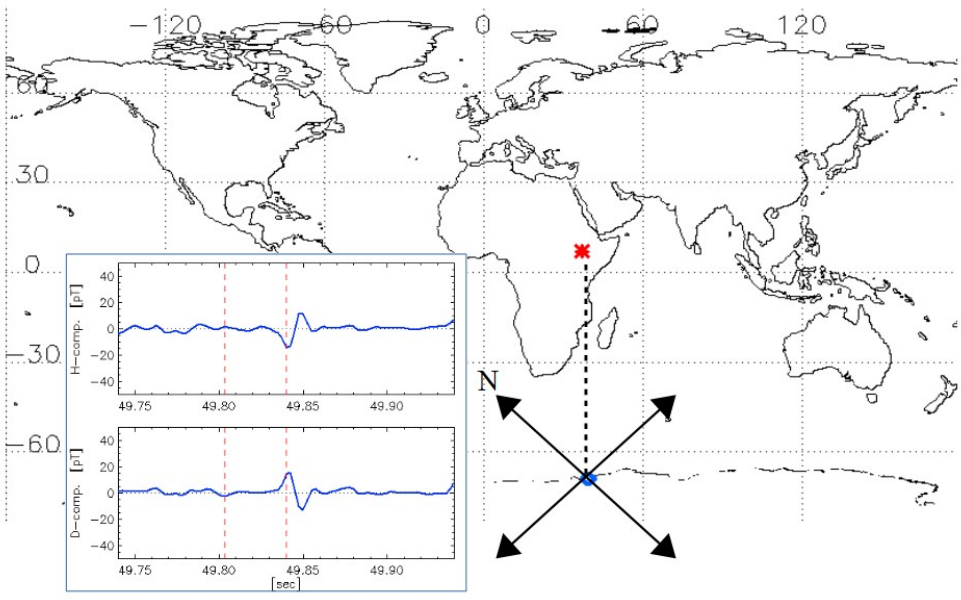

Figure 3.2: Electromagnetic waves signal on H-component and D-component for considering the polarity of CG event of Figure 3.1.

By considering the component of electromagnetic waves detected by the H-component and D-component and the location of lightning event as shown in Figure 3.2 and Table 2.2. This lightning event was identify to be a -CG discharge. Then, the logarithmic of PH intensity ratio, *i.e.*, PH2/PH3, PH5/PH3, PH6/PH3,

PH2/PH4, PH5/PH4, PH6/PH4, at t = 0 ms and LSI intensity ratio of this lightning event was calculated.

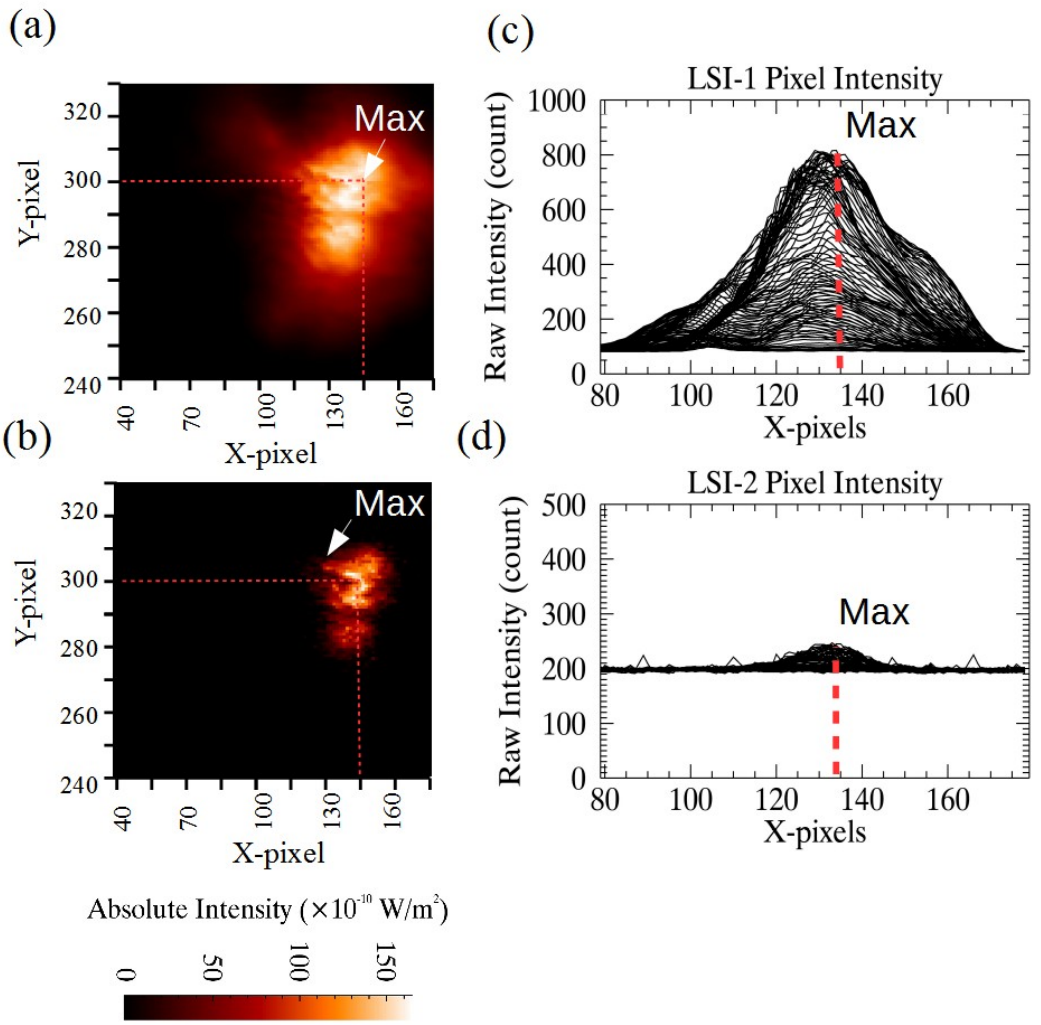

Figure 3.3: An example of (a) lightning discharge image on LSI-1(b) Same as (a) except for LSI-2.Figure (c) and (d) is the plot of raw count for each y-pixel for LSI-1 and LSI-2.

In order to estimate the intensity ratio between lightning emission obtained by LSI-2 and LSI-1 or the LSI intensity ratio, the maximum emission value in LSI-2 and LSI-1 were used. As a first step, the raw count intensity for each y-pixel was

plotted as shown in Figure 3.3. As shown in Figure 3.3(b) and (d), it is found that the maximum raw count in LSI-2 is located at the pixel X = 135 and Y = 300. Therefore, the value of lightning emission in this pixel, both in LSI-2 and LSI-1 images, was used to estimate the LSI intensity ratio. The saturation level of the LSI image data is 210 digit (10-bit data), that is 1024 digit. So, the signal level was not saturated in this event. Note that the lightning events that has the saturated data in LSI-1 or LSI-2 were excluded for estimating the LSI intensity ratio.

3.1.2 Example of +CG discharge

Figure 3.4 presents an example of the identified +CG discharge. The event was detected by the JEM-GLIMS optical instruments at 03:25:22.383 UT on September 13, 2014, where JEM-GLIMS was located at (16.051°E, 6.767°S) over Africa. As shown in Figure 3.4(a), PH2-PH6 detected optical emissions from the lightning discharges,while Figure 3.4(b) and 3.4(c) is a plot of ELF magnetic field waveform data obtained at Syowa atation, Antarctica, and Kuju stations, Japan, between 03:25:21.25–03:25:27.25 UT. Considering the optical propagation time of 1.35 ms from the assumed light source at the altitude of 10 km to the JEM-GLIMS altitude of 414.3 km, the distance between JEM-GLIMS nadir point and Syowa station and JEM-GLIMS nadir point to Kuju station is 7135.2 km and 12760.6 km, respectively. Therefore, a wave propagation time from the lightning event to Syowa station and Kuju station are $\Delta t = 28.38$ ms and $\Delta t = 51.82$ ms, respectively. The expected arrival time of the magnetic waves at Syowa and Kuju station would be 03:25:22.411 UT and 03:25:22.435 UT, respectively. As shown in Figure 3.4(b) and 3.4(c), there is a clear transient ELF waveform at the expected arrival time.

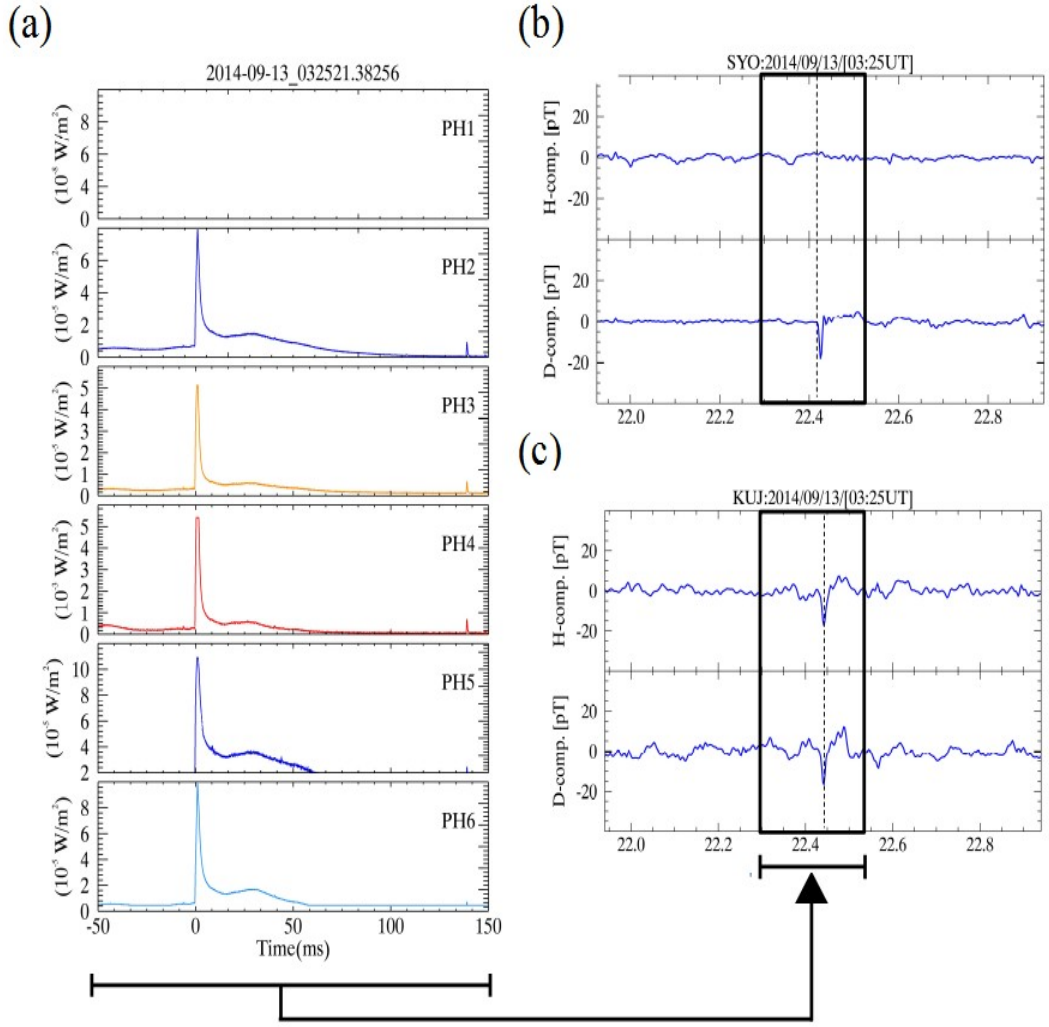

Figure 3.4: (a) Positive cloud-to-ground lightning event detected by JEM-GLIMS optical instruments 03:25:22.383 UT on September 13, 2014. Figure (b) and (c), plot of the ELF magnetic field waveform data acquired at Syowa and Kuju station, respectively.

By considering the component of electromagnetic waves detected by the H-component and D-component and the location of lightning event as shown in Figure 3.5. This lightning event was identify to be a -CG discharge. Then, the logarithmic of PH intensity ratio, *i.e.*, PH2/PH3, PH5/PH3, PH6/PH3, PH2/PH4, PH5/PH4, PH6/PH4, and the LSI intensity ratio at t = 0 ms of this lightning event was calculated.

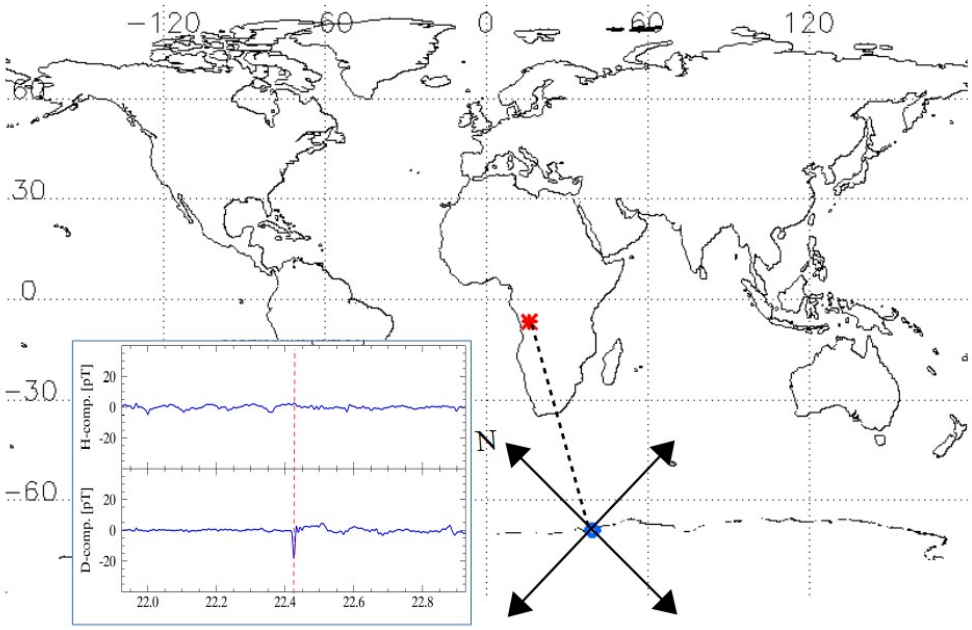

Figure 3.5: Electromagnetic waves signal on H-component and D-component for considering the polarity of CG event of Figure 3.4.

Figure 3.6(a) and (b) show an image of +CG discharges on LSI-1 and LSI-2. The LSI intensity ratio of this identified +CG discharge was also calculated and it presented in Figure 3.6. As shown in Figure 3.6(b) and (d), it is found that the maximum raw count in LSI-2 is located at the pixel X = 90 and Y = 276. Therefore, the value of lightning emission in this pixel, both in LSI-2 and LSI-1 images, was used to estimate the LSI intensity ratio for this +CG discharge.

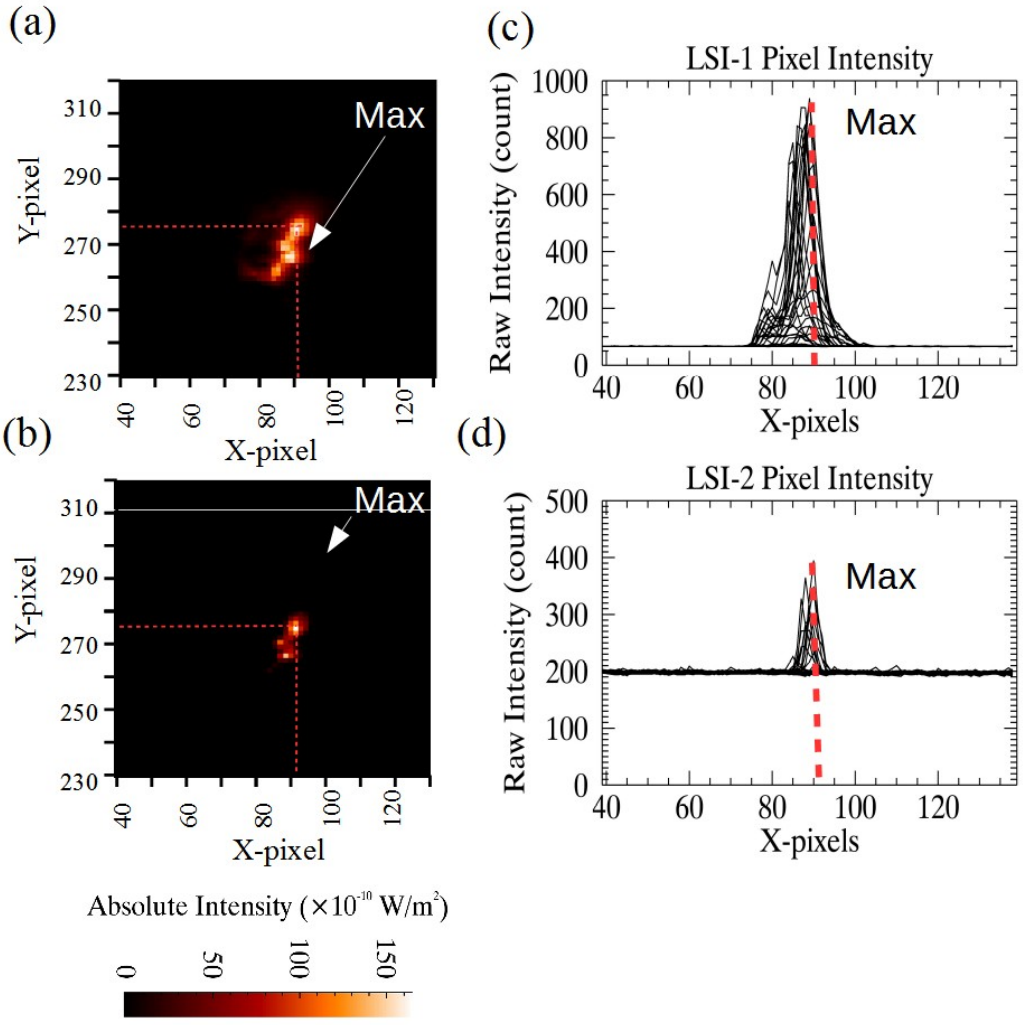

Figure 3.6: An example of (a) lightning discharge image on LSI-1(b) Same as (a) except for LSI-2.Figure (c) and (d) is the plot of raw count for each y-pixel for LSI-1 and LSI-2.

3.1.3 Example of IC discharge

An example of the IC lightning event is shown in Figure 3.7. This event was observed at 08:10:46.352 UT on March 12, 2014, where JEM-GLIMS was located at (76.238°W, 3.891°S) over South America. Figure 3.7(a) illustrates that, PH2-PH6 detected lightning emissions. Figure 3.7(b) and 3.7(c) is a plot of ELF magnetic field waveform data obtained at Syowa and Kuju stations between 08:10:45.500-08:10:46.900 UT.

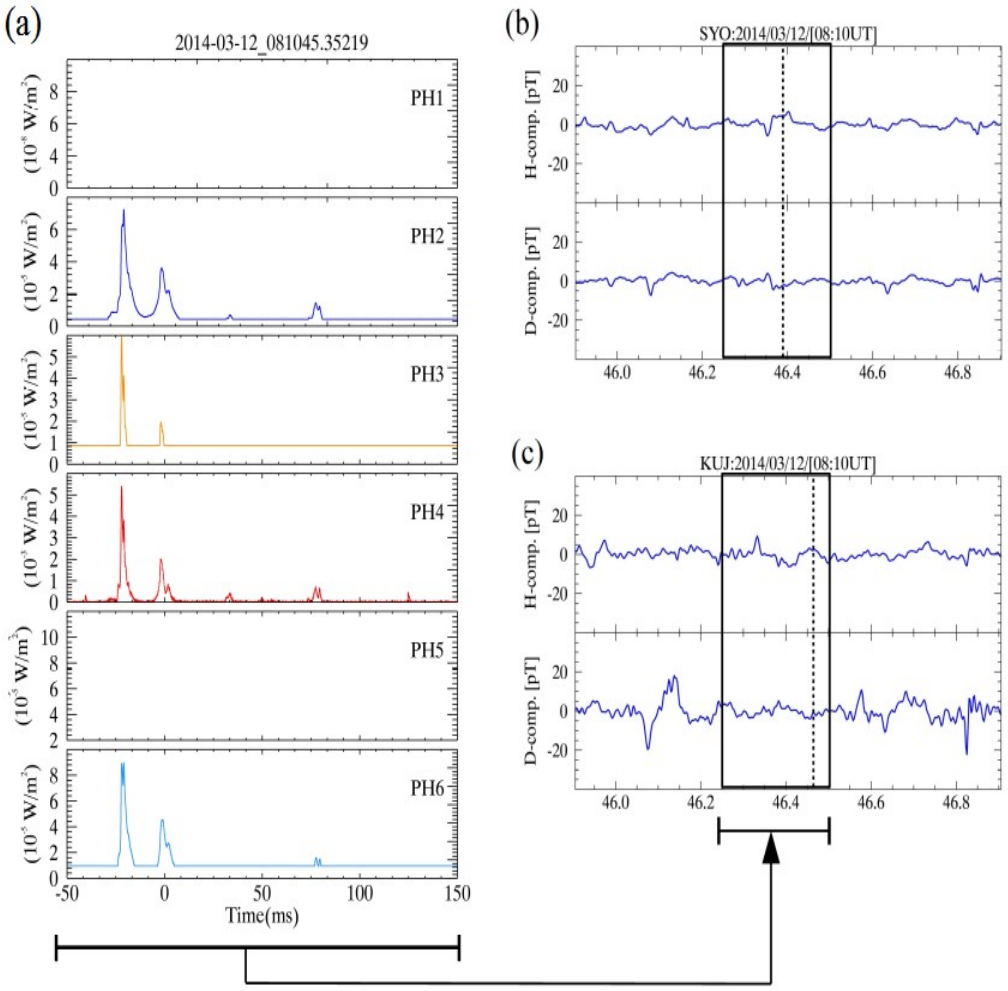

Figure 3.7: (a) IC Lightning event detected by JEM-GLIMS optical instruments at 08:10:46.352 UT on 12 March 2014. Figure (c) – (d), plot of the ELF magnetic field waveform data acquired at Syowa and Kuju station, respectively.

Considering the optical propagation time of 1.35 ms from the assumed light source at the altitude of 10 km to the JEM-GLIMS altitude of 414.3 km, the distance between JEM-GLIMS nadir point and Syowa station and JEM-GLIMS nadir point to Kuju station is 10605.3 km and 15713.9 km, respectively. Therefore, the wave propagation time from this lightning to Syowa station and Kuju station is Δt = 44.19 ms and Δt = 65.47 ms, respectively. The expected arrival time of

the electromagnetic waves at Syowa and Kuju station would be 08:10:46.396 UT and 08:10:46.417 UT, respectively. As shown in Figure 3.7(b) and 3.7(c), there is no clear transient SR waveform at around the PH trigger time. Consequently, we concluded that this lightning event is an IC lightning. Then, the logarithmic of PH intensity ratios and LSI intensity ratio at t = 0 ms of this lightning event is also calculated.

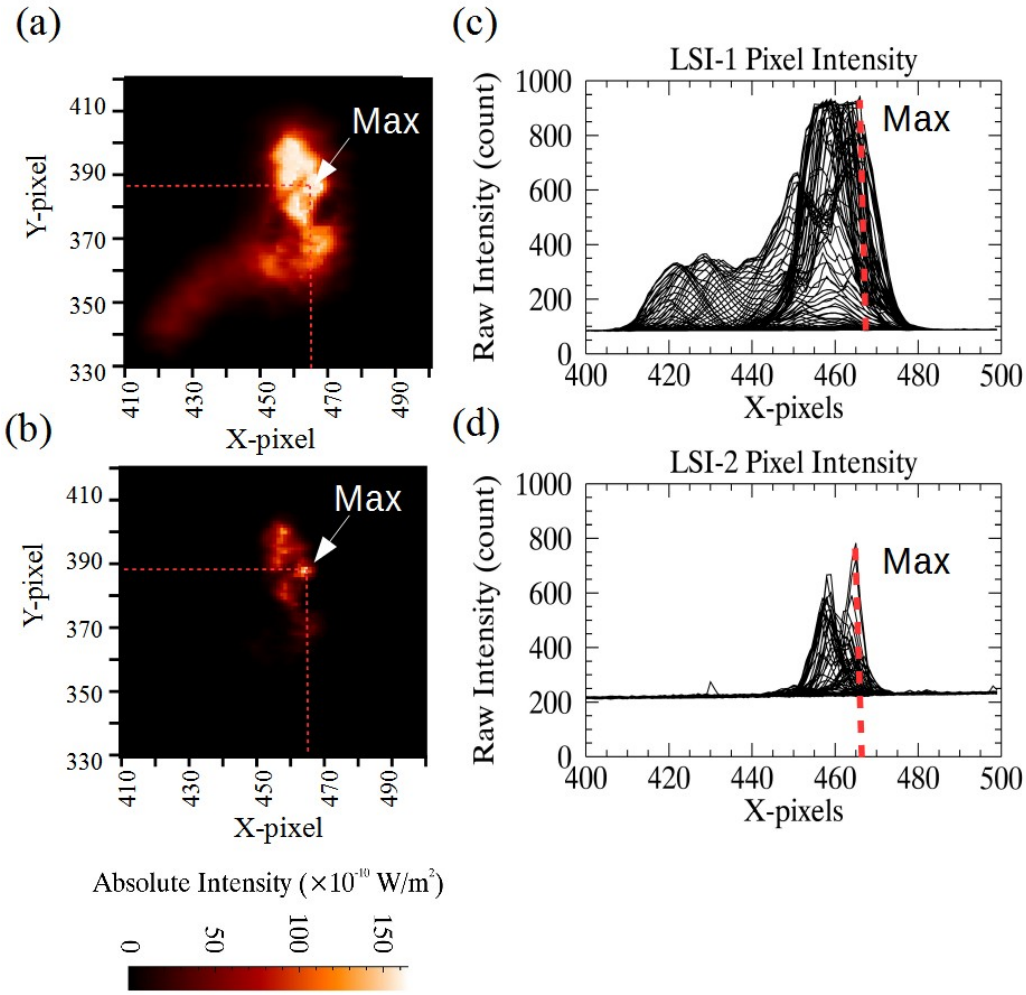

Figure 3.8: An example of (a) lightning discharge image on LSI-1(b) Same as (a) except for LSI-2.Figure (c) and (d) is the plot of raw count for each y-pixel for LSI-1 and LSI-2.

Figure 3.8(a) and (b) show an image of IC discharges on LSI-1 and LSI-2. The LSI intensity ratio of this identified IC discharge was also calculated and it presented in Figure 3.8. As shown in Figure 3.8(b) and (d), it is found that the maximum raw count in LSI-2 is located at the pixel X = 466 and Y = 388. Therefore, the value of lightning emission in this pixel, both in LSI-2 and LSI-1 images, was used to estimate the LSI intensity ratio for this IC discharge.

3.2 PH intensity ratio and LSI intensity ratio of lightning discharges

Figure 3.9. Figures 3.9(a)-3.9(f) illustrates the histogram of the logarithmic of the PH intensity ratio ,*i.e.*, PH2/PH3, PH5/PH3, PH6/PH3, PH2/PH4, PH5/PH4, PH6/PH4, for the identified 75 IC, 102 +CG, and 394 -CG discharges. In those mentioned in figures 3.9, PH intensity ratios are indicated on the horizontal axis in logarithmic scale while the vertical axis is the number of events. The median and standard deviation of the logarithmic PH intensity ratios are also calculated and they are concluded in Table 3.1.

As shown in Figure 3.9 and table 3.1, the result reveals that the PH intensity ratio of the IC discharges is the highest in all cases of PH intensity ratios. It is also found that the PH intensity ratio of -CG discharges is always the lowest value compared with others while the PH intensity ratio of +CG discharges is smaller than those of IC discharges but larger than those of -CG discharges. The LSI intensity ratios of the identified JEM-GLIMS lightning events were also calculated, and the histogram of the calculated LSI intensity ratios is presented in Figure 3.10. Both the median and standard deviation are also calculated and these number are presented in Table 3.1.

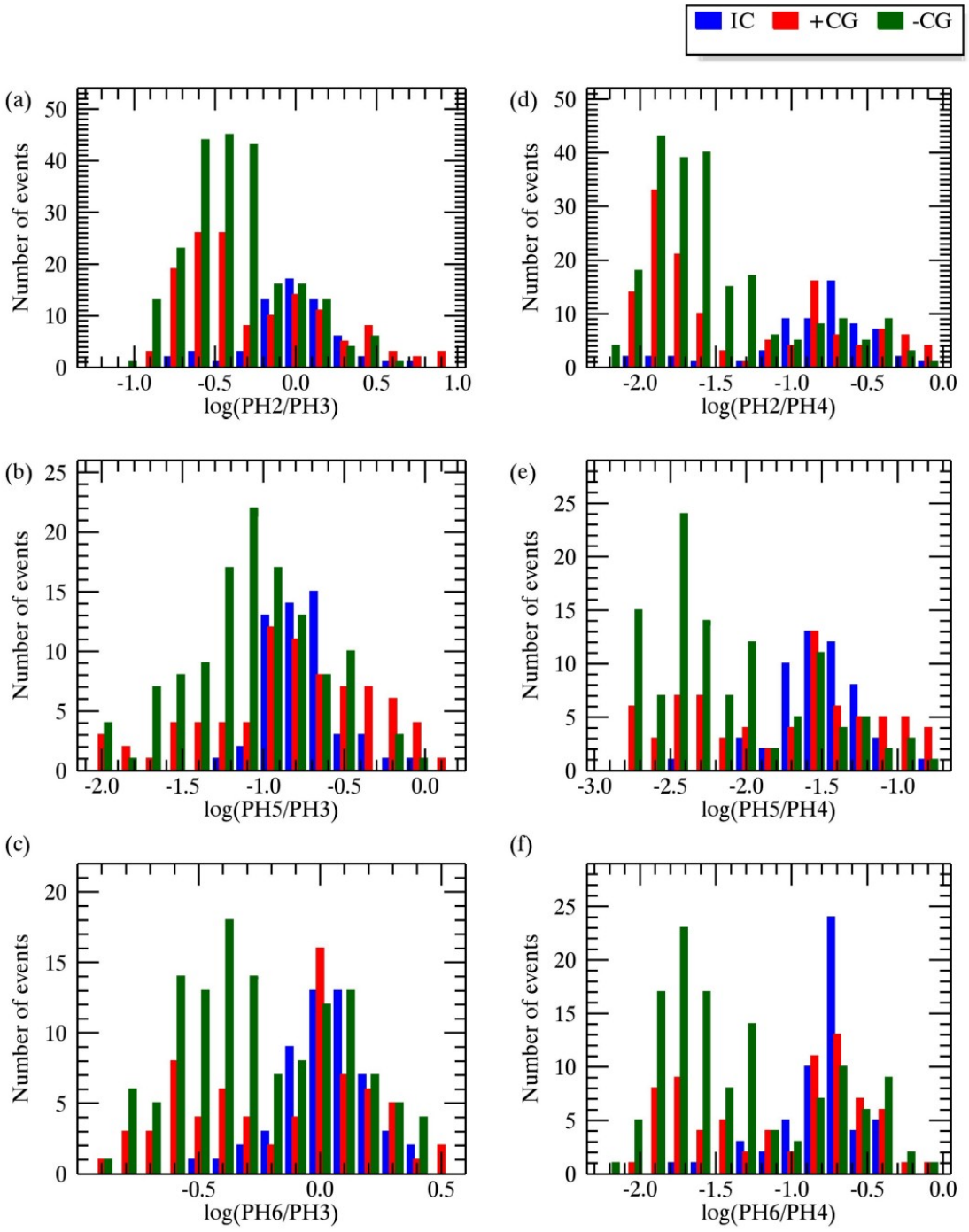

Figure 3.9: Histograms of the PH intensity ratios with the logarithmic scale. The blue, red and green bars correspond to the ratio of IC, +CG, and -CG discharges, respectively. In this figure, (a)-(f) are the ratios of PH2/PH3, PH5/PH3, PH6/PH3, PH2/PH4, PH5/PH4, and PH6/PH4, respectively.

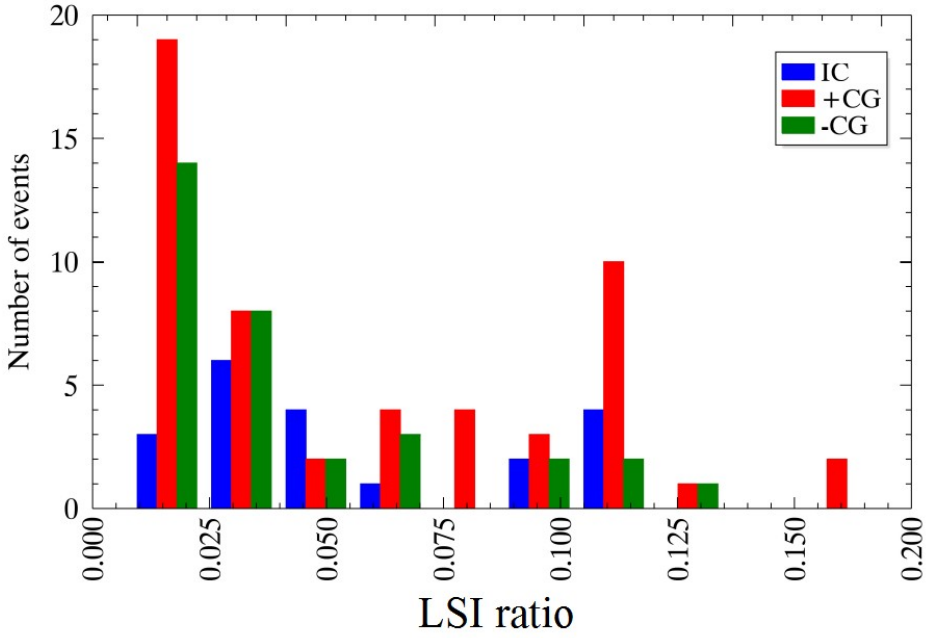

Figure 3.10: Histograms of the LSI intensity ratio of 45 IC (blue), 12 +CG (red), and 17 -CG (green) discharges.

The number of lightning events used in the LSI intensity ratio calculation is smaller than the one used in the PH intensity ratio calculation analysis due to the LSI-2 could detect lightning optical emissions only 107 from 571 lightning events. The reason is that the lightning emissions at 762 nm were severely attenuated by the atmospheric oxygen molecules; Consequently, LSI-2 would not be able to collect all 521 of lightning events in the calculation of LSI intensity ratio. As illustrated in Figure 3.5, the median values of IC, +CG and -CG discharges were 0.063, 0.049, and 0.038, respectively. It is clear that the characteristics of the LSI intensity ratio has a good agreement with the result of PH intensity ratio, *i.e.*, the LSI intensity ratio of IC and +CG discharges is higher than those of -CG discharges.

Table 3.1: Summary of the PH and LSI intensity ratios of 75 IC, 102 +CG, and 394 -CG discharges. In this table, the median value of the logarithmic PH and LSI intensity ratios and the standard deviation (σ) are listed.

	+CG		IC		-CG	
	median	σ_{+CG}	median	σ_{IC}	median	σ_{-CG}
log(PH2/PH3)	-0.33	0.48	0.097	0.32	-0.36	0.32
log(PH5/PH3)	-0.72	0.57	-0.62	0.23	-1.0	0.46
log(PH6/PH3)	0.019	0.38	0.099	0.17	-0.27	0.36
log(PH2/PH4)	-1.5	0.67	-0.71	0.48	-1.6	0.49
log(PH5/PH4)	-1.5	0.68	-1.44	0.28	-2.2	0.55
log(PH6/PH4)	-0.79	0.55	-0.68	0.29	-1.5	0.54
LSI-2/LSI-1	0.049	0.068	0.063	0.057	0.038	0.053

The difference in PH and LSI intensity ratio between IC and -CG discharges would be explained by the difference of the light source altitude of lightning discharges since the atmospheric transmittance in the blue and red wavelengths from lightning discharge are different as discussed in Section 2.3. The normal discharge channels of IC discharges tend to occur in the middle of the thunderclouds (López et al., 2016) while the discharge channel of -CG discharges tends to occur at lower altitudes or near the cloud-base (Ballarotti and Saba, 2005; Sun et al., 2016; Lyu et al., 2016). Consequently, both blue and red emissions from the IC discharges escapes to the JEM-GLIMS optical instruments with a relatively low attenuation rate. On the other hand, only red emission from -CG discharges mainly escapes to the JEM-GLIMS optical instruments due to the strong attenuation rate of blue emission in the atmosphere. Therefore, the PH and LSI intensity ratio of IC discharges are higher than that -CG discharges. The PH and LSI intensity ratio of +CG discharges, however, were not in an agreement with the assumption in

Section 2.3 because it smaller then those of IC discharges. The main cause of the discrepancy is due to the +CG discharges which initiate from the lower positive charge region (LPCR). Although the discharge channels of +CG discharges tend to occur at a high altitude between the main positive charge region near the cloud top and the ground (Rust et al., 1981; Lu et al., 2012), some +CG discharges arise from the LPCR in the thundercloud (Pawar and Kamra, 2004; Stolzenburg et al., 1998c,a,b). The discharge channel of these +CG discharges locates at the lower altitude than the normal +CG discharges. Consequently, the median PH intensity ratio of +CG discharges is smaller than those of IC discharges but still higher than those of -CG discharges.

As shown in Figures 3.9, Figure 3.10 and Table 3.1, the distribution of the PH and LSI intensity ratios of the IC, +CG, and -CG discharges shows the clear difference. Consequently, these PH and LSI intensity ratios are useful indicators for distinguishing the discharge type of 6532 events and 1251 CG events obtained by JEM-GLIMS observation.

3.3 Regional Dependence of Z-ratio

Figures 3.11 shows the global distribution of the identified IC, +CG, and -CG discharges. Next step, in order to estimate regional dependences of the Z-ratio, the number of lightning discharges in each $3.0^\circ \times 3.0^\circ$ grid are counted. Then, the Z-ratio would be calculated on every square boxes.

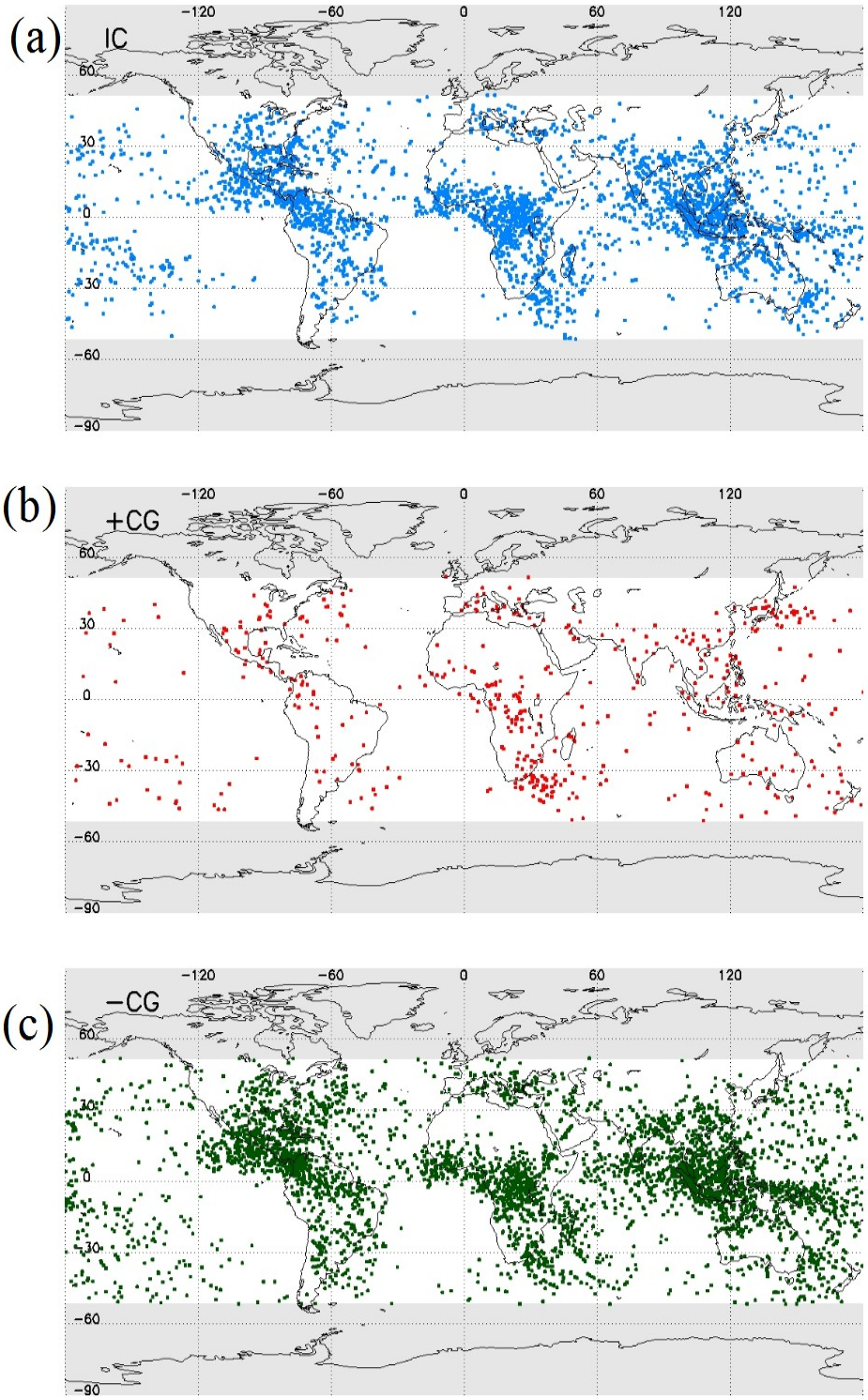

Figure 3.11: Global distribution of the identified IC, +CG,and (c) -CG discharges detected by JEM-GLIMS in the period from November 2012 – August 2015

The spatial distribution of the Z-ratio is presented in Figure 3.12. It is found that the Z-ratio varies from 0.2 to 17.1 and that the average value is equal to 1.6, even though Mackerras and Darveniza (1994) estimated the value of 1.9 of mean Z-ratio from the analysis of the lightning data obtained by the CGR3 network. Interestingly, the result also shows that the higher Z-ratio tends to occur over the continental rather than the ocean. The average value Z-ratio over the continental and oceanic areas were 1.7 and 1.1, respectively. It should be noted that the definition of the continental and the oceanic areas used in this study is same as what Mackerras et al. (1998) introduced. The appropriate explanation for this finding may be, the thundercloud structure and the electrical charge distributions in thunderclouds are different in the continental and oceanic thundersclouds. The lightning occurrence frequency relates to the strong upward velocity in thunderclouds and the convective available potential energy (CAPE) (Lhermitte and Williams, 1983). The strong CAPE are usually observed in the continental air masses, while the weaker CAPE are usually observed in the oceanic air masses. The difference in the CAPE energy between continental and ocean causes the weaker updrafts in the oceanic thunderclouds than the continental thunderclouds (Zipser, 1994; Zipser and Lutz, 1994). The weaker updrafts in the oceanic thunderclouds cause a less efficient charge separations (Takahashi, 1984; Norville et al., 1991; Stolzenburg et al., 1998c,a,b). Thus, the main negative charge region inside the oceanic thunderclouds tends to locate at the lower altitude than that inside the continental thunderclouds, which enhances the occurrence rate of CG discharges. However, this assumption needs to be verified in a future study.

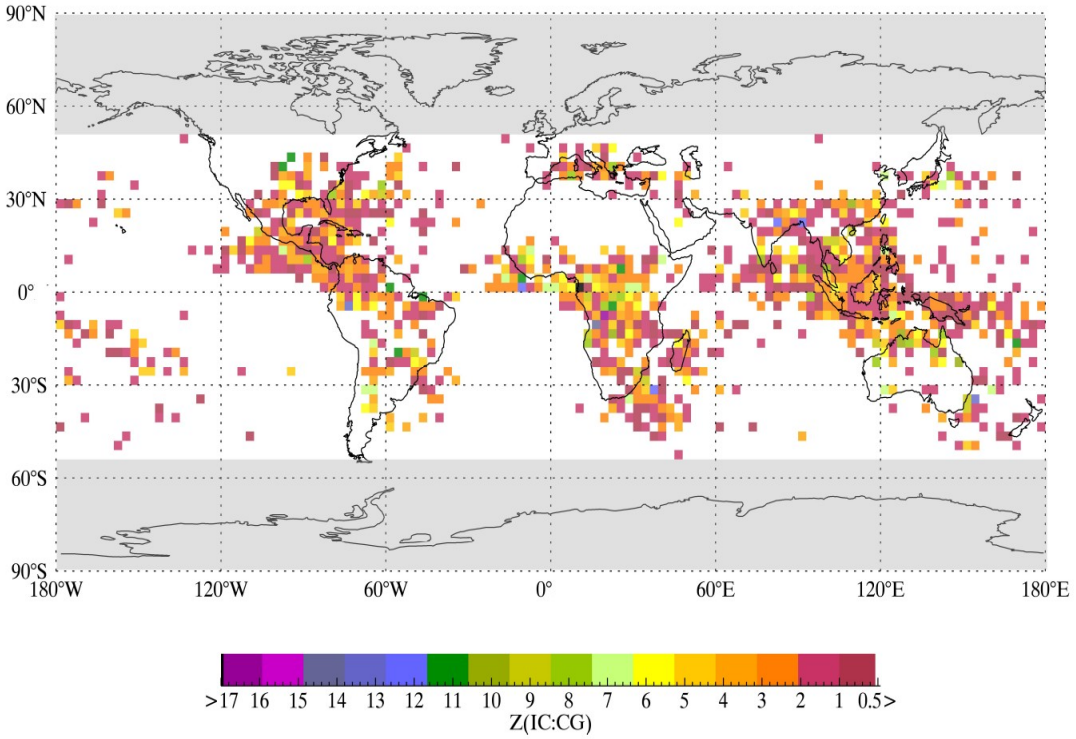

Figure 3.12: Spatial distribution of the Z-ratio over the latitudinal range of ±51° used for calculating the occurrence number of IC discharges

3.4 Seasonal Dependence of Z-ratio

Figures 3.13(a)-3.13(d) show the global map of the Z-ratio in the period of December - February, March - May, June - August, and September - November, respectively. In the period of December - February, the pixels where the Z-ratio exists can be found mainly in the southern hemisphere, especially, between the equator to 30°S, as shown in Figure 3.13(a). While, in the period from June - August, these pixels can be found mainly in the northern hemisphere between the equator to 30°N, as shown in Figure 3.13(c). However, the distribution of those pixels in the period of March - May and September - November can be found both in the northern and southern hemispheres, and they are mainly located in the latitudinal range of 30°S - 30°N, as shown in Figures 3.13(b) and 3.13(c). It is found that in the northern tropics (from 0° to 20° N) the average Z-ratio value

in the local summer (June - August) is 2.4 times higher than that in the local winter (December - February). Similarly, it is found that in the southern tropics (0° to 20°S) the average Z-ratio value in the local summer (December - February) is 2.3 times higher than that in the local winter (June - August). In contrast, the averaged Z-ratio values in the northern and southern hemispheres in the period of March - May are almost comparable to those in the period of September - November.

A possible explanation for the difference of Z-ratio values in the local summer and winter may be related to the altitude difference of the main negative charge region in the thunderclouds. As we describe in Section 3.2, the height of the main negative charge region in thunderclouds is the function of the freezing levels and CAPE. In the local summer, the ground temperature is higher compared to the local winter. Consequently, the main negative charge region tends to locate at the higher altitude and tend to be closer to the main positive charge region. The shorter distance between the main positive and negative charge regions enhances the occurrence frequency of IC discharges than CG discharges, which brings the enhancement of Z-ratio.

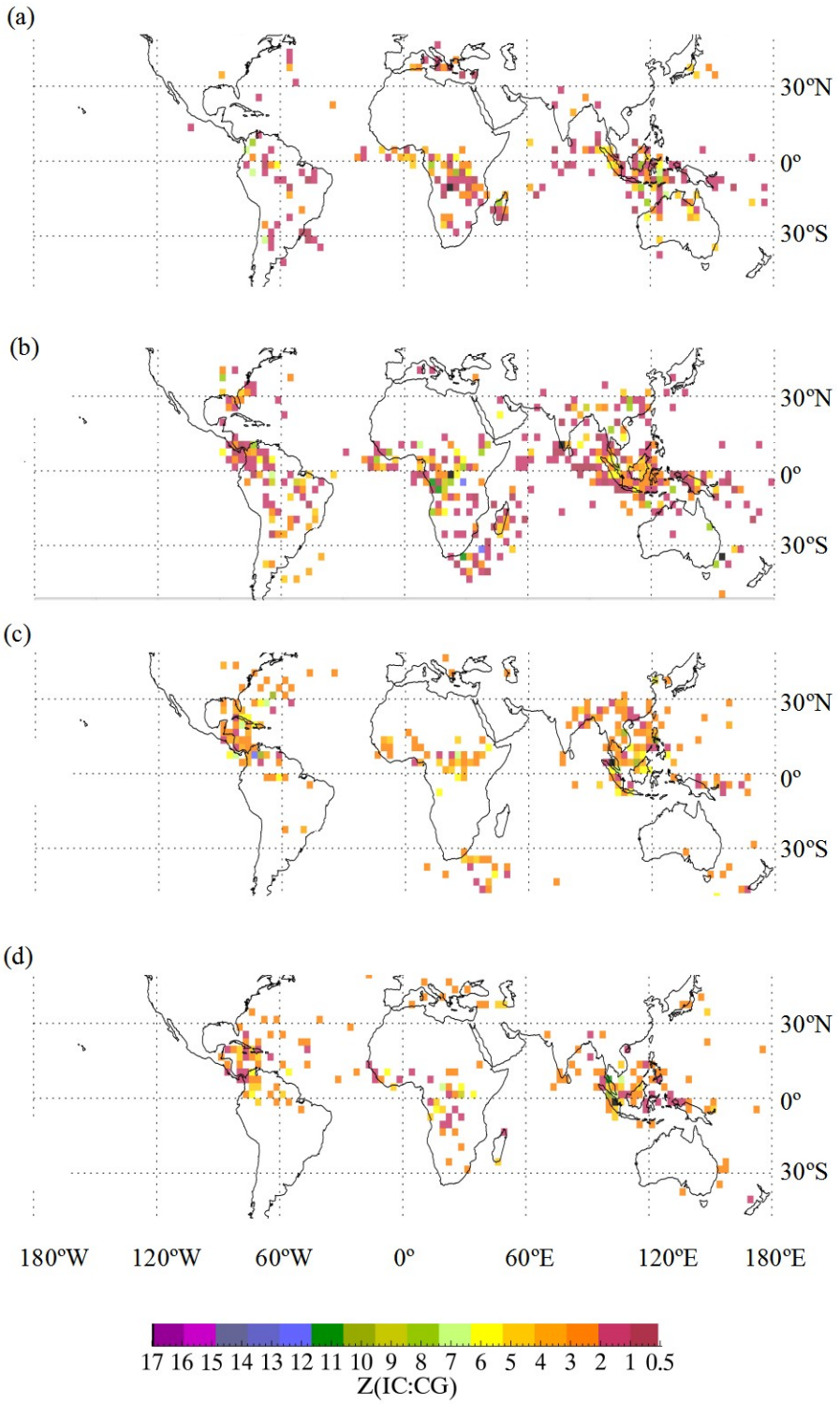

Figure 3.13: Spatial distribution of the Z-ratio in the period of (a) December-February, (b) March-May, (c) June-August, and (d) September-November, respectively.

3.5 Latitudinal Dependence of Z-ratio

The zonal-mean Z-ratio was calculated, and its latitudinal dependences in the northern and southern hemispheres are plotted in Figures 3.14(a) and 3.14(b), respectively. The vertical bars attached to each data point represent the standard deviation ($\pm 1\sigma$ level) of the Z-ratio variation in each latitudinal range. It is found that the Z-ratio gradually decreases from the equator to the higher latitude from 2.9 to 0.2 in the northern hemisphere as shown in Figure 3.14(a), while from 2.9 to 0.5 in the southern hemisphere as shown in Figure 3.14(b). These characteristics are well comparable to the results reported by Pierce (1970), Prentice and MacKerras (1977), Mackerras and Darveniza (1994), Mackerras et al. (1998), and Boccippio et al. (1999).

The comparison between Z-ratios derived from this study and previous studies are summarized in Table 3.2. As shown in this table, the mean value of the Z-ratio, which is shown in the bracket in the latitudinal range of 20°S-20°N, is estimated to be 2.5 with a standard deviation of 0.46. This value is smaller than the tropical (20°S-20°N) Z-ratio (6.2 and 5.9) estimated by Pierce (1970) and Prentice and MacKerras (1977), while this value well agrees with the Z-ratio estimated by-Mackerras and Darveniza (1994), where the mean Z-ratio in the tropics was 2.3. At the latitudinal range of 20°N - 40°N and 20°S - 40°S, the mean value of Z-ratio is 1.9 with a standard deviation 0.33, again it is considerably lower than the ratio of 4.2 by Prentice and MacKerras (1977) and 2.2 by Mackerras and Darveniza (1994) in the same latitudinal range. As for the result of Z-ratio in the latitudinal range of 40°N - 60°N and 40°S - 60°S, the mean Z-ratio value derived from this study is 1.1. It is lower than the ratio of 1.3 by Mackerras and Darveniza (1994) in this latitudinal range.

There are two possible explanations for this disagreement. First, there were limitations of the visual and flash counter observations in the previous studies. The obtained results were not reliable in the high lightning activity regions because

of the difficulty in distinguishing between IC and CG discharges. Second, there were limitations of the observation areas. In the previous studies, Z-ratios were estimated from the lightning data obtained over the land region, and they did not include the ratios over the oceanic areas where the Z-ratios are believed to have lower values than those over land regions as we presented in Section 3.1.

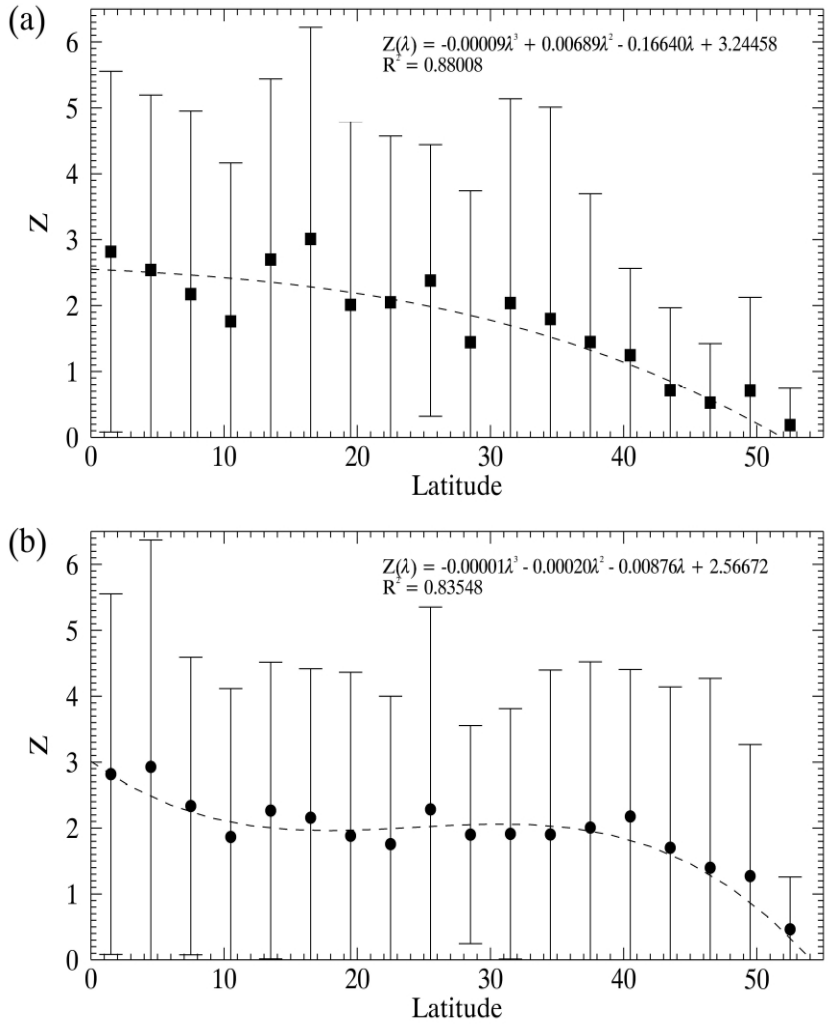

Figure 3.14: Latitudinal dependences of the Z-ratio in the northern hemisphere. (b) Same as (a) except for the southern hemisphere. In these figures, the zonal-mean Z-ratio values are calculated every 3° latitudinal range and plotted. Vertical bars at each data point represent the $\pm 1\sigma$ of Z-ratio values

Table 3.2: Comparison between the Z-ratios derived from this study and the previous studies.

	This study	Pierce (1970)	Prentice and MacKerras (1977)	Rivas Soriano and Dávila (2007)	Mackerras et al. (1998)
coverage	50°S-50°N	-	-	50°S-54°S	50°S-50°N
20°S-20°N	2.9-1.7(2.5)	9.0-4.4(6.2)	6.3-5.2(5.9)	-	3.4-0.5(2.3)
20°N-40°N,20°S-40°S	2.4-1.2(1.9)	4.4-2.8(3.5)	5.2-3.1(4.2)	6.1-2.2(3.5)	3.8-1.1(2.2)
40°N-60°N,40°S-60°S	1.9-0.19(1.1)	2.8-2.2(2.5)	3.1-2.0(2.4)	-	1.5-1.0(1.3)

* latitudinal range = 40°N-51°N and 40°S-51°S

3.6 Relationship between Z-ratio and +CG discharges

The relationship between Z-ratio and the percentage of occurrence of IC, -CG, and +CG discharges at each $3.0^{o}\times3.0^{o}$ grid box is presented in Figure 3.15. In Figure 10(a), each data point shows the pairwise value of Z-ratio and the percentage of IC discharges for each $3.0^{o}\times3.0^{o}$ grid block. The Z-ratio in Figure 3.15 is the corresponding to Figure 3.12. Figure ??(b) and ??(c) same as ??(a) except for +CG and -CG discharges, respectively. The previous studies have reported a significant correlation between Z-ratio and +CG discharges. They found that the high Z-ratio values would be founded in the areas where the occurrence percentage of +CG discharges is high (Boccippio et al., 1999; Pinto et al., 2003; de Souza et al., 2009). In this study, however, it was found that the occurrence percentage of +CG discahrges decreases when the Z-ratio increases as illustrates in Figure 3.15(b). It was also found the clear relations between the increasing Z-ratio and the increasing occurrence percentage of IC discharges (Figure 3.15(a)) and between the decreasing Z-ratio and the increasing occurrence percentage of -CG discharges (Figure 3.15(c)). The relationship between Z-ratio and occurrence percentage of IC, +CG and -CG discharges illustrates that the increase of Z value in thunderclouds is enhanced by the increasing rate of IC discharges.

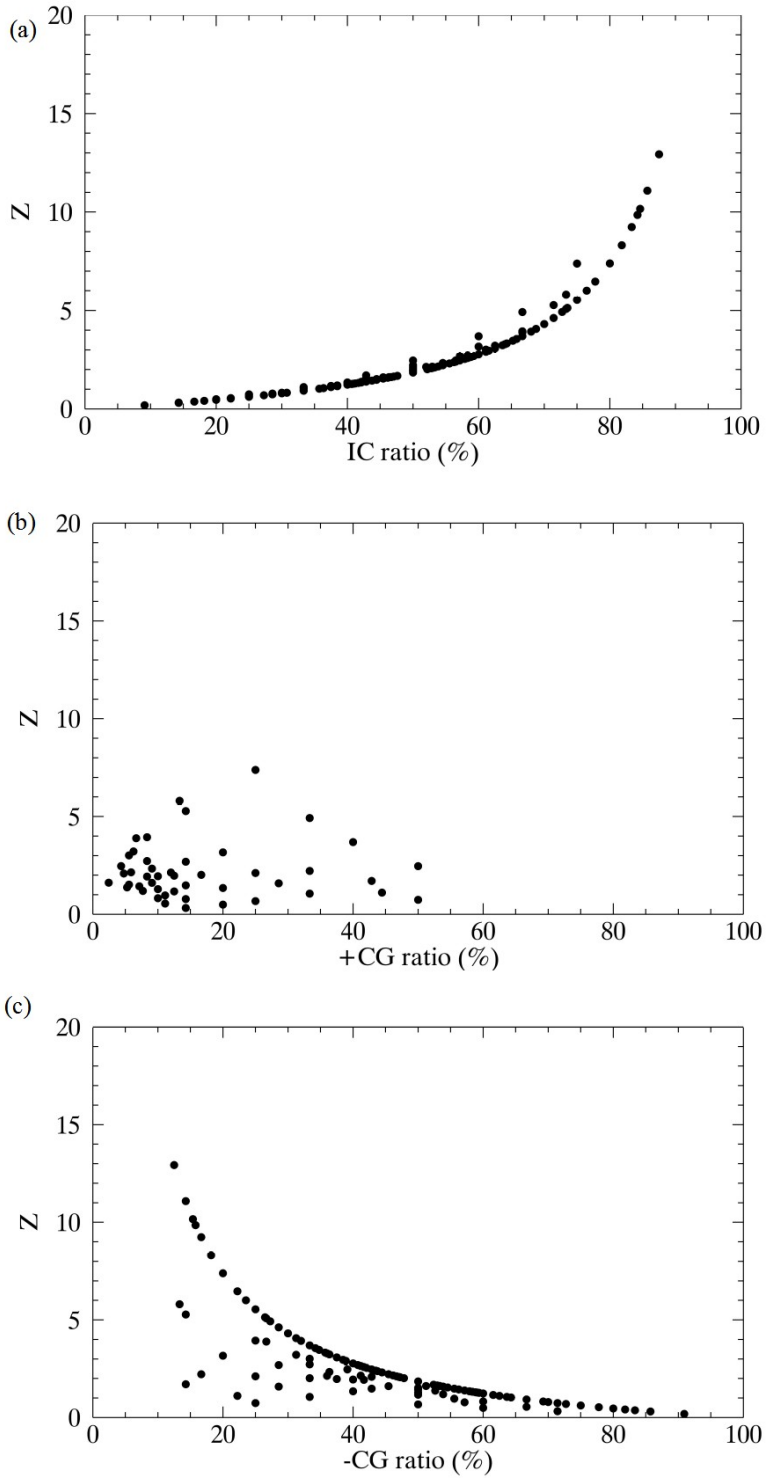

Figure 3.15: Scatter plot of the estimated Z-ratio and the occurrence percentage of (a) IC discharges, (b) +CG discharges, and (c) -CG discharges, respectively.

Chapter 4

The 3-dimensional model of the global electric circuit

4.1 Calculation of the upward electric current by lightning discharges

The flow chart showing how the input parameters of the global electric circuit were calculated is summarized in Figure 4.1. As a first step, in order to estimate the number of IC, +CG, and -CG discharges, CG discharges data provided by WWLLN was divided into $0.2^\circ \times 0.2^\circ$ grid as shown in Figure 4.2(a). Note that the grid cite $0.2^\circ \times 0.2^\circ$ was used in this study correspondence to the size of a typical thundercloud $i.e., \sim 20km$ (Rycroft and Odzimek, 2010). Then, using lightning data provided by WWLLN (Figure 4.2(a)) and the detection efficiency map of WWLLN (Figure 4.2(b)), the global occurrence number of CG discharges was calculated by:

$$N_{CG} = \sum_{i=0}^{i=1800} \sum_{j=0}^{j=900} \frac{N_{CG_{ij}}}{DE_{ij}} \tag{4.1}$$

where $DE_{i,j}$ is detection efficiency of WWLLN and $N_{CG_{ij}}$ is the occurrence number of CG discharges of cell i,j, respectively.

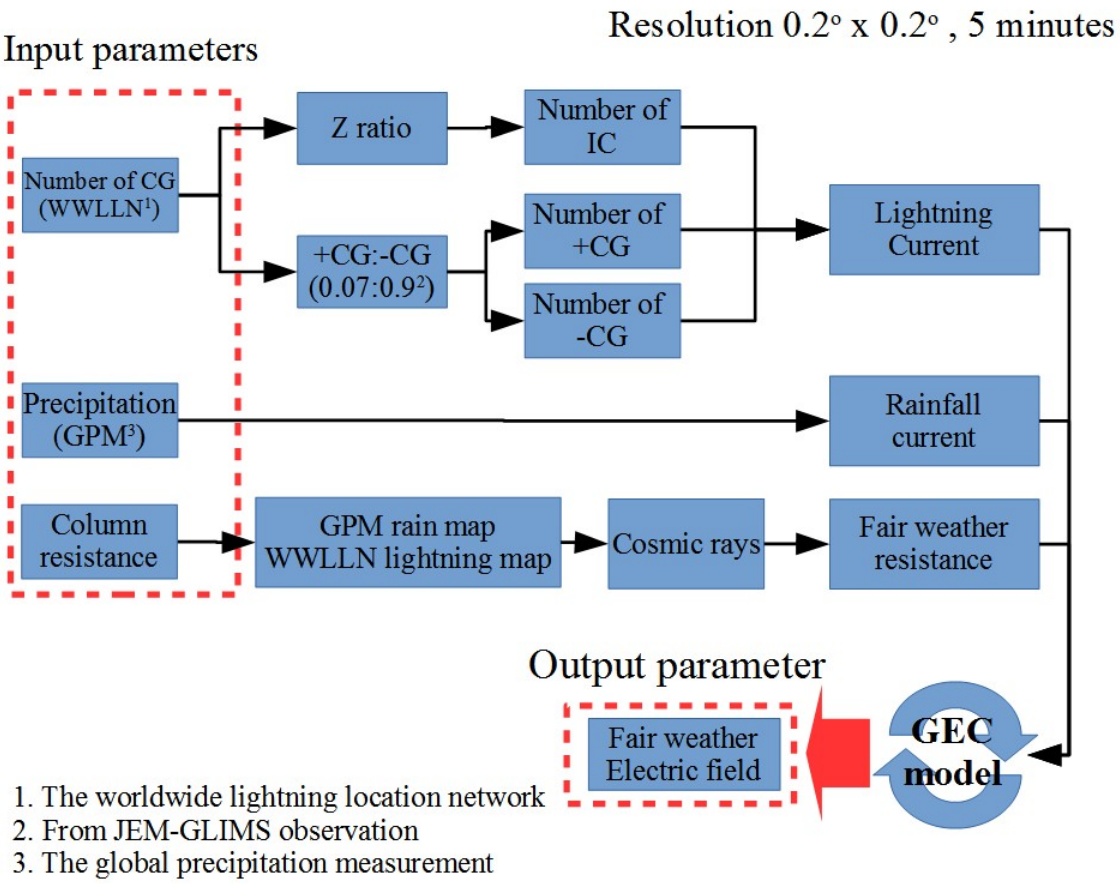

Figure 4.1: (a) Flow chart showing how the input parameters of the global electric circuit were calculated using CG lightning data provided by WWLLN, rainfall data provided by GPM, and the average column resistance map .

Secondly, using CG lightning data provided by WWLLN and the global distribution map of Z-ratio (Figure 3.12), the number of IC discharges (N_{IC}) was calculated by,

$$N_{IC} = \sum_{i=0}^{i=1800} \sum_{j=0}^{j=900} Z_{i,j} \frac{N_{CG_{ij}}}{DE_{ij}} \tag{4.2}$$

where $Z_{i,j}$ is the Z-ratio of cell i,j. After that, the occurrence number of +CG discharges (N_{+CG}) and -CG discharges (N_{-CG}) was finally calculated by using the ratio between +CG and -CG discharges (0.07:0.93) which is introduced by Rakov et al. (2004).

$$N_{+CG} = 0.07 N_{CG} \tag{4.3}$$

$$N_{-CG} = 0.93 N_{CG} \tag{4.4}$$

As a next step, in order to estimate the total upward current to the ionosphere by lightning, the currents waveform of lightning discharge was used (Plooster, 1971; Heidler et al., 1999; Javor, 2009). Then, the total current was calculated by:

$$\begin{aligned} I_L = (N_{IC} \int_0^{t_{IC}} I_{P_{IC}} e^{-t/\tau} dt + N_{+CG} \int_0^{t_{+CG}} I_{P_{+CG}} e^{-t/\tau} dt \\ + N_{-CG} \int_0^{t_{-CG}} I_{P_{-CG}} e^{-t/\tau} dt)/T \end{aligned} \tag{4.5}$$

where $I_{P_{IC}}$, $I_{P_{+CG}}$, and $I_{P_{-CG}}$ are a peak current of IC, +CG, and -CG discharges respectively, while t_{IC}, t_{+CG}, and t_{-CG} are a decay time of IC, +CG, and -CG discharge respectively. The important input parameter for calculating the lightning current were summarised in Table 4.1. In this study, the lightning occurrence number was calculated in every 5 minutes. Therefore the time resolution T is 300 seconds was also used for calculating the currents.

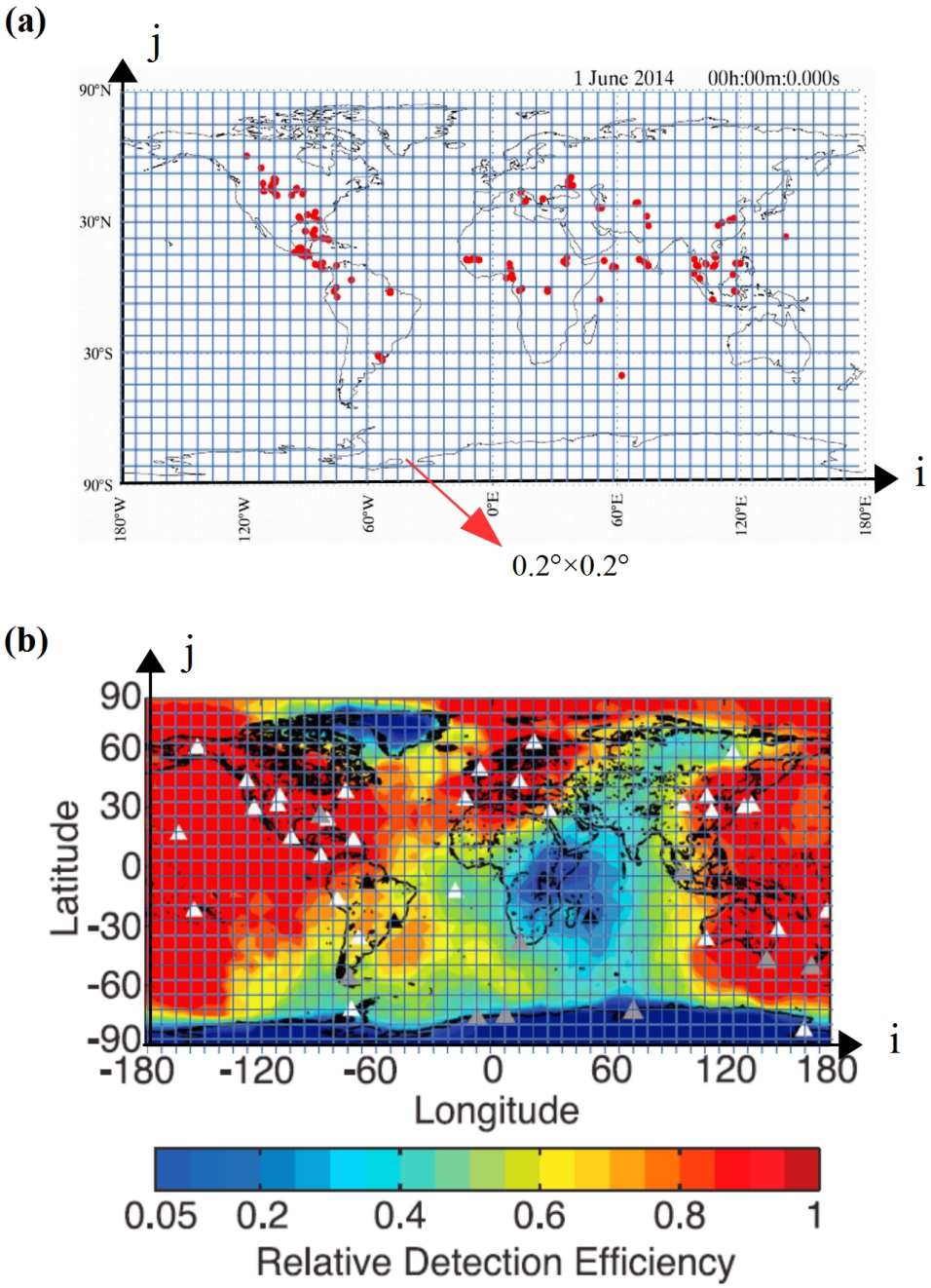

Figure 4.2: (a) The occurrence number of CG discharges provided by WWLLM were composited into a $0.2° \times 0.2°$ cell for estimating the occurrence number of +CG, -CG, and IC lightning. (b)The relative detection efficiency of WWLLN. Stations are shown as triangles with operational stations in white, non-operational in black, and operational for part of the day in grey (Hutchins et al., 2012).

Table 4.1: The input parameters for calculating the upward current to the ionosphere by lightning discharges.

	Ip (kA)	Decay time (μs)	λ (μs)
IC	7	20	5
+CG	35	230	40
-CG	30	75	15

4.2 Calculation of the upward electric current by rainfall

As mentioned in Introduction, global rainfall is a fundamental current source in the global atmospheric electric circuit (Wilson, 1921; Williams et al., 2000). The mean annual global rainfall is estimated to be about 1000 mm (Legates and Willmott, 1990; Michaelides et al., 2009), and it generates around 600-800 A of electric current to the ionosphere (Mareev et al., 2008). In this study, the upward electric current to the ionosphere generated by rainfall was estimated from the precipitation data provided by the Global Precipitation Measurement (GPM) mission, which provides the most recent global estimates of rainfall at high spatial and temporal resolutions.

The GPM project is a joint mission of international space agencies to make observations of Earth's rainfall. This project provides global rainfall data to assist researchers in improving weather forecasting and studying global climate (Kidd and Huffman, 2011). The main observatory instruments on the satellites of this project are the Dual-Frequency Precipitation Radar (DPR) and the GPM Microwave Imager (GMI) (Hou et al., 2014). These instruments estimates the sizes and density of particles inside thunderclouds and then converse them to a rainfall rate (Liu et al., 2008). For more detailed information and operation of GPM

project can be found in the paper of Flaming (2005); Kidd and Huffman (2011); Hou et al. (2014)

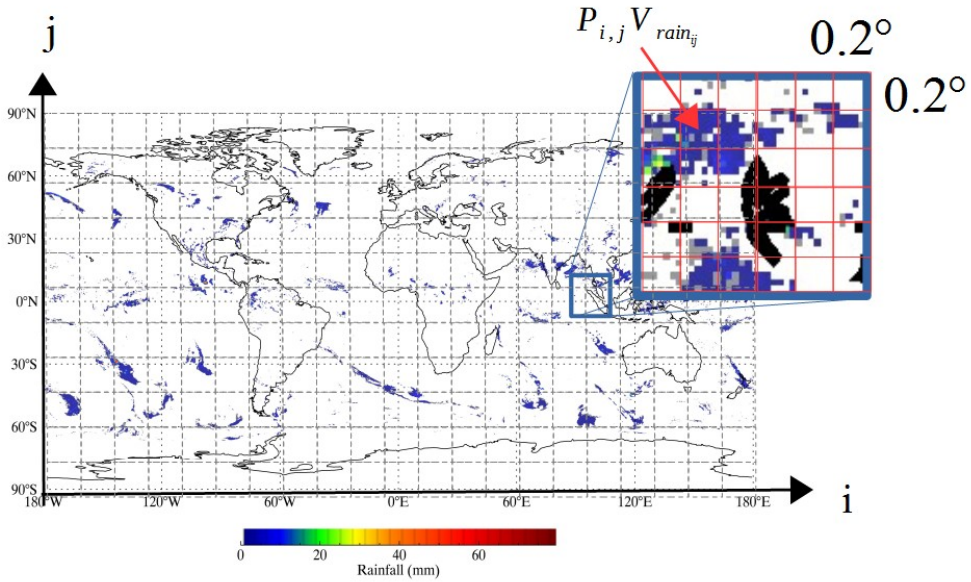

Figure 4.3: Example of the rainfall data provided by the GPM on June 4, 2014, which was used to calculate the upward electric current to the ionosphere.

In this study, GPM data with 30 min temporal and 0.1° spatial resolution was used for estimating the upward current produced by rainfall. As shown in Figure 4.3, rainfall volume (mm) in each $0.2^\circ \times 0.2^\circ$ grid was used to calculate electric current using the equation introduced by (Soula and Chauzy, 1997). An electric current produced by rainfall was calculated by:

$$I_P = \sum_{i=0}^{i=1800} \sum_{j=0}^{j=900} \rho A_{i,j} V_{Rain_{i,j}} \tag{4.6}$$

where V_{Rain} is the rainfall (mm), and ρ is a specific charge density. The specific charges density for precipitation over continental and oceanic cell are 0.42 nA/m^{2}mm^2 and 1.21 nA/m^{2}mm^2 Mach et al. (2009). The parameter A in the equation is an area of a $0.2^\circ \times 0.2^\circ$ cell. Note that, rainfall contributed from

clouds which cloud top temperature grater than the freezing level (273 K) was excluded for calculating the electric current generated by rainfall because these clouds do not produce electric charges due to its absence of ice particles (Liu et al., 2008).

4.3 Calculation of the fair weather resistance

On of the crucial parameter for calculating the contribution of lightning and rainfall to the global electric circuit is the fair-weather resistance. Using the rainfall data provided by the GPM and lightning data provided by the WWLLN, a cell where has a lightning event or/and rainfall was identified to be a generator cell. Then, the accompanying resistance of the three resistors, as shown in Figure 4.4, was calculated using standard electrostatic theory as

$$R_A = \frac{1}{A_T}\int_{i-1}^{i}\frac{d(h)}{\sigma(h)}\ ;\ i = 20,,80\ and\ h_i - h_{i-1} = 1km \tag{4.7}$$

$$R_T = \frac{1}{A_T}\int_{i-1}^{i}\frac{d(h)}{\sigma(h)}\ ;\ i = 5,,20\ and\ h_i - h_{i-1} = 1km \tag{4.8}$$

$$R_B = \frac{1}{A_T}\int_{i-1}^{i}\frac{d(h)}{\sigma(h)}\ ;\ i = 0,,5\ and\ h_i - h_{i-1} = 1km \tag{4.9}$$

where R_A is the resistance between cloud-top and the ionosphere (20km – 80km), R_T is the resistance of the thunderstorm, and R_B is the resistance between the cloud-based and the ground, respectively. The $\sigma(h)$ is an electric conductivity of the air as shown in Figure 1.6 and A_T is the area of the generator cell.

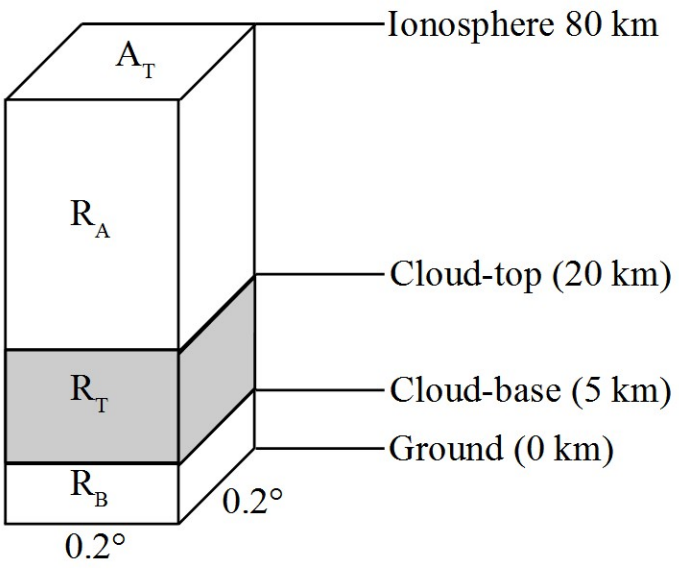

Figure 4.4: Schematic diagram of the three resistors in the generator cell. The accompanying resistance are R_A, R_T, and R_B represent the resistance between cloud-top and the ionosphere, the resistance of the thunderstorm, and the resistance between the cloud-based and the ground, respectively.

As a next step, a cell where does not has lightning events and rainfall was identified to be a fair-weather cell, and these fair weather cells were combined with the average column resistance map (Figure 4.5) and the effect of galactic cosmic rays (Velinov et al., 2013) for calculating the global fair weather resistance (R_{FW}). by:

$$R_{FW} = \frac{1}{\sum_{i=0}^{i=1800} \sum_{j=0}^{j=900} \gamma A_{i,j} R_{i,j}} \tag{4.10}$$

where $A_{i,j}$ is an area of a $0.2^\circ \times 0.2^\circ$ cell and $R_{i,j}$ is an average column resistance of cell i, j as shown in Figure 4.5. The parameter γ is a fraction from the yearly mean value of the galactic cosmic rays.

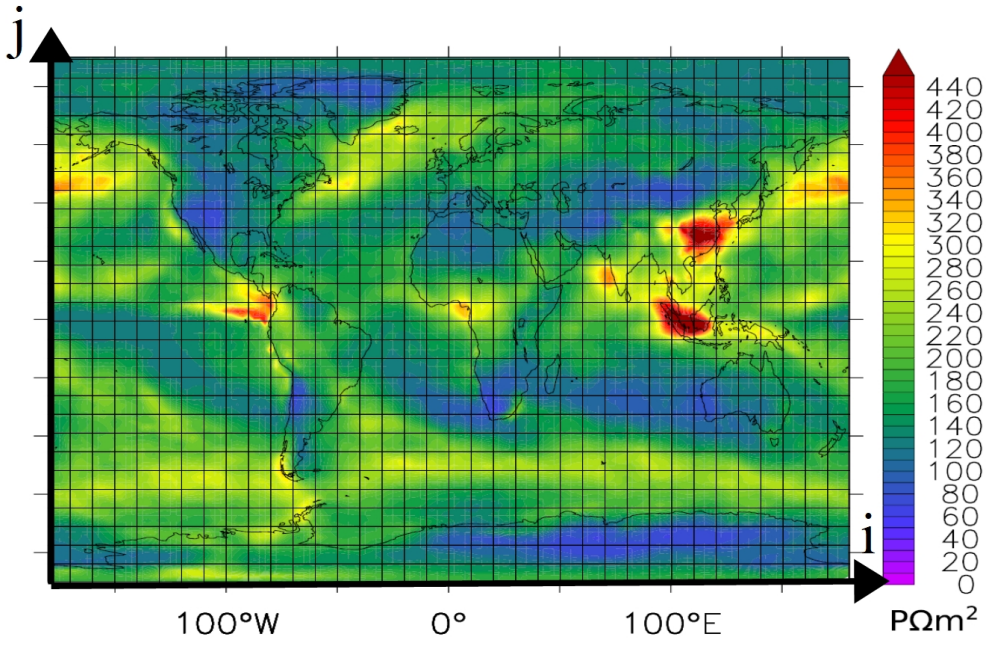

Figure 4.5: Average column resistance map that was used for calculating the fair-weather resistance (Baumgaertner et al., 2013).

The capacitance in the global electric circuit was also calculated using standard electrostatic theory (Rycroft et al., 2007) as

$$C_{T_i} = \frac{\varepsilon_0 A_T}{h_i - h_{i-1}}, i = 0, ..., 80, h_i - h_{i-1} = 1km \tag{4.11}$$

where ε_0 is the dielectric permeability of free space, $h_0 = 0$ km is the mean ground level, and $h_{80} = 80$ km is the height of the ionosphere.

In a final step, the tree inputs parameters that are the upward electric current produced by lightning discharges (I_L), the upward electric current produced by rainfall (I_P), and the fair weather resistance (R_{FW}) were used in our 3-dimensional model (Figure 4.6), which was newly developed. In Figure 4.6, a cell where has lightning and/or precipitation was identified as a generator cell, and it was used for calculating the upward current to the ionosphere. While a cell where does not has lightning and precipitation was identified as a fair-weather cell, and it was used for calculating the fair-weather resistance. Then the output parameter,*i.e.*,

the fair weather electric field was estimated. As a final step, the estimated fair weather electric field was compared with the observation fair weather electric field at Syowa station, Antarctica, Reading station, United Kingdom, and Kakioka, Japan.

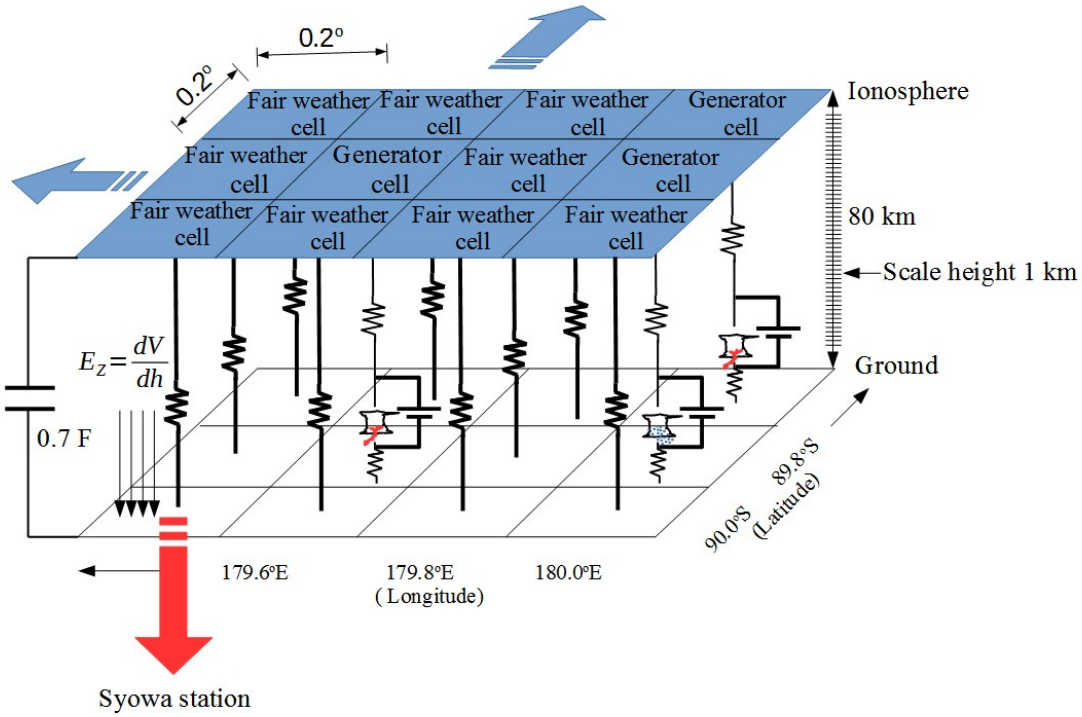

Figure 4.6: The 3-dimensional model that was used to estimated the fair-weather field.

Chapter 5

Contribution of lightning and rainfall to the global electric circuit

5.1 Calculation of the fair weather electric field on May 17, 2013

This section presents the contribution of lightning and rainfall to the global electric circuit. The result on May 17, 2013, was selected as a case study because the weather condition at both Syowa station, Antarctica, and Kakioka station, Japan, are the fair weather, ***i.e.***, no cloud, no rainfall, and the wind speed less than 6m/s.

Figure 5.1(a) presents the total lightning discharges over the globe on March 16, 2014. The blue, red, green, red, yellow, and pink lines represent the occurrence of lightning numbers over Southeast Asia, Africa, South America, North America, and the other areas, respectively, while the black line represents total lightning discharges. It was found that the average of lightning discharges on May 17, 2013, is 49 events per second, and the IC:+CG:-CG ration is 38:0.7:10.

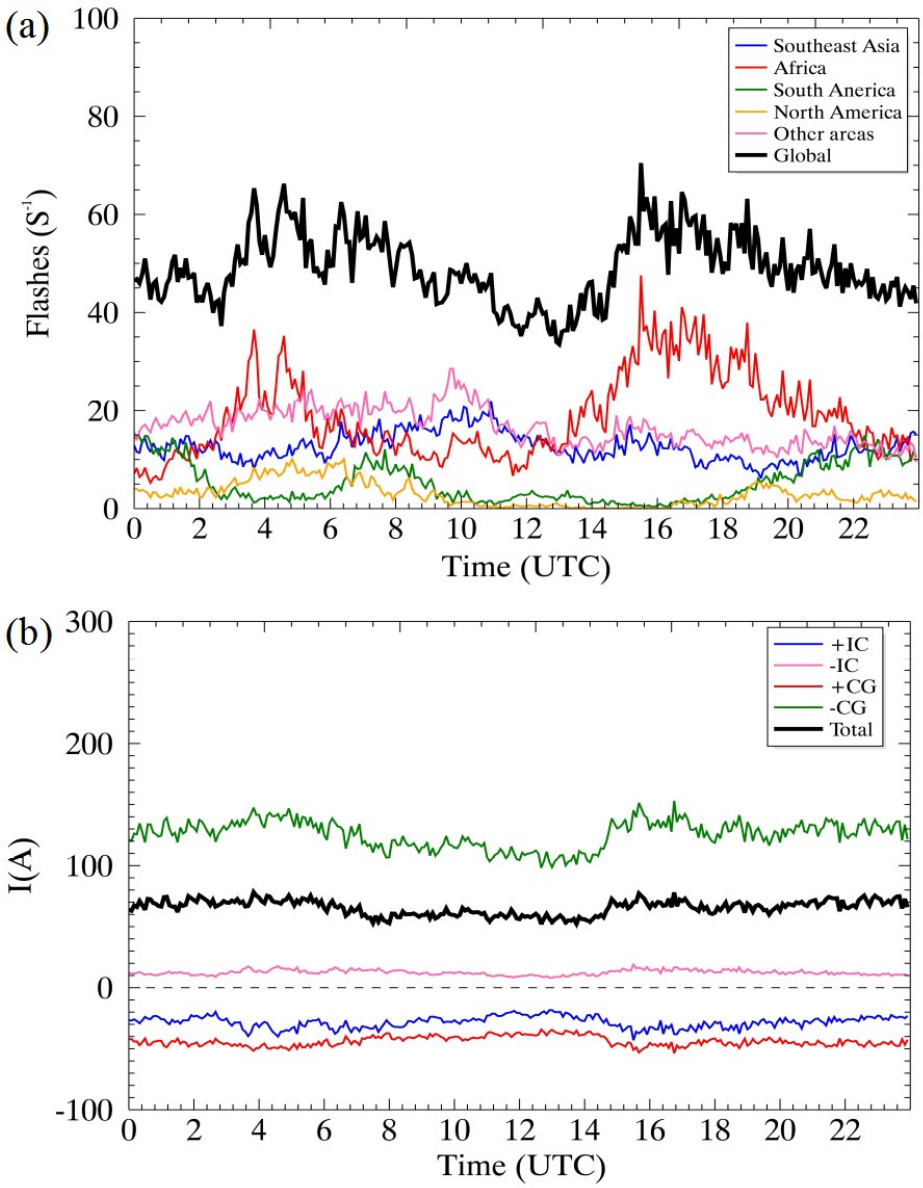

Figure 5.1: (a) Occurrence number of lightning around the world on March 16, 2014. (b) Electric current generated by +IC(blue), -IC(purple), +CG(red), and -CG(green) lightning.

The electric current produced by lightning discharges was also calculated and it is shown in Figure 5.1(b). The blue, pink, red, and green lines represent the electric current generated by +IC, -IC, +CG, and -CG discharges respectively. The total upward electric current to the ionosphere is represented by the black line in Figure 5.1(b). The calculation revealed that the average lightning current in the global electric circuit on May 17, 2013, was 40.7 A with the standard deviation 5.99 A.

Figure 5.2 shows the diurnal variation of the rainfall over continental(red line), oceanic areas(blue line), and the global rainfall (black line). It was found that 25.3% of the global rainfall was rainfall over continental areas and the remaining (74.7%) was the rainfall over the oceanic areas. The possible explanation for this result is that the oceanic areas are larger than continental areas, especially over the tropical area (20°S – 20°N) where is the main source of rainfall. Therefore, rainfall over oceanic areas was higher than that of continental areas. An upward electric current generated by global rainfall on May 17, 2013, was also calculated and it is shown in Figure 5.2(b). The electric current in Figure 5.2(b) was calculated from the global rainfall in 5.2(a). It was found that the average upward electric current to the ionosphere generated by global rainfall was 744.2 A. As shown in 5.2(b), it was clear that almost upward electric current was generated by the rainfall over the oceanic area (74.7%).

Figure 5.3 shows the fair weather resistance that was calculated from the rainfall data provided by the GPM, the lightning data provided by the WWLLN, and the average column resistance map (Figure 4.5). The average of fair weather resistance on May 17, 2013, is 228.3 Ohm, and this number has a good agreement with the fear weather resistance 220-240 Ω that introduced by Rycroft et al. (2007); Rycroft and Odzimek (2010); Baumgaertner et al. (2013).

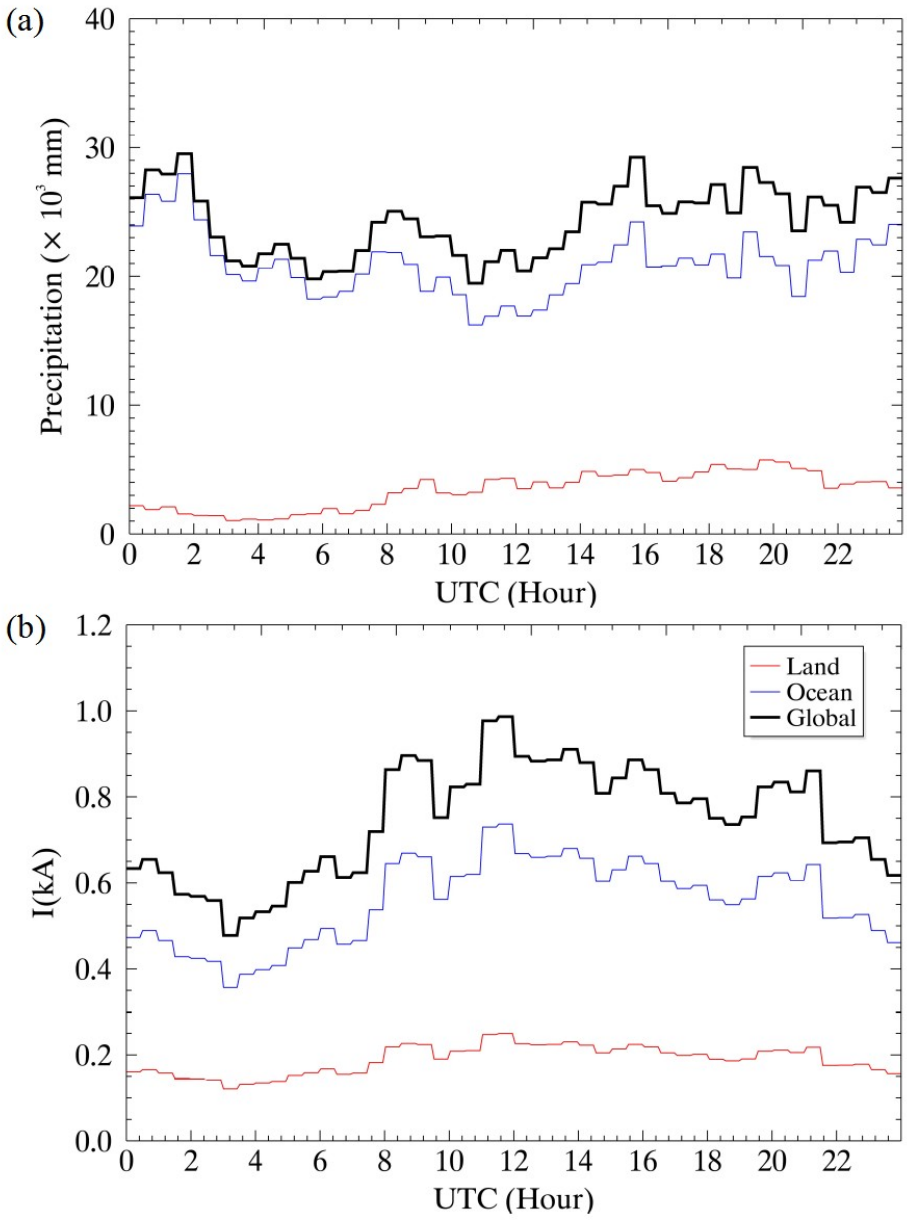

Figure 5.2: (a) Rainfall over continental, oceanic, and global which calculated from the GPM on May 17, 2013 (b) Electric current from rainfall which calculated from the precipitation data in Figure 5.2(a).

Using input parameters in Figure 5.1, 5.2, and 5.3, the fair weather electric field (E_{ZE}) near the ground on May 17, 2013, was also calculated. Then it was compared with the observation fair weather electric fields (E_{ZO}) at Syowa station, Antarctica (Figure 5.4(a)), and Kakioka, Japan (Figure 5.4 (b)). In the Figure 5.4(a), the red, blue, and green line shows E_{ZO} measured by the filed-mill sensors number 1, 2, and 3 respectively. Each dot in Figure 5.4 presents the average of E_{ZE} every 5 minutes.

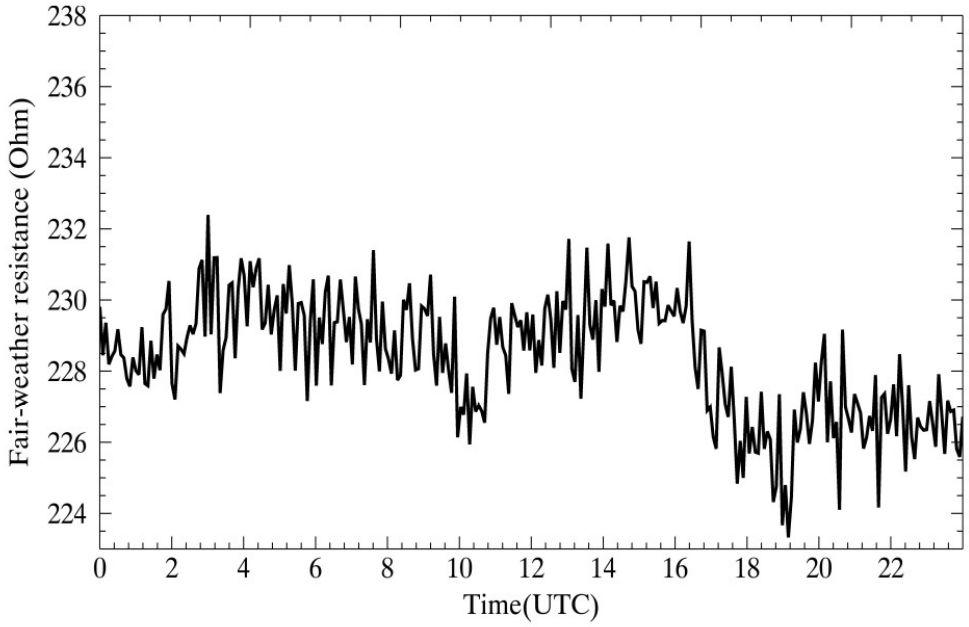

Figure 5.3: Fair weather resistance on May 17, 2013, calculated from the average column resistance.

The estimated E_{ZE} has a good agreement with the observed E_{ZO} at both Syowa station and Kakioka station. The correlation coefficient between E_{ZE} and E_{ZO} at Syowa station and Reading station are 0.322 and 0.326.

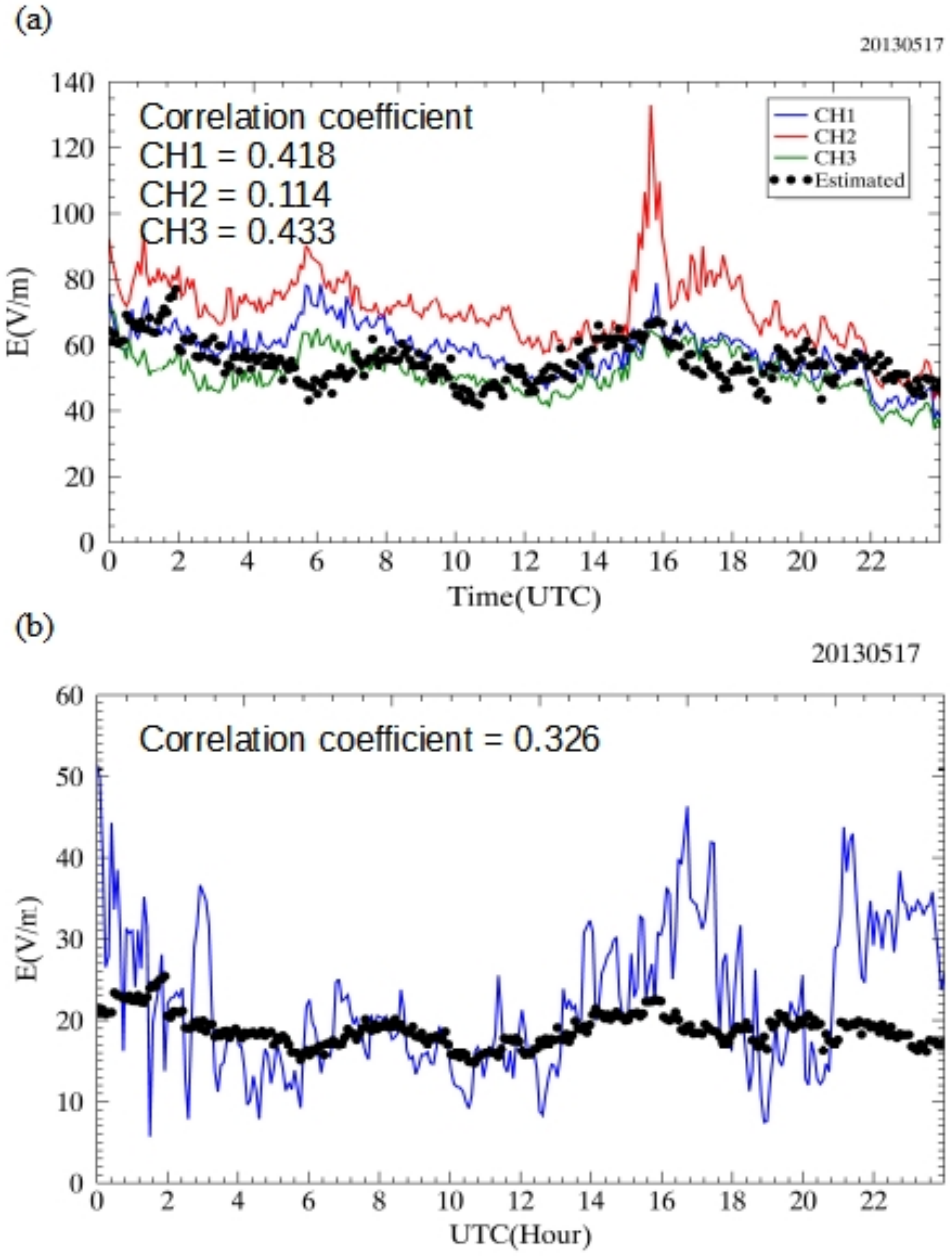

Figure 5.4: (a)Comparison between the estimated fair-weather electric field and the observed fair-weather electric field at the Syowa station on May 17, 2013. (b) similar to (a) but for at the Kakioka station.

The fair weather current density was also calculated. It is found that an average current density was 1.7 pA/m^2, and it smaller than an average fair weather current density 2-3 pA/m^2 introduced by Wilson (1921). It can be concluded that the contribution of the lightning discharges to the global electric circuit on May 17, 2015, is 40.7 A (5.2%) while the contribution of the rainfall in the global electric circuit is 744.2 A (94.8%).

5.2 Calculation of the fair weather electric field on March 16, 2014

This section presents another case study on the contribution of lightning and rainfall to the global electric circuit on March 16, 2014. The result on this day was selected as a case study because the weather condition at both Syowa station, Antarctica, and Reading station, UK, are the fair weather, *i.e.*, no cloud, no rainfall, and the wind speed less than 6m/s.

Figure 5.5(a) presents the total lightning discharges over the globe on March 16, 2014. The blue, red, green, yellow, and pink lines represent the occurrence of lightning numbers over Southeast Asia, Africa, South America, North America, and Oceanic areas, respectively, while the black line represents total lightning discharges. It was found that the average of lightning discharges on March 16, 2014, is 57 events per second, and the IC:+CG:-CG ration is 43:0.9:13.

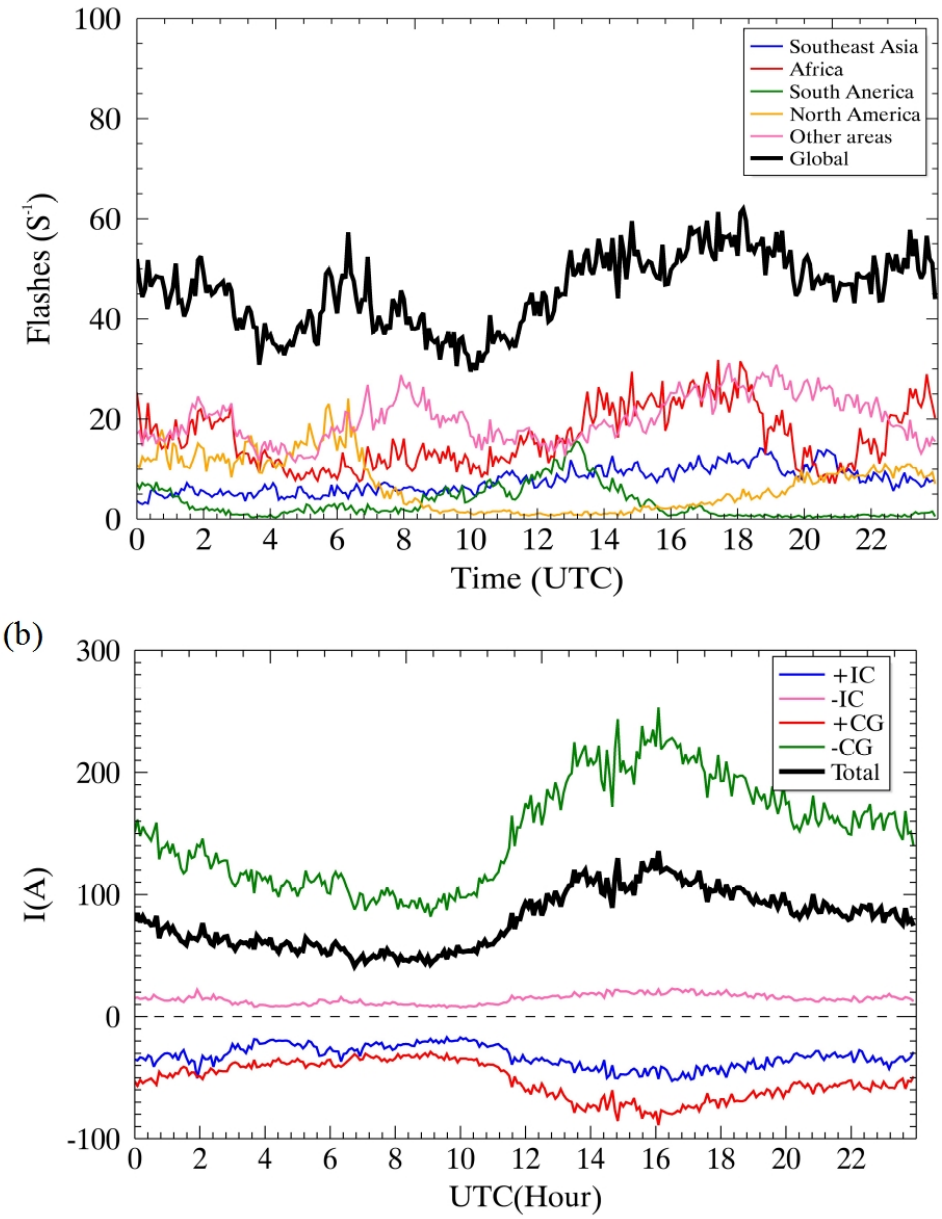

Figure 5.5: (a) The number of +IC(blue), -IC(purple), +CG(red), and -CG(green) lightning around the world on March 16, 2014. (b) Electric current generated by +IC(blue), -IC(purple), +CG(red), and -CG(green) lightning.

The electric current produced by lightning discharges was also calculated and it is shown in Figure 5.5(b). The blue, pink, red, and green lines represent the electric current generated by +IC, -IC, +CG, and -CG discharges respectively. The total upward electric current to the ionosphere is represented by the black line in Figure 5.5(b). The calculation revealed that the average lightning current in the global electric circuit on March 16, 2014, was 79.1 A with the standard deviation 23.6 A. The correlation between lighting current and UT time is interesting because the maximum phase of the lightning current is between 1200 – 1800 UTC when the thunderstorms over Southeast Asia and Africa actives as shown in Figure 5.5(a).

Figure 5.6 shows the diurnal variation of the rainfall over continental(red line), oceanic areas(blue line), and the global rainfall (black line). It was found that 18.8% of the global rainfall was the rainfall over continental areas and the remaining (81.2%) was the rainfall over the oceanic areas. The possible explanation for this result is that the oceanic areas are larger than continental areas, especially over the tropical area (20°S – 20°N) where is the main source of rainfall. Therefore, the rainfall over oceanic areas was higher than that of continental areas. The upward electric current from rainfall was also calculated and it was shown in Figure 5.6(b). The electric current was calculated from the rainfall in 5.6(a). It was found that the average rainfall current was 1118.2 A. As shown in 5.6(b), it was clear that almost rainfall current was generated by the rainfall over the oceanic area (90.9%). The minimum and maximum electric current produced by rainfall were around 0800 UTC and 1900 UTC, respectively. The maximum rainfall current around 1900 UTC was enhanced by the thunderstorms and electrified rain over South America which actives between 1800 UTC – 2200 UTC (Liu et al., 2010).

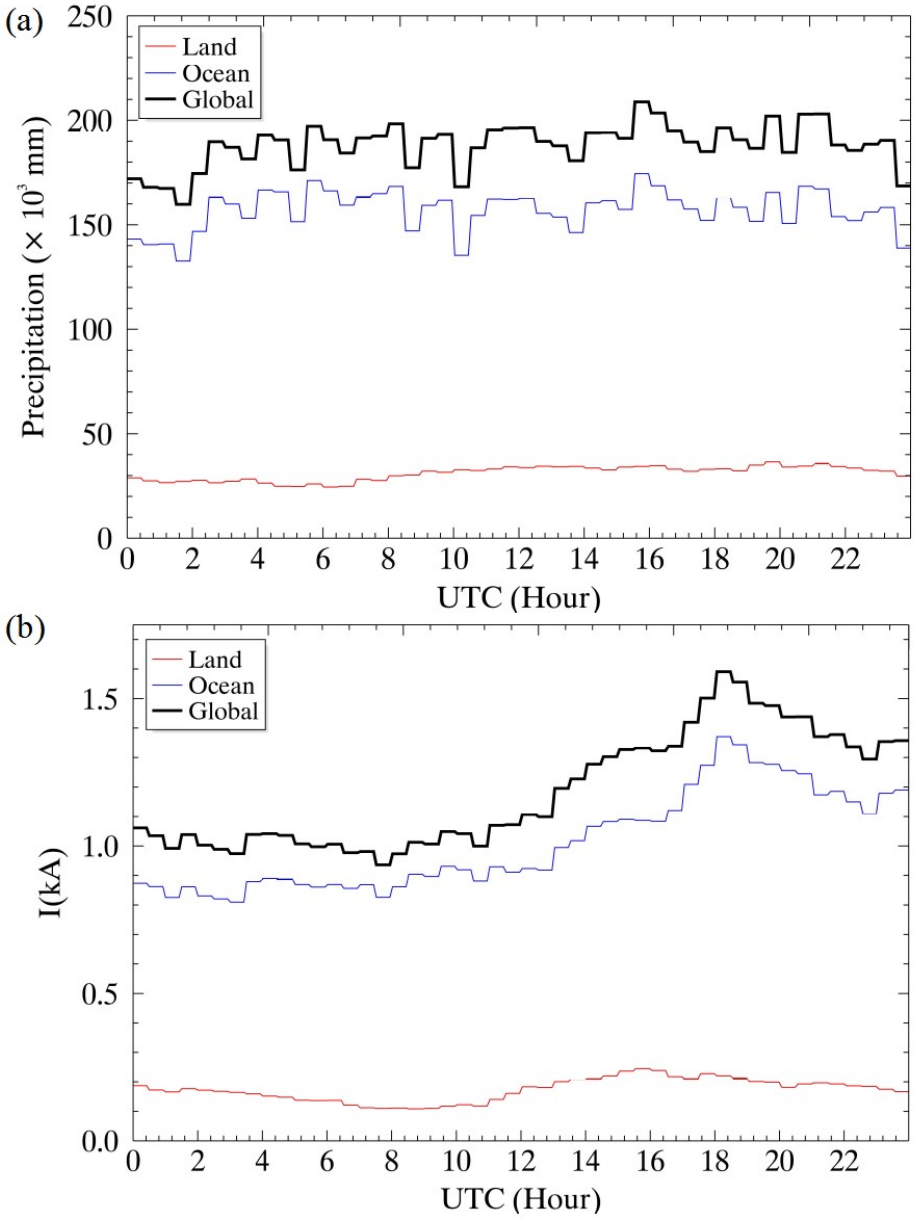

Figure 5.6: (a) Rainfall over land, ocean, and global which calculated from the GPM on March 16, 2014 (b) Electric current from rainfall which calculated from the precipitation data in Figure 5.6(a).

Figure 5.7 shows the fair weather resistance that was calculated from the rainfall data provided by the GPM, the lightning data provided by the WWLLN, and the average column resistance map (Figure 4.5). The average of fair weather resistance on March 16, 2014, is 238.4 Ω, and this number matches with the fear weather resistance 220-240 Ω that introduced by Rycroft et al. (2007); Rycroft and Odzimek (2010); Baumgaertner et al. (2013).

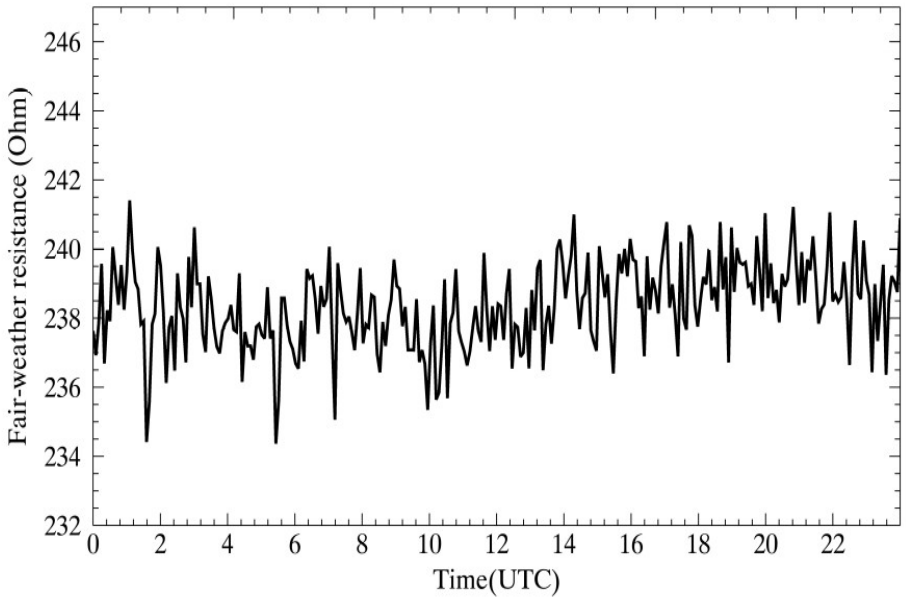

Figure 5.7: (a) Fair weather resistance on March 16, 2014, calculated from the average column resistance.

Using input parameters in Figure 5.5, 5.6, and 5.7, the fair weather electric field (E_{ZE}) near the ground on March 16, 2014, was also calculated. Then it was compared with the observation fair weather electric fields (E_{ZO}) at Syowa station, Antarctica (Figure 5.8(a)), and Reading station, United Kingdom (Figure 5.8 (b)). In the Figure 5.8(a), the red, blue, and green line shows E_{ZO} measured by the filed-mill sensors number 1, 2, and 3 respectively. Each dot in Figure 5.8 presents the average of E_{ZE} every 5 minutes.

The estimated E_{ZE} has a good agreement with the observed E_{ZO} at both Syowa

station and Reading station. The correlation coefficient between E_{ZE} and E_{ZO} at Syowa station and Reading station are 0.373 and 0.455. However, it was found that many spikes were appeared on the observed fair weather electric field at Syowa station. These spikes are originated from the high speed wind at the Syowa station (Minamoto and Kadokura, 2011). When the wind speed is high ($\geq$ 6 m/s), the particles of snow are raised by the wind and charged by frictional electricity. Then, these charged snow particles disturb the atmospheric electric field. The fair weather current density was also calculated. It is found that an average current density was 2.5 pA/m^2, and it has a well agreement with the current density 2-3 pA/m^2 introduced by Wilson (1921). It can be concluded that the contribution of the lightning discharges to the global electric circuit on March 16, 2014, is 79.1 A (6.6%) while the contribution of the rainfall in the global electric circuit is 1118.2 A (9.34%). This upward electric current maintain the potential 285.4 kV between the Earth's surface and the ionosphere.

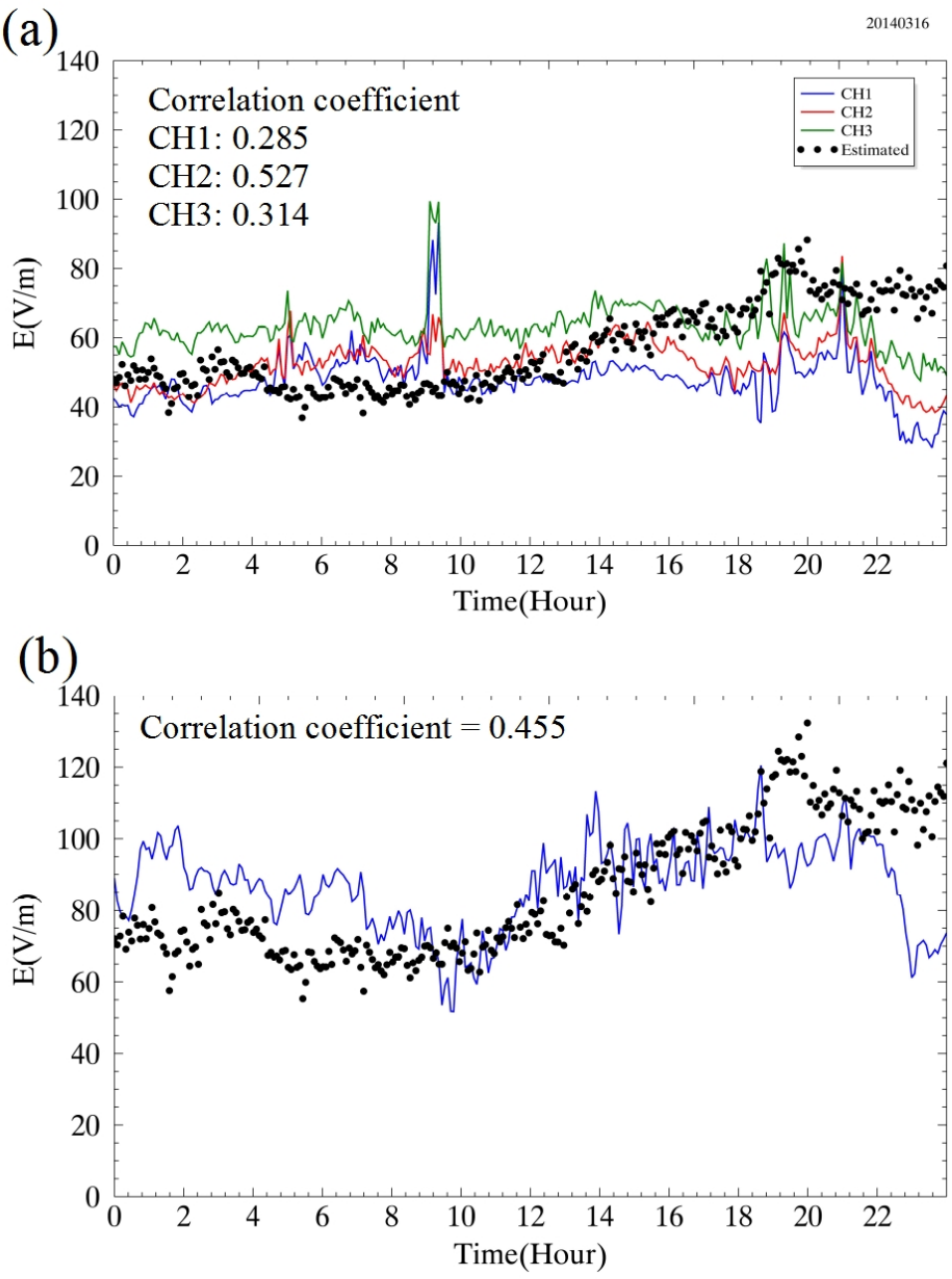

Figure 5.8: Comparison between the estimated fair-weather electric field and the observed fair-weather electric field at the Syowa station on March 16, 2014.

5.3 Contribution of lightning to the global electric circuit

In order to evaluate the upward current to the ionosphere by lightning discharges, the CG lightning data provided by WWLLN and the Z-ratio map were combined to estimate the occurrence number of both IC and CG flashes. Then the total lightning current from lightning around the world was estimated from the average peak current and the average of the decay time of lightning discharges. Figure 5.9(a) and (b) show the average diurnal variation of lightning flashes and the upward current from lightning discharges from 26 fair weather days as shown in Table 5.1.

The average lightning flashes was $\mathbf{54 \pm 6}$ per second, whereas, from the space-based Optical Transient Detector (OTD) instrument, Christian et al. (2003) estimate that the average of lightning flash rate was $\mathbf{44 \pm 5}$ per second. The ratio between IC discharges, +CG discharges, and -CG discharges was also calculated, and it was found that the ratio between IC:+CG:-CG discharges is 42:0.81:12, while, Rakov et al. (2004) introduce that the approximately 10 -CG discharges per second, 0.7 +CG discharges per second, and the remaining 33 discharges per second are IC discharge. Although the occurrence number of +CG and -CG lightning in this study has a good agreement with those mentioned in the previous studies, the occurrence number of IC lightning in this study seems to be higher compared with the previous studies. A reasonable explanation for this might be the difficulty in detecting IC discharges, which is hard to detect especially for the weak IC discharges, in the previous mission.

Table 5.1: Selected date for estimating the fair weather electric field.

Syowa station	Kakioka station	Reading station
1. May 5, 2013	1. January 1, 2013	1. March 16, 2014
2. March 16, 2014	2. May 17, 2013	2. September 3, 2014
3. May 29, 2014	3. April 1, 2014	3. December 28, 2014
4. June 4, 2014	4. June 1, 2014	4. February 8, 2015
5. July 14, 2014	5. October 28, 20	5. March 7, 2015
6. July 29, 2014	6. December 13, 2014	6. April 7, 2015
7. September 15, 2014		7. April 9, 2015
8. October 10, 2014		8. April 14, 2015
9. November 29, 2014		9. April 18, 2015
10. January 6, 2015		10. July 9, 2015

The upward current to the ionosphere from lightning discharges was also calculated, and it is shown in Figure5.9(b). This current was calculated from the occurrence number of lightning discharges in Figure5.9(a). As shown in the figure, the correlation between the total lighting current (black line) and UTC is interesting because the maximum phase of the lightning current is 1800 UTC when the thunderstorms over Africa actives (Roy and Balling, 2013). The average lightning current and standard deviation (STD) were 73.1 A and 17.2 A, respectively. This number has a good agreement with 50-400 A previously estimated by Mareev et al. (2008).

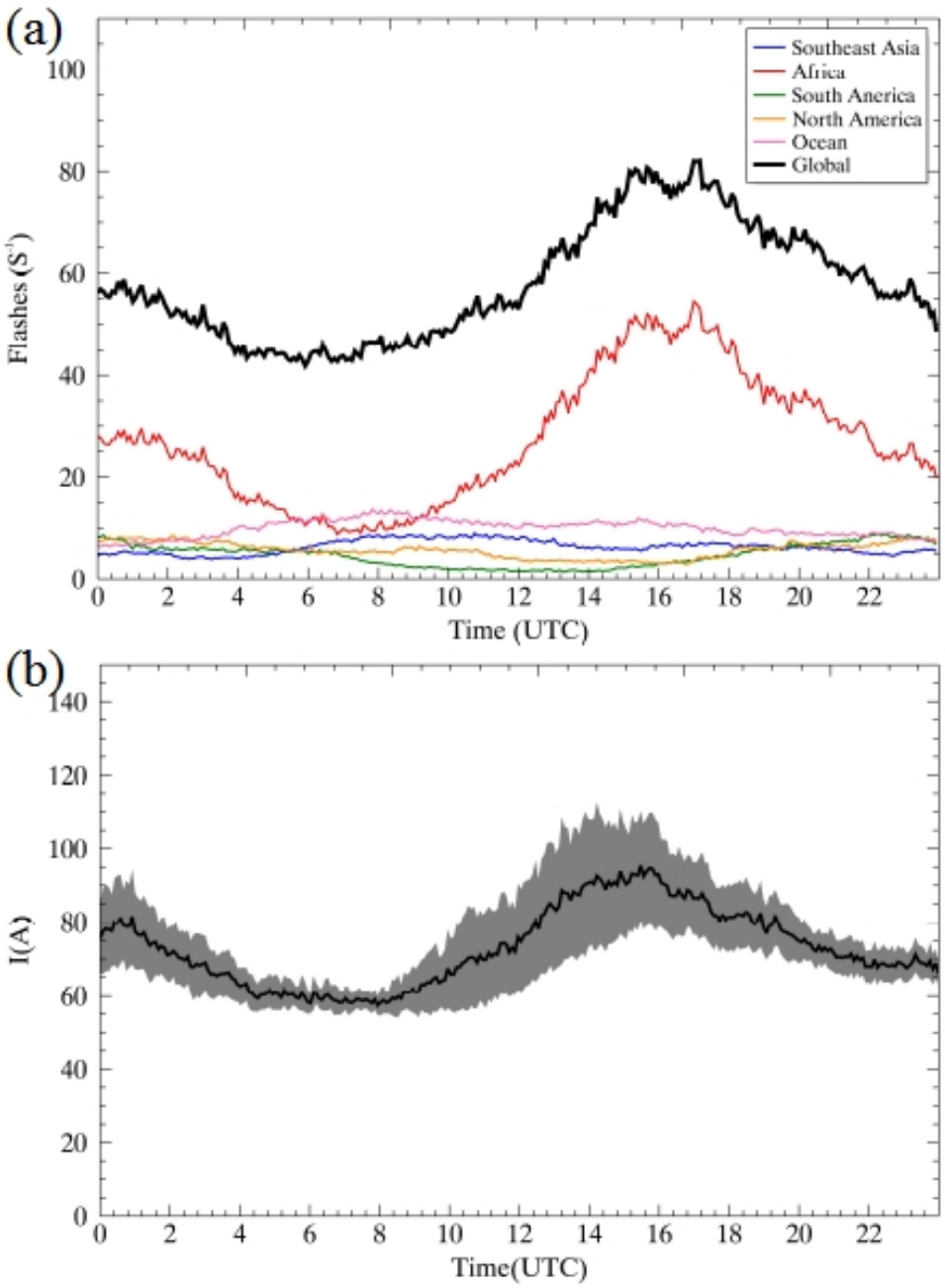

Figure 5.9: (a) Lightning flashes as a function of UTC. (b) The estimated lightning current as a function of UTC. The $\pm 1\sigma$ values are indicated in Gray area.

Although the correlation between lightning current and the Carnegie curve is in good agreement, the amplitude of total lightning flashes from the median is 7.92%. This number is smaller than that of the Carnegie curve (19.7%). This evidence illustrates that lightning ($\sim 70A$) is not the main generator in the global electric circuit.

5.4 Contribution of rainfall to the global electric circuit

Figure 5.10(a) shows the diurnal variation of rainfall in universal time. Although most electrified rain/shower clouds occurred over ocean (81.2%), rainfall over land (18.8%) shows more diurnal variation than the rainfall over the ocean. As shown in Figure5.10(b), the difference between minimum and maximum of the rainfall over ocean and land are 12.2% and 32.4%, respectively.

The upward electric current generated by the rainfall was also calculated, and it is shown in Figure 5.10(c). This upward current was calculated from the rainfall in Figure 5.10(a). The average upward current to the ionosphere by land (red) and ocean (blue) rainfall is 105.1 A and 983.6 A, respectively. Therefore, the upward current was totally 1088.7 A. The correlation between the upward current from rainfall and UTC is very interesting finding. As shown in Figure 5.10(c), the maximum phase of the current is 2000 UTC when the thunderstorms and electrified rain/shower over South America actives. This finding confirms that the main current source in the global electric circuit is the rainfall which contributes around 1080 A (94.4%) to the ionosphere.

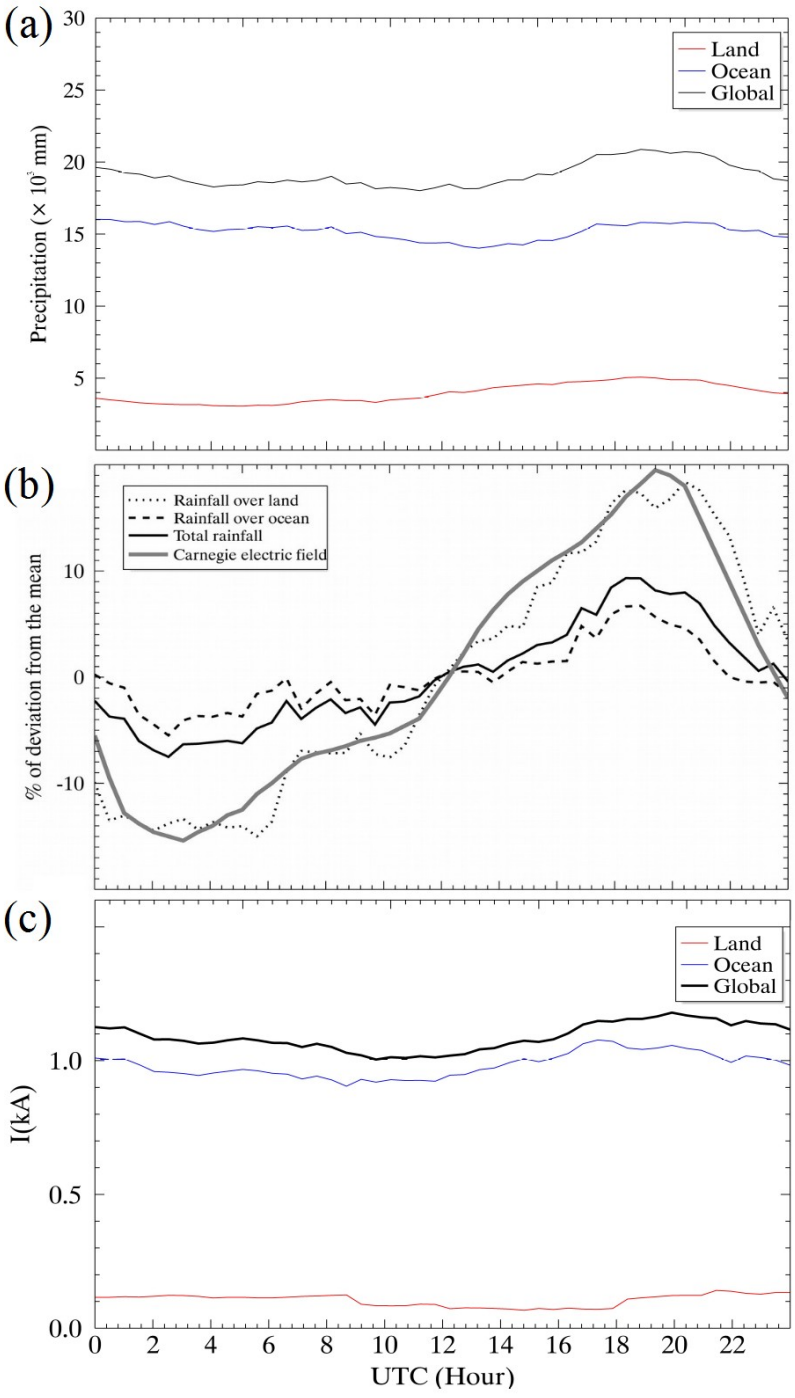

Figure 5.10: (a) The average of global rainfall over continental and oceanic areas. (b) The comparison between the Carnegie curve (gray curve) and the diurnal variations of total rainfall (black solid) over land (dashed) and over ocean (dotted). (c) Upward electric currents generated by global rainfall calculated from Figure 5.10(a).

5.5 Fair-weather resistance

The correlation between the fair weather resistance (R_{FW}) and universal time is presented in Figure 5.11 (black line), and the standard deviation is also shown in the figure (gray area). The result reveal that the diurnal variation of the global resistance links with the precipitation and lightning activities. As shown in Figure 5.11, the maximum R_{FW} is 1900 UTC when the lightning and precipitation reach the maximum phase. Meanwhile the minimum R_{FW} is 0500 UTC when the global lightning and precipitation current is in the minimum phase. The reasonable explanation of the links between the fair weather resistance and the rainfall is an area of the Earth's surface that is covered by thunderclouds. Between 2000 - 2200 UTC, when the rainfall reaches the maximum phase, the Earth's surface is more covered by thunderclouds than those of between 0300 - 0600 UTC. Therefore, the increase of the thunderclouds area decreases the fair weather areas and increases the fair weather resistance between 2000 - 2200 UTC.

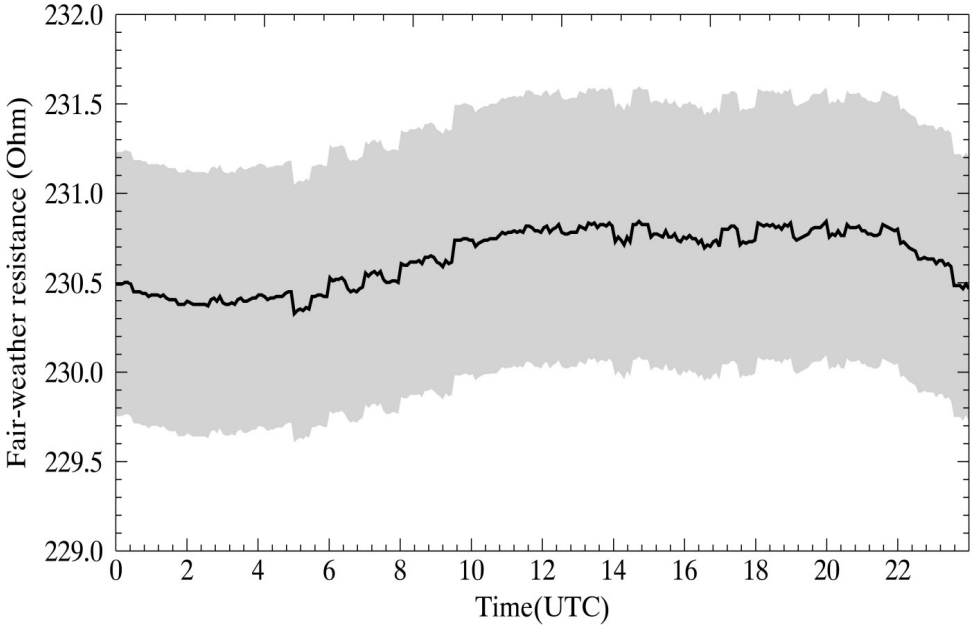

Figure 5.11: Diurnal variations of total global resistance. The black line shows the mean value, and the gray area presents the $\pm 1\sigma$.

The average of the global resistance is 230.7Ω with the standard deviation of 0.75. The fear weather resistance in this study well agrees to the value of those ($220-250\Omega$) which estimated by Rycroft and Odzimek (2010) and Baumgaertner et al. (2013).

5.6 Simulation of a fair-weather electric field

The further analysis was made in order to find the correlation between the estimated fair weather field (E_{ZE}) and the observed fair weather field (E_{ZO}) at the Syowa station. To do this, the three input parameters *i.e.*, lightning current, rainfall current, and fair weather resistance, were used as inputs parameters in the developed 3-dimensional global electric circuit model (Figure 4.6). Figure 5.12(a) – 5.12(f) show the comparison between E_{ZE} and E_{ZO}. The blue, red, and, green line represent the E_{ZO} obtained from sensors numbers 1, 2, and 3, respectively. The black dot shows the E_{ZE} of every five minutes from 0000UTC to 2359 UTC. The correlate coefficient between E_{ZE} and E_{ZO} was also provided in the Figure.

As shown in Figure 5.12, the E_{ZE} estimated from the developed 3D-model is in good agreement with the E_{ZO}. Although the correlation coefficient between E_{ZE} and E_{ZO} was high (the average correlation coefficient for all cases was 0.424), we found many spikes that the developed 3-dimensional global electric circuit cloud not be explained. A satisfactory explanation for this limitation may be that the strong wind at the measurement filed affects the E_{ZO} as introducing by Minamoto and Kadokura (2011).

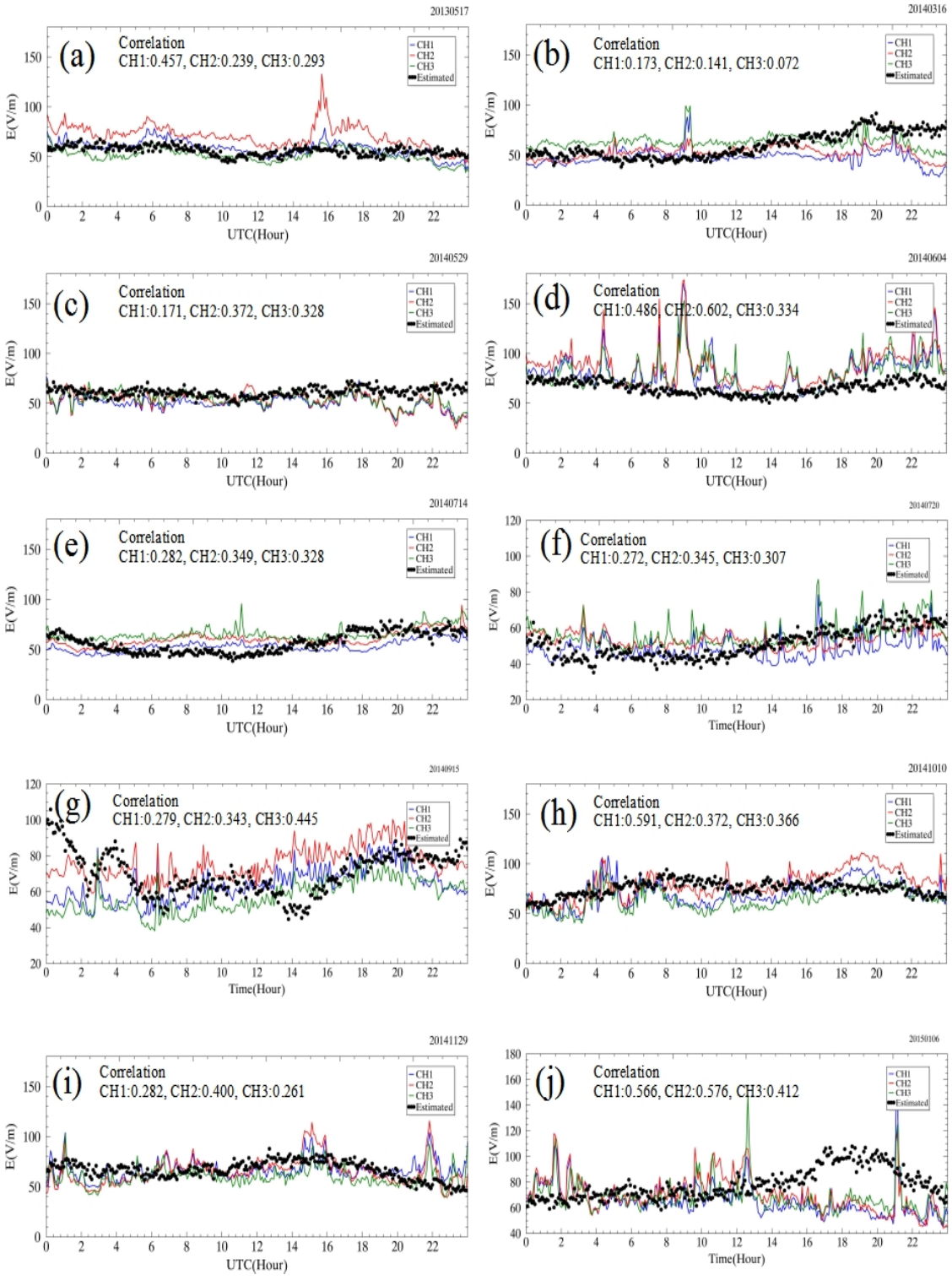

Figure 5.12: Comparison between the estimated fair-weather electric filed (black dot) and observed fair-weather electric filed (red, green, and blue) at the Syowa Station. The red, blue, and green lines in the Figure represents the observed fair-weather electric fields obtain from Sensor 1, 2, and 3 respectively.

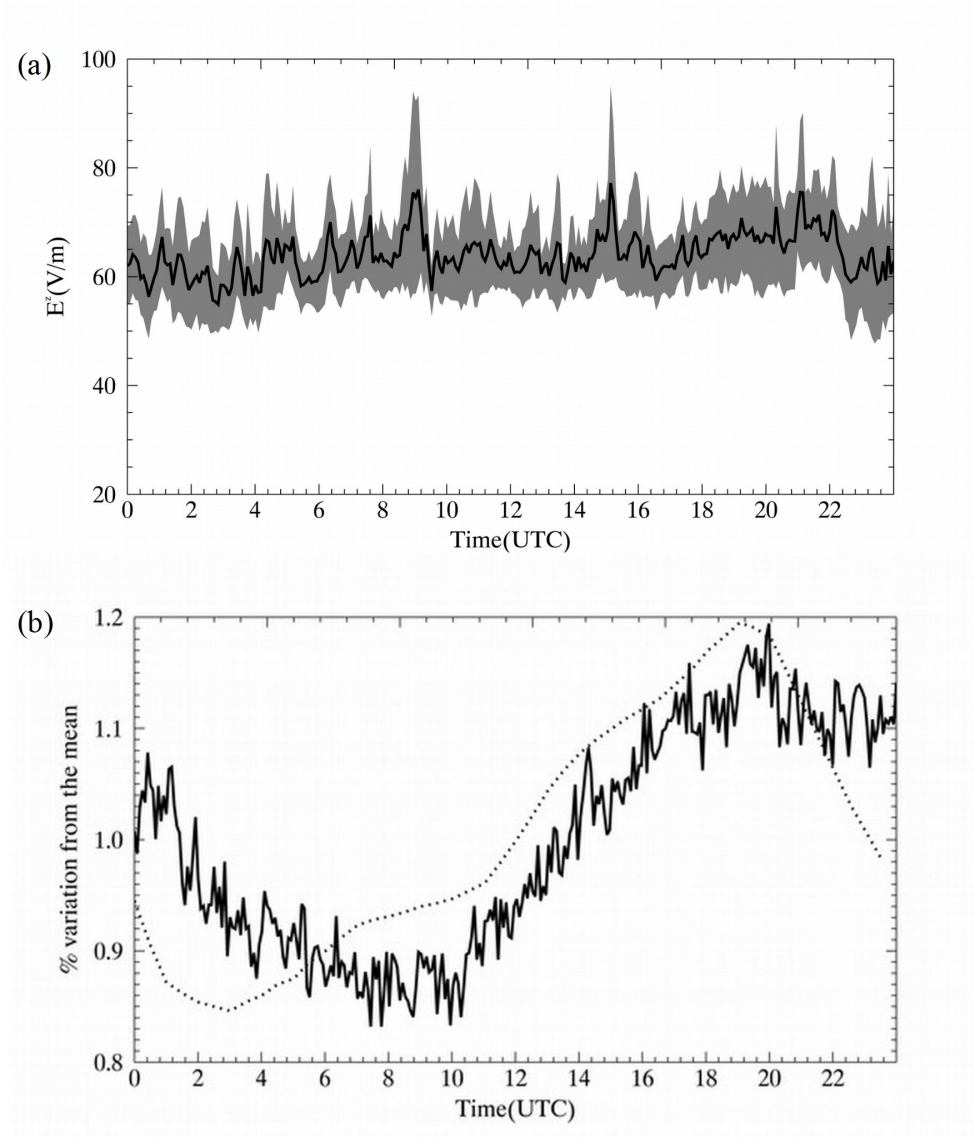

Figure 5.13: Average of the estimated fair weather electric field at Syowa station. The average E_{ZE} in this Figure calculated using the data as shown in Figure 5.12.

Although the percentage of variation from the mean of E_{ZE} (black line in Figure 5.13(b)) well agree with the Carnegie curve (Black dotted line in Figure 5.13(b)), As shown in Figure 5.13(a), the absolute magnitude of E_{ZE} was smaller around 2 times of the global (yearly) average of fair-weather electric fields ($120V/m$) Harrison (2012). However, this is not particularity surprising given a fact that the column resistance at the Syowa station might be smaller than other areas due to the effect of the galactic cosmic rays. Near the geomagnetic north and south pole, the galactic cosmic rays easily penetrate to the Earth's atmosphere. The increasing of GCR ionization at high geomagnetic latitudes more reduces the column resistance than other areas. Consequently, due to Ohm's law, the decreasing of the column resistance would also link to decrease in the fair-weather electric filed if a constant current source is assumed.

Figure 5.14 presents the comparison between the estimated E_{ZE} and the observed E_{OE} at Reading station, located in United Kingdom. It was found that the estimated E_{ZE} has a good agreement with the E_{ZO} the high correlation coefficient (the average correlation coefficient for all cases was 0.497). The average of E_{ZE} was also calculated, and it is shown in Figure 5.14. We found that the average of the fair-weather electric field is 124.4 V/m. This number has a good agreement with the 120 V/m introduced by Wilson (1921); Harrison (2005); Rycroft and Odzimek (2010); Harrison (2012).

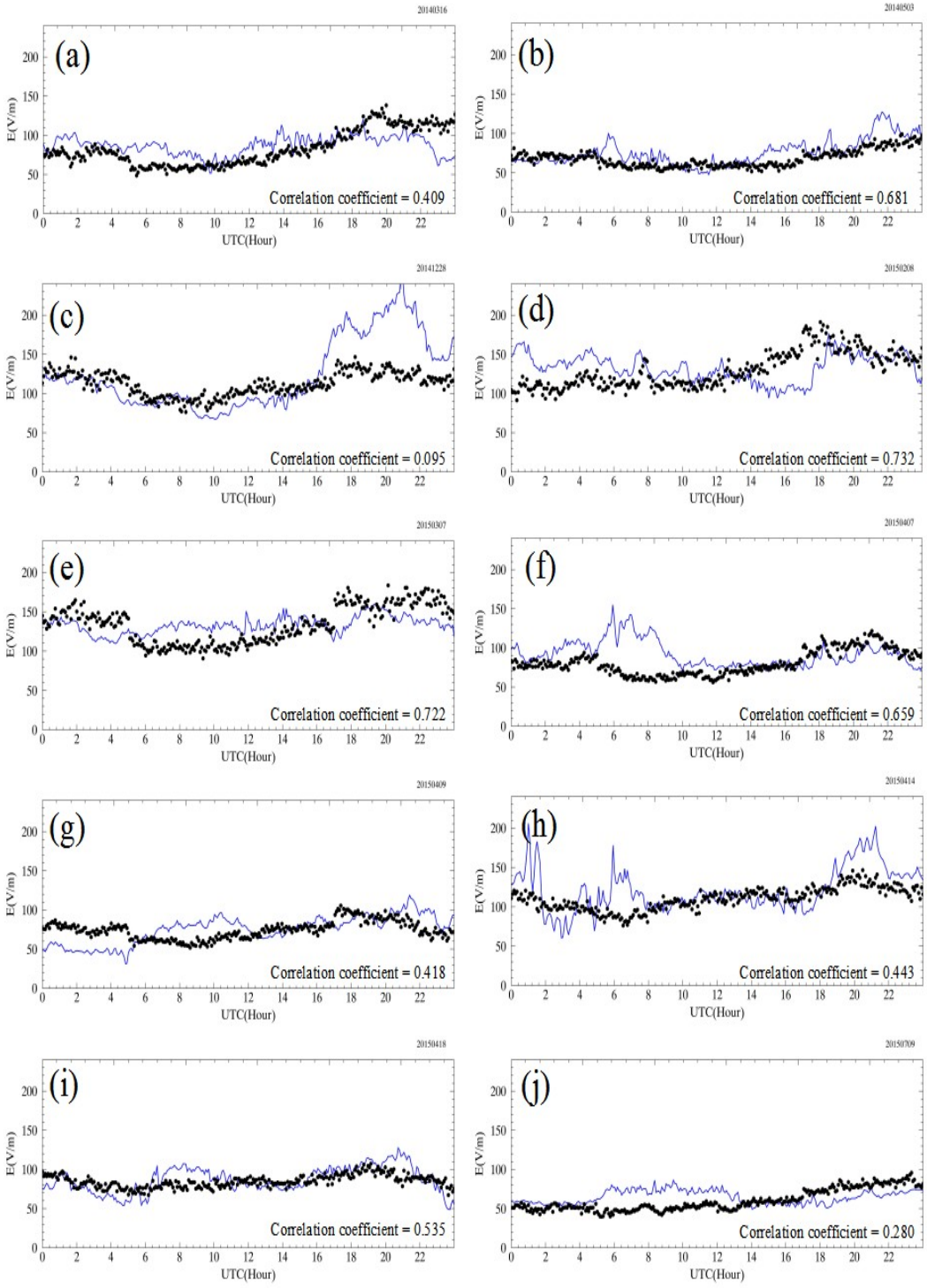

Figure 5.14: Comparison between the estimated fair-weather electric filed (black dot) and observed fair-weather electric filed (blue line) at the Reading Station, located in the United Kingdom.

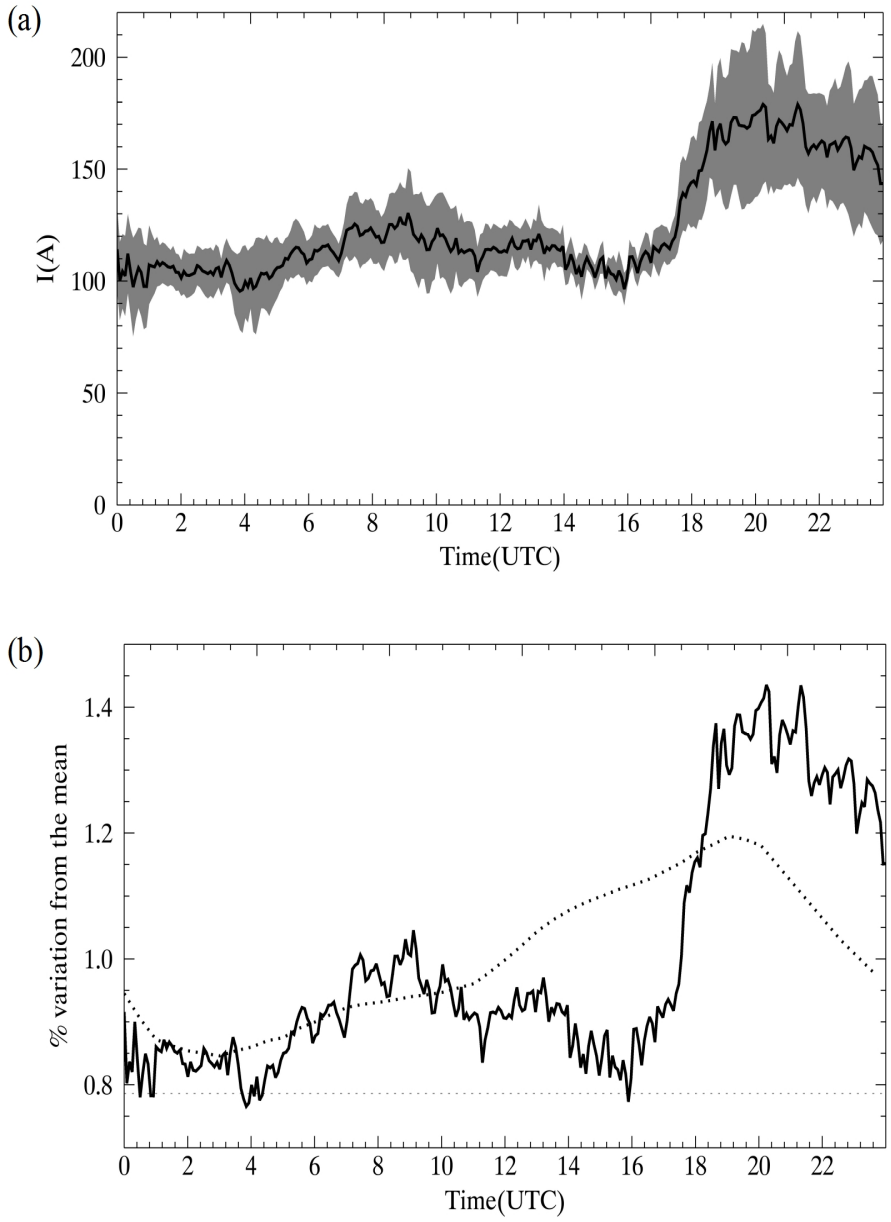

Figure 5.15: Average of the estimated fair weather electric field at Reading station. The average E_{ZE} in this Figure calculated using the data as shown in Figure 5.14.

The fair weather electric field at Kakioka station, Japan, was also calculated and it is shown in Figure 5.16. The black dotted in Figure 5.16 shows the average fair weather electric field every five minutes while blue line presents the observed fair weather electric field. The result reveal that the estimated fair weather electric field has a good agreement with the observed fair weather electric field. The average correlation coefficient for all cases was 0.258.

The average of estimated fair-weather electric field was also calculated, and it is presented in Figure 5.17. The result reveal that the average of the fair-weather electric field is 39.7 V/m with the standard deviation 5.57 V/m . Although the absolute value of both estimated and observed fair-weather electric field at Kakioka station smaller around 4 times of the fair-weather electric field in the previous study Wilson (1921); Harrison (2005); Rycroft and Odzimek (2010); Harrison (2012), the fraction from the mean of the estimated fair-weather electric field at Kakioka station has a good agreement with the Carnegie curve as shown in Figure 5.17

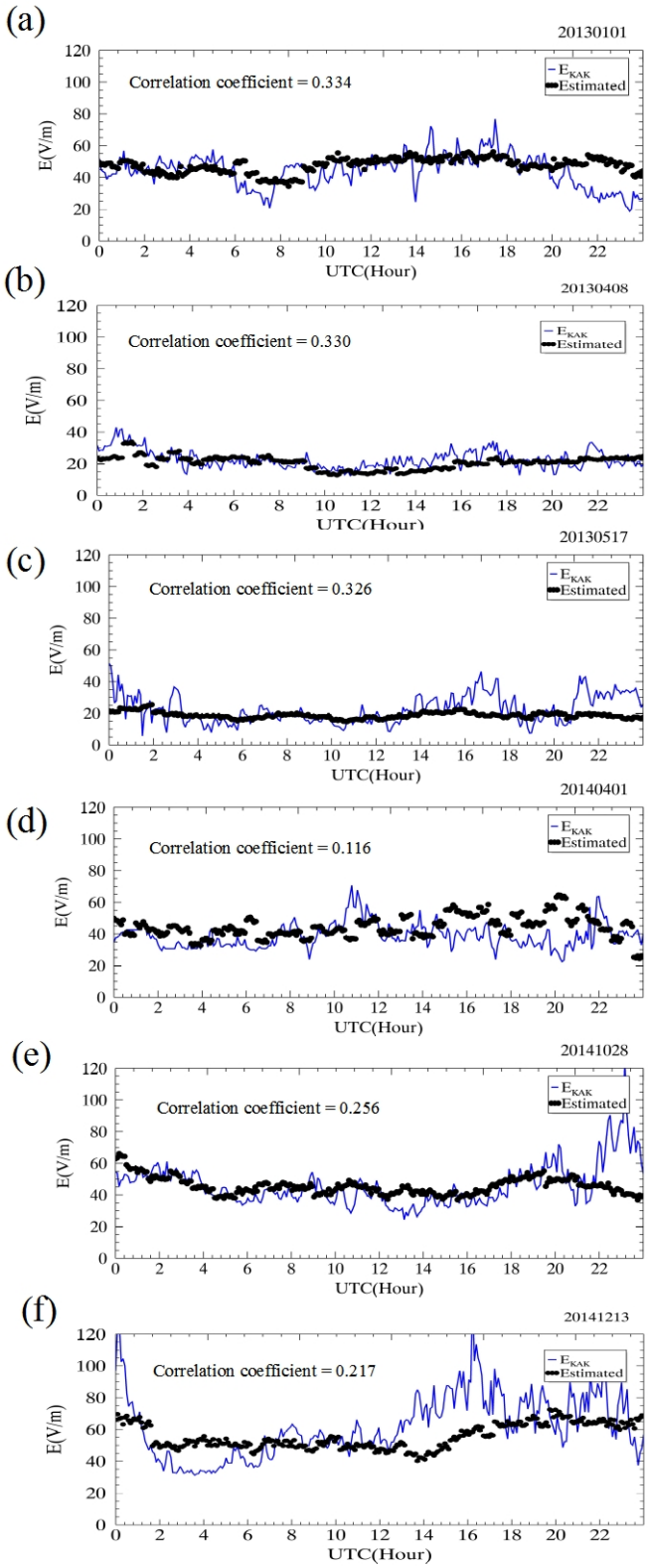

Figure 5.16: Comparison between the estimated fair weather electric filed (black dot) and observed fair weather electric filed (blue line) at the Kakioka Station, Japan.

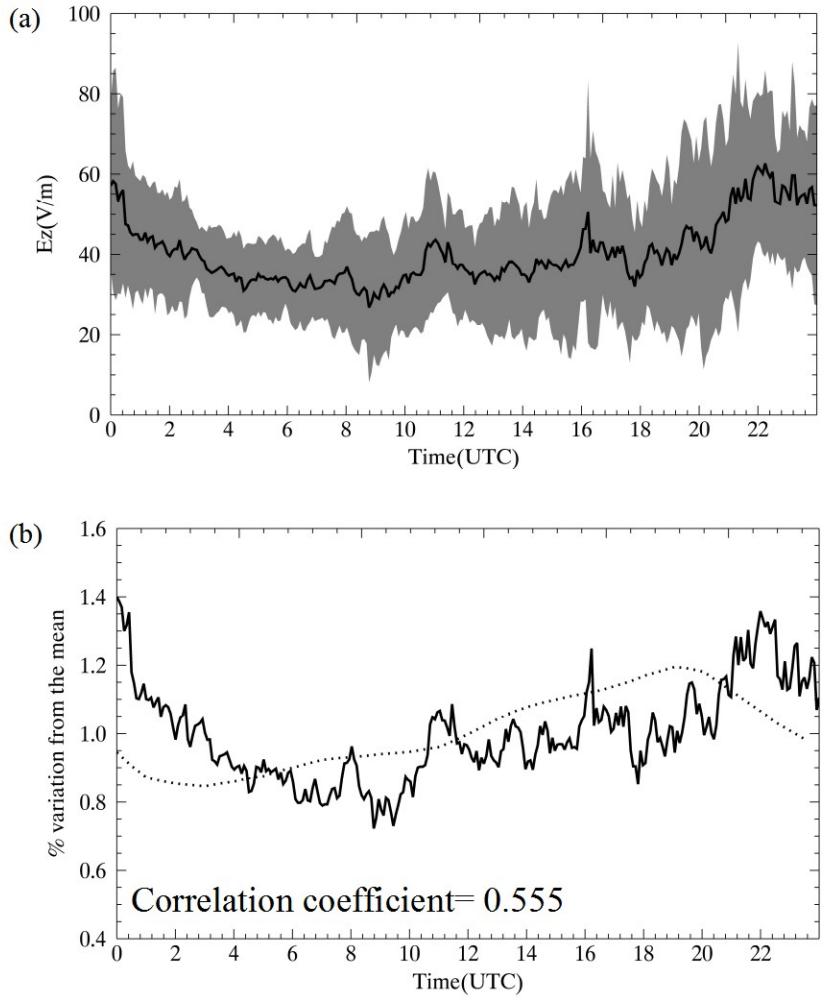

Figure 5.17: Average of the estimated fair weather electric field at Reading station. The average E_{ZE} in this Figure calculated using the data as shown in Figure 5.16.

Chapter 6

Summary

The new method for identifying lightning discharges types was newly developed. The new method used the ratio between blue and red emission provided by JEM-GLIMS space-based mission. It is found that there is a difference in the PH and LSI intensity ratios of IC, +CG, and -CG discahrges. This facts are strongly related to the difference of the atmospheric transmission from the lightning discharges channels to the ISS. However, this method may not be suitable for classifying between -CG discharge and +CG discharge that arise from the lower positive charge region. The discharge channel of this +CG discharge might located at the same altitude of typical -CG discharges. Therefore, the +CG discharge that initiates from the lower positive charge region might be identified as -CG discharge. From these limitations, it would be essential to utilize not only satellite data but also the ground-based lightning data.

Using the new method described above, the occurrence ratio of IC discharges to CG discharges (Z-ratio) was estimated using the lightning optical data obtained by the JEM-GLIMS mission in the period from November 2012 to August 2015. The results derived from our analysis show that the Z-ratio in the continental thunderclouds is higher than that of the oceanic thunderclouds, especially in the area where the lightning activities are high, i.e., central Africa, south-east Asia, and central America. It is also found that the Z-ratio in the local summer is

higher than that in the local winter in both the northern hemisphere and southern hemisphere. The latitudinal dependence of the Z-ratio is clearly found, which is comparable to the previous studies (Pierce, 1970; Prentice and MacKerras, 1977; Mackerras and Darveniza, 1994; Mackerras et al., 1998). The estimated Z-ratio varies from 2.9 - 0.19 from the tropics (20°S - 20°N) to the mid-latitude (20°S - 40°S and 20°N - 40°N) with the global mean of 1.6. The decrease of the Z-ratio from the tropics to the mid-latitude is confirmed both in the northern and southern hemispheres.

Lightning and rainfall play an important part role in the global electric circuit as a current generator. Therefore, in this paper, we assessed the contribution of lightning and rainfall to the global electric circuit using lightning data provided by WWLLN and rainfall data provided by GPM. The major evidence from this study suggests that global rainfall might be an important current source in the global electric circuit. We found that the ratio between the upward current to the ionosphere generate by rainfall and lightning is 16:1. However, the current study was limited by the limitation of warm rain data from TRMM that provided warm rain between 35° S - 35° N. We assumed that precipitation between 90° S - 35° S and 35° N - 90° N carries the electric charge to the ground. However, we believe that our results may improve knowledge about the current source in the global electric circuit. To further our research we plan to include the effect of thin clouds in our model for the more accuracy of our estimation.

Appendix A

The absolute intensity of LSI image

The Lightning and Sprite Imager (LSI) cameras have been calibrated with a standard light source in the laboratory before JEM-GLIMS was launched. LSI-1 and LSI-2 measure the intensity of a standard light source (raw count) that was installed in a spherical dome as shown in Figure A.1. Then, the raw count data were used as the calibration data for calibrating the LSI cameras.

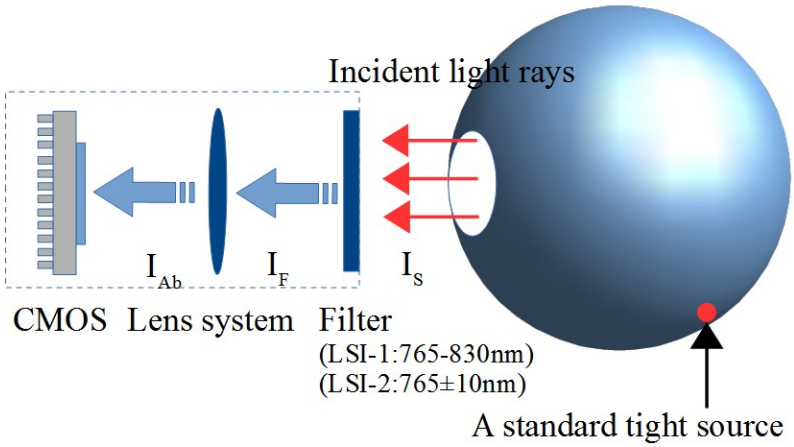

Figure A.1: Schimetic diagram for calibrating the LSI-1 and LSI-2 cameras.

A first step, the specific intensity of a light source ($I_S(\lambda) : W/srm^2nm$), in each wavelengths, were multiplied by the transmission coefficient of the filter (e) to estimate the passed filter specific intensity($I_F(\lambda) : W/srm^2nm$). Then, the passed

filter specific intensity was integral to estimate the absolute intensity (I_A) by:

$$I_A = \int_{\lambda_1}^{\lambda_2} eI_S(\lambda)d\lambda \tag{A.1}$$

Secondly, the correlation between the absolute intensity (I_A) from a standard light source and the relative intensity value (I_R) obtained by LSI-1 and LSI-2 camera was measured and they were presented in Table A.1.

Table A.1: Absolute intensity from a standard light source (I_S) and the relative intensity (I_R) obtained by LSI-1 and LSI-2 camera (Bandholnopparat et al., 2019).

LSI-1		LSI-2	
I_S (W/srm^2nm)	I_R Counts	I_S (W/srm^2nm)	I_R Counts
5.0×10^{-4}	568	5.0×10^{-4}	799
2.0×10^{-4}	245	2.0×10^{-4}	321
1.0×10^{-4}	129	1.0×10^{-4}	170
5.0×10^{-5}	75	5.0×10^{-5}	95
2.0×10^{-5}	41	2.0×10^{-5}	51
1.0×10^{-5}	29	1.0×10^{-5}	31
2.0×10^{-6}	26	2.0×10^{-6}	18

Thirdly, the variation of the absolute intensity(I_A) is plotted toward the relative intensities (I_R), as shown in Figure A.2, in order to find an equation which presents the relationship between the absolute intensity (I_A) and the relative intensity (I_R).

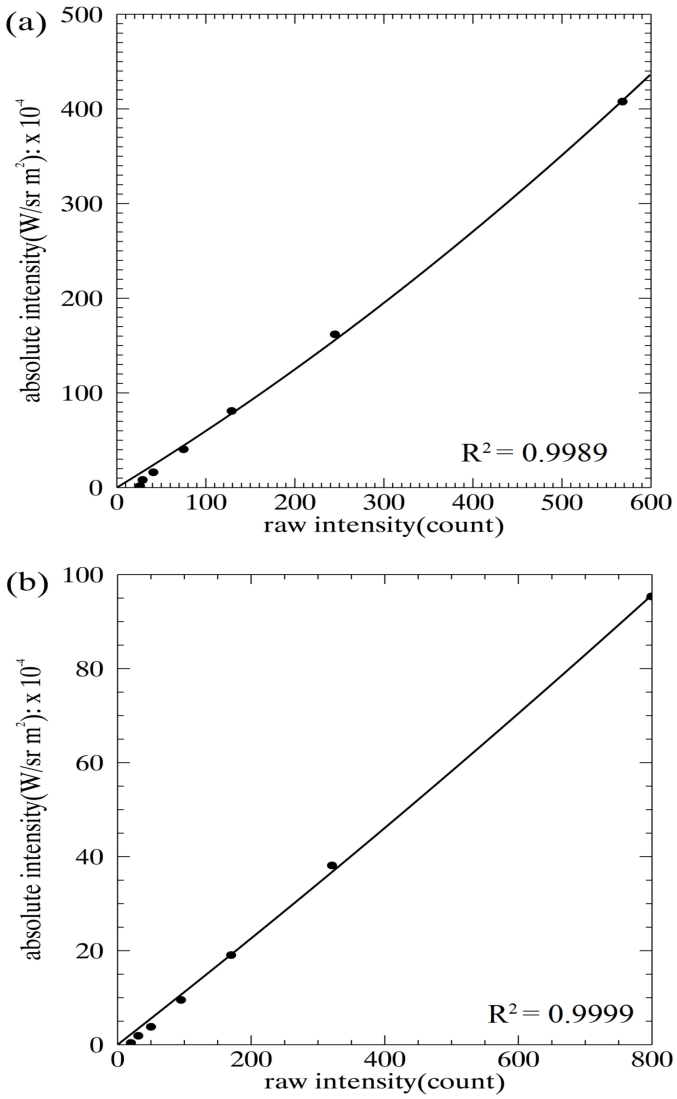

Figure A.2: The variation of the absolute and relative intensities for (a) LSI-1 and (b) LSI-2) Bandholnopparat et al. (2019).

Two functions: (i) the linear function, $f(x) = Ax + B$ and (ii) polynomial function, $f(x) = Ax2 + Bx + C$ were used. The parameters A, B, and C are the parameter to be fitted. It was found that the coefficient of determination (R_2) is 0.99832 (linear) and 0.99897 (polynomial) for LSI-1 and 0.99984 (linear) and 0.99994 (polynomial) for LSI-2, respectively. Consequently, the polynomial function was used for transforming the relative intensity into the absolute intensity for LSI-1 and LSI-2 cameras.

$$I_{A_{LSI-1}} = 2.5937 \times 10^{-8} I_{LSI-1}^2 + 5.7251 \times 10^{-5} I_{LSI-1} \tag{A.2}$$

$$I_{A_{LSI-2}} = 1.0783 \times 10^{-9} I_{LSI-2}^2 + 1.1097 \times 10^{-5} I_{LSI-2} \tag{A.3}$$

Appendix B

Lightning Detection Efficiency of JEM-GLIMS

As we mentioned in Chapter 2, the JEM-GLIMS optical instruments were designed to detect optical emissions of lightning discharges and lightning-associated TLEs. The event triggering threshold of these instruments was set to be high due to the limitation of the telemetry speed between the ISS and the ground, and the average detection number was ∼10 events/day. Therefore, JEM-GLIMS optical instruments detected only intense lightning emissions and missed many weak lightning emissions, that tend to have smaller optical energy. Figure B.1 shows the optical energy distribution of JEM-GLIMS lightning events measured in the period from November 2012 to August 2015. Each data point shows the optical energy in the wavelength range of 400 - 1000 nm which was calculated from PH4(599-900 nm) lightning curve data. The optical energy in the wavelength range of 599 - 900 nm is 29.2% of the optical energy radiated by lightning discharges in the wavelength range of 400 - 1000 nm (Orville and Henderson, 1984). Therefore, we also included this percentage in the calculation of the optical energy in the wavelength range of 400 - 1000 nm for all JEM-GLIMS lightning flashes. It is found that these events have the optical energy larger than 2.1×10^6 J. This means that the JEM-GLIMS optical instruments missed lightning flashes having

the optical energy less than 2.1×10^6.

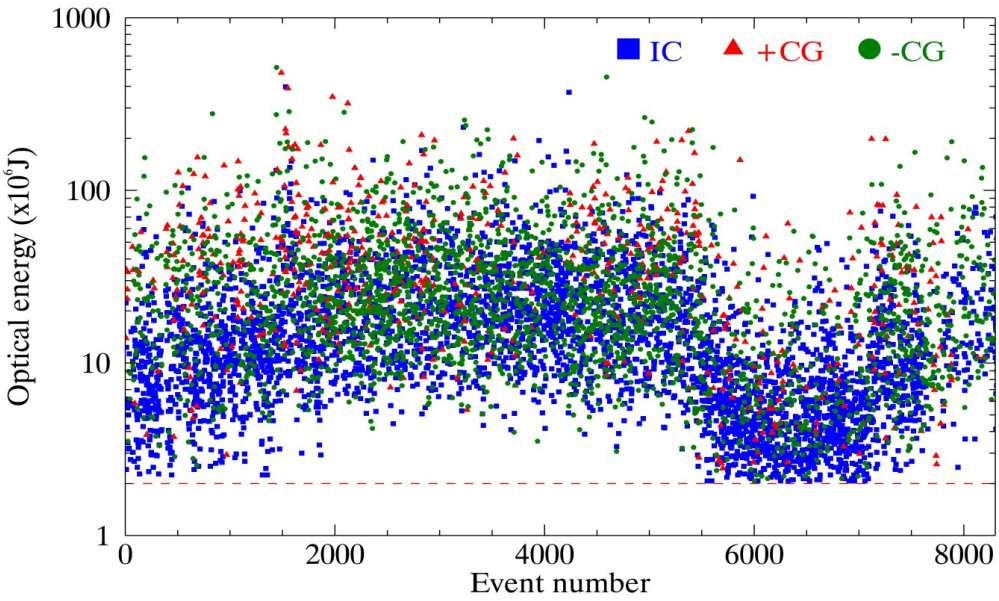

Figure B.1: Optical energy distribution of lightning events detected by JEM-GLIMS optical instruments in the wavelength range of 400 - 1000 nm.

In order to estimate the JEM-GLIMS detection efficiency of lightning emissions, i.e., the ratio between detected lightning events and total lightning events, we first performed further analysis to classify the relation between the optical energy of lightning discharges and the detection number of lightning discharges. Figure B.2 shows the relation between the detection number of lightning discharges by the JEM-GLIMS optical instruments and optical energy. For this plot, the optical energy of each data point was estimated every 0.001 MJ step. Then, we use the linear regression to find the correlation between the occurrence number and the optical energy in the optical energy range from 0.08×10^6 J to 102.0×10^6 J, as shown by the solid and dashed lines in Figure B.2. The reason why we used this optical energy range is that the average optical energy of IC, +CG, and -CG discharges are 1.5×10^6 J, 9.7×10^6 J, and 3.5×10^6 J, respectively, and that these numbers well agree with the optical energies reported by the earlier studies (Orville, 1980; Orville and Henderson, 1984; Quick and Krider, 2013). It was

found that the correlation between the occurrence number of IC, +CG, and -CG discharges, and the occurrence number of lightning discharges can be empirically estimated by the following linear regression functions,

$$N_{IC}(E) = -336.1ln(E) + 1352 \tag{B.1}$$

$$N_{+CG}(E) = -12.21ln(E) + 69.53 \tag{B.2}$$

$$N_{-CG}(E) = -89.15ln(E) + 417.4 \tag{B.3}$$

where $N_{IC}(E)$, $N_{+CG}(E)$, and $N_{-CG}(E)$ are the occurrence number of IC, +CG, and -CG discharges having the optical energy of E, respectively. Then, the total occurrence number of IC, +CG, -CG discharges, i.e., (N_{IC}, N_{+CG}, N_{-CG}), can be estimated by integrating the equations B.1, B.2, and B.3 in the energy range from 0.08×10^6 J to 102.0×10^6 J. Finally, the detection efficiency (DE) is estimated by

$$DE_{IC} = 100 \times \frac{N_{IC_{Glims}}}{N_{IC}} \tag{B.4}$$

$$DE_{+CG} = 100 \times \frac{N_{+CG_{Glims}}}{N_{+CG}} \tag{B.5}$$

$$DE_{-CG} = 100 \times \frac{N_{-CG_{Glims}}}{N_{-CG}} \tag{B.6}$$

where $N_{IC_{Glims}}$, $N_{+CG_{Glims}}$, and $N_{-CG_{Glims}}$ are the number of IC, +CG, and -CG discharges detected by JEM-GLIMS optical instruments. Using this method, the JEM-GLIMS detection efficiency of IC, +CG, and -CG discharges are estimated to be 11.2%, 28.3%, and 19.7%, respectively.

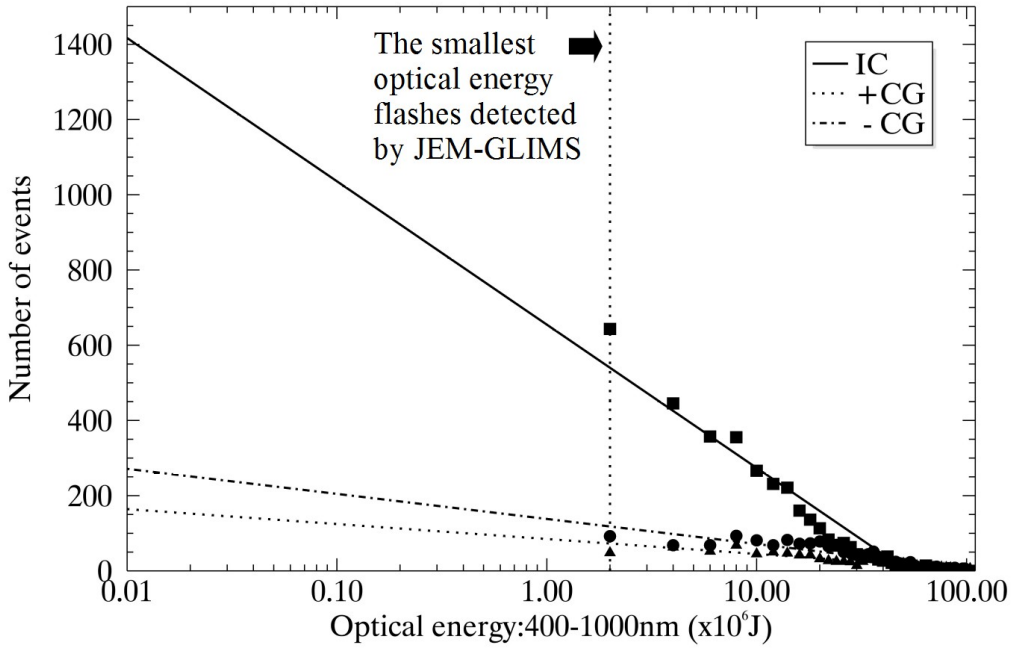

Figure B.2: Optical energy distribution of lightning events detected by JEM-GLIMS optical instruments in the wavelength range of 400 - 1000 nm.

Appendix C

Journal of Atmospheric and Solar-Terrestrial Physics:Optical Properties of Intracloud and Cloud-to-Ground Discharges Derived from JEM-GLIMS Lightning Observations

Journal of Atmospheric and Solar-Terrestrial Physics 189 (2019) 87–97

Contents lists available at ScienceDirect

Journal of Atmospheric and Solar-Terrestrial Physics

journal homepage: www.elsevier.com/locate/jastp

Optical properties of intracloud and cloud-to-ground discharges derived from JEM-GLIMS lightning observations

K. Bandholnopparat[a,*], M. Sato[b], T. Adachi[c], T. Ushio[d], Y. Takahashi[b]

[a] Department of Cosmosciences, Hokkaido University, Sapporo, Japan
[b] Faculty of Science, Hokkaido University, Sapporo, Japan
[c] Meteorological Research Institute, Tsukuba, Japan
[d] Department of Aerospace Engineering, Tokyo Metropolitan University, Hino, Japan

ARTICLE INFO

Keywords:
Intracloud lightning
Cloud-to-ground lightning
JEM-GLIMS
Nadir observation

ABSTRACT

We developed a new method to distinguish the lightning discharge type using lightning data obtained by JEM-GLIMS spaced-based mission and ground-based lightning network that are JLDN, NLDN, WWLLN, and GEON. As a first step, we selected 1057 lightning events detected by the JEM-GLIMS cameras (LSI) and spectrophotometers (PH) in 2014. Then, we compared the JEM-GLIMS optical data to the ground-based lightning data in order to check the simultaneous detection of JEM-GLIMS lightning events by the ground-based lightning networks, and finally we identified the discharge type of the JEM-GLIMS lightning events. We succeed in identifying 941 simultaneous lightning events and found that 582, 93, and 266 lightning events were IC, +CG, and -CG discharges, respectively. As a next step, we calculated intensity ratios between blue and red PH channels, *i.e.,* 337nm/762 nm, 316nm/762 nm, 392nm/762 nm, 337nm/(599–900 nm), 316nm/(599–900 nm), and 392nm/(599–900 nm) for the 941 lightning events in order to specify the optical characteristics of IC, +CG, and -CG discharges. It is found that the PH intensity ratio of +CG discharges is the highest and that the PH intensity ratio of IC and -CG discharges is smaller than that of +CG discharge. We also found that the characteristics of the LSI intensity ratio are almost comparable to those of the PH intensity ratio. As the differences of the 337nm/762 nm, 337nm/(599–900 nm), and 392nm/(599–900 nm) ratio of IC, +CG, and -CG discharges are relatively large, these three ratios are a useful proxy for classifying the discharge types for additional 7349 lightning events detected by JEM-GLIMS in order to estimate the global ratio between IC and CG discharges (*Z* ratio).

1. Introduction

The detection and identification of intracloud (IC) discharges and cloud-to-ground (CG) discharges is essentially important to estimate the *Z* ratio (IC/CG). This ratio is an important parameter in order to study (1) the occurrence ratio of IC discharges to the total lightning flash and its regional and latitudinal dependences, (2) climatological differences of thundercloud development, (3) regional and global production of NO_X by lightning discharges, and (4) the quantitative contribution of lightning discharges to the global electric circuit (Mackerras and Darveniza, 1994; Mackerras et al., 1998; Buechler et al., 2000; Boccippio et al., 2001; Schumann and Huntrieser, 2007; Rycroft and Odzimek, 2010). However, most of previous ground-based observations focused on the detection of only CG discharges, which is comparatively easier than the detection of IC discharges over the globe by the ground-based electromagnetic wave observations (Orville et al., 2002; Greenberg and Price, 2004; Schulz et al., 2005; Sato et al., 2008; Yamashita et al., 2011).

In order to detect IC discharges and to identify discharge type, some ground-based and space-based observations were performed so far. The Australia Bureau of Methodology estimated the altitude range of the lightning channels in Brisbane, Australia. They found that the altitude range of the lightning channel of CG discharges and IC discharges lays between 0-4 km and 4–12 km, respectively (Mackerras, 1968; Ely et al., 2008; Fuchs and Rutledge, 2018; Mecikalski and Carey, 2018). Although the difference of the electromagnetic waveform radiated by lightning discharges enable us to distinguish between IC and CG discharges (Kitagawa and Brook, 1960; Mackerras, 1968; Smith et al., 2004), the detection of those electromagnetic waves would be limited only to a specific observational region since the electromagnetic waves radiated by IC discharges can not travel longer horizontal distances. The IC discharge channel tends to flow horizontally and has a

* Corresponding author. Department of Cosmosciences, Hokkaido University, Kita 10-Nishi 8, Kita-ku, Sapporo, Hokkaido, 060-0810, Japan.
E-mail address: kbjack@ep.sci.hokudai.ac.jp (K. Bandholnopparat).

https://doi.org/10.1016/j.jastp.2019.04.005
Received 15 October 2018; Received in revised form 5 April 2019; Accepted 5 April 2019
Available online 11 April 2019

horizontal current moment (Mackerass, 1968; Coleman et al., 2003; Tan et al., 2006). This current processes a weak horizontal electromagnetic waves and challenging to detect by the ground-based observation. Moreover, the ambiguity in identifying IC and CG discharges based on the VLF/LF signals occurs in the cases where the return stroke has high peak currents because the IC discharges with high-peak currents may be identified as CG discharges, while the CG discharges with low-peak currents can be identified as IC discharges (Davis et al., 2002; Orville et al., 2002).

Goodman et al. (1988) compared the characteristics of the optical signals emitted by IC and CG discharges from the cloud top and measured by the optical pulse sensor (OPS) on board the NASA U2 aircraft. This observational results provided an important fact that it is very difficult to classify the discharge type using only the OPS optical data. The spaceborne optical instruments such as Optical Transient Detector (OTD) and Lightning Imaging Sensor (LIS) can measure both IC and CG discharges over a much wider area than the OPS measurements (Williams et al., 2000; Christian et al., 2003; Koshak, 2010). Nevertheless, it is difficult to classify the discharge type only from the OTD and LIS optical data. In order to classify the discharge type of lightning, it is essential to use not only space-based optical data but also ground-based lightning data. This analysis technique was adopted in the studies by Boccippio et al. (2001) for the continental US, Soriano and de Pablo (2007) for European regions, and de Souza et al. (2009) for Brazil. However, this kind of analysis is applicable for the region where the ground-based lighting data are available. Thus, the classification of the lightning discharge type is still possible only in the specific target areas.

In contrast, if multispectral optical measurements of lightning emissions are performed from space, there is high possibility that the lightning discharge type can be easily distinguished (Adachi et al., 2016). When lightning emissions propagate from thunderclouds to space, they are scattered inside the thunderclouds and are absorbed and attenuated by the Earth's atmosphere. The optical emissions in the shorter wavelength, such as ultra violet (UV) (300–400 nm), violet (380–450 nm), and blue (450–495 nm), are more absorbed and attenuated than those in longer wavelength (Quick and Krider, 2013). This difference of the atmospheric transmission would be a key parameter for classifying the lightning discharge type since the IC and CG discharges tend to occur at higher and lower altitudes, respectively.

In this paper, we introduce the newly developed method for classifying lightning discharge type using multispectral optical data obtained by the Global Lightning and Sprite Measurements on Japanese Experiment Module (JEM-GLIMS) mission on board the International Space Station (ISS) and the ground-based lighting data provided by the Japanese Lightning Detection Network (JLDN), the National Lightning Detection Network (NLDN), the World Wide Lightning Location Network (WWLLN), and the Global ELF Observation Network (GEON) (for a detailed review on the ground-based lighting detection networks, see Matsui and Takano (2010); Olume (2002); Cummins and Murphy (2009); Nag et al. (2011); Rodger et al. (2006); Hutchins et al. (2012); Sato et al. (2003, 2008)). The optical intensity ratio of the blue and red emission derived from the JEM-GLIMS spectrophotometers data shows a clear difference between IC and CG discharges. It is also found the same result in the optical intensity ratio between wideband (λ = 768–830 nm) and narrowband (λ = 760–775 nm) camera data. These results imply that the lightning discharge type can be determined by the multispectral optical data obtained from space. In section 2, JEM-GLIMS data, ground-based lightning data, and data analysis technique are introduced. In section 3, the optical intensity ratio derived from JEM-GLIMS spectrophotometers and cameras and the interpretations of these results are presented. Finally, the conclusions of this research are presented in section 4.

2. Data and methods

The JEM-GLIMS instruments are designed to measure lightning discharges and lightning-associated transient luminous events (TLEs) from the ISS in the nadir direction and comprise both optical instruments and electromagnetic waves receivers (Sato et al., 2015). The JEM-GLIMS optical instruments consist of the six-channel spectrophotometers (PHs) and the Lightning and Sprite Imager (LSI) composed of wideband and narrowband Complementary Metal Oxide Semiconductor (CMOS) cameras. The PHs measure the absolute optical intensity of lightning emissions in the wavelength range of 150–280 nm (PH1), 310–321 nm (PH5), 332–342 nm (PH2), 386–397 nm (PH6), 599–900 nm (PH4), 755–766 nm (PH3), respectively (Sato et al., 2011a, 2015, 2016; Adachi et al., 2016). The wideband CMOS camera (LSI-1) acquires the optical images in the wavelength range of 768–830 nm, while the narrowband CMOS camera (LSI-2) in the wavelength range of 760–775 nm (Sato et al., 2011b, 2015, 2016). Fig. 1 shows the modeled atmospheric transmittance in the wavelength range of 200–1000 nm calculated by the Moderate Resolution Atmospheric Transmission (MODTRAN) code (Berk et al., 2014, 2015). As the optical emission in 762 nm propagating from the troposphere to the ISS altitude is severely absorbed by the atmospheric oxygen molecules, LSI-1 and LSI-2 mainly observe the lightning emissions and TLE emissions, respectively (Blanc et al., 2004, 2007; Sato et al., 2015, 2016). JEM-GLIMS conducted the lightning and TLE optical observations in the local time (LT) range of 19:00–05:00 LT (Sato et al., 2015). More detailed information on the specifications and the operation of the JEM-GLIMS instruments can be found in the papers of Sato et al. (2015, 2016), and Adachi et al. (2016).

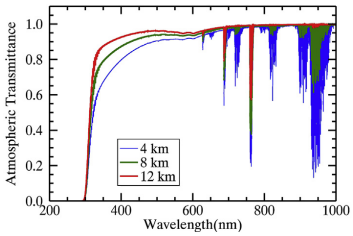

Fig. 1. Modeled atmospheric transmittance in the wavelength range of 200-1000 nm calculated by the MODTRAN code. The blue, green and red lines show the transmittance from a light source located at the 4, 8, and 12 km altitude to the zenith direction, respectively.

In this study, we selected 1057 lightning events detected by JEM-GLIMS in 2014, that are not accompanied by TLEs, in order to estimate the PH intensity ratio and LSI intensity ratio of IC, +CG, and -CG discharges. These lightning events were mainly detected in the latitudinal range from 51°S to 51°N over both oceanic and continental regions as shown in Fig. 2. Note that, the gray hatched area in this figure corresponds to the region where JEM-GLIMS did not conduct the observations due to the limitation of the orbital inclination angle of the ISS.

The flow chart showing how we classify the discharge type of the JEM-GLIMS lightning events using the JLDN, NLDN, WWLLN, and GEON is summarized in Fig. 3. As a first step, we compared the JEM-GLIMS data to the ground-based lightning data detected by the JLDN, NLDN, and WWLLN in order to identify the discharge types of the JEM-GLIMS lightning events. We adopted two criteria to identify the coincidence between the JEM-GLIMS lightning events and ground-based lightning events: (i) the horizontal distance (D) between the JEM-GLIMS nadir point and the ground-based lightning location, and (ii) the time difference (Δt) between the detection time of the JEM-GLIMS lightning event (T_{glims}) and the that of the ground-based lightning event (T_{ground}). When we calculate Δt, the time lag of 1.5 ms representing the delay from the light source to the cloud top due to the multi-path scattering in thunderclouds (Koshak et al., 1994) and of 1.3 ms which is the average travel time of light from cloud top to the ISS altitude are subtracted from T_{glims}. If D and Δt are found to be $D \leq 90$ km and $\Delta t \leq$

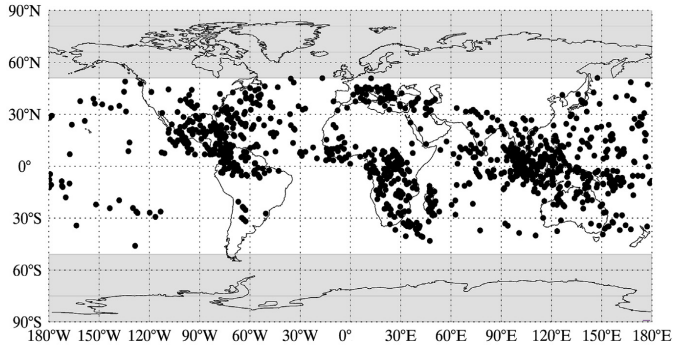

Fig. 2. The distribution of the 1057 selected lightning events detected by JEM-GLIMS in 2014 and used in this study to identify the discharge types by comparing them to the ground-based lightning data.

1.5 ms, respectively, the JEM-GLIMS lightning event is identified to be the same lightning event detected by the ground-based lightning networks. The criterion 90 km is defined based on the half radius of the PH field of view (FOV) and the location error of the ground-based lightning network, *i.e.,* 500 m for the NLDN (Nag et al., 2011), 10 km for the WWLLN (Hutchins et al., 2012), and > 500 m for the JLDN (Matsui and Takano, 2010). The procedure for calculating the criterion $D \leq 90$ km is given in Appendix A.

Secondly, the polarity of CG discharges, *i.e.,* +CG or -CG was obtained. Although the polarity of CG discharges is already provided by the JLDN and the NLDN, it is not provided by the WWLLN. When the parent lightning of the JEM-GLIMS events is found in the WWLLN data, we further analyze the ELF magnetic field waveform data detected by the GEON and estimated the polarity of CG discharges using the magnetic direction finding method, which is introduced in Sato et al., (2003). According to these procedures, the JEM-GLIMS lightning events were classified into one of four categories: 1) "IC discharge", 2) "+CG discharge", 3) "-CG discharge", and 4) "ambiguous discharge events". Note that if the amplitude of the ELF signal is too weak (< 10 pT) to estimate the polarity and the wave propagation path, the JEM-GLIMS lightning events were classified into the "ambiguous discharge event".

Finally, the PH intensity ratio (PH2/PH3, PH5/PH3, PH6/PH3, PH2/PH4, PH5/PH4, and PH6/PH4) and the LSI intensity ratio (LSI-2/LSI-1) were computed for each event.

3. Results and discussion

3.1. Classification of the discharge type

By comparing the JEM-GLIMS lightning data and the ground-based lightning data, we succeeded in identifying the discharge type in 941 of 1057 events, which corresponds to 89.0% of the total events. It is found that 582 (55.1%), 93 (8.80%), 266 (25.2%), and 116 (10.9%) of 1057 events were identified to be IC, +CG, -CG discharges, and ambiguous discharge events, respectively.

Fig. 4(a), (b), and (c) show the global distribution of the identified IC, +CG, and -CG discharges, respectively. It is found that the 78.9% of the identified IC discharges occurred mainly between 20°S and 20°N. The same characteristics can be seen in the global map of the identified -CG discharges (Fig. 4(c)). It is found that 73.6% of those -CG discharges were occurred in the latitudinal range 20°S to 20°N. In contrast, the distribution of the identified + CG discharges shown in Fig. 4(b)

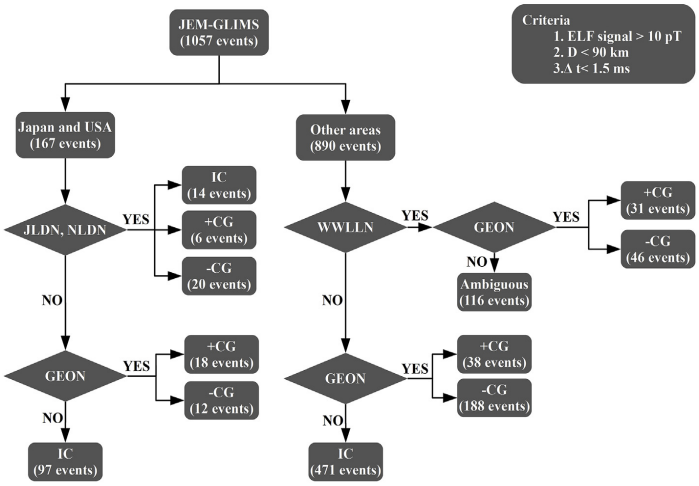

Fig. 3. Flow chart showing how the discharge type of the JEM-GLIMS lightning events are classified into IC, -CG and +CG using the ground-based lightning data (JLDN, NLDN, WWLLN, and GEON).

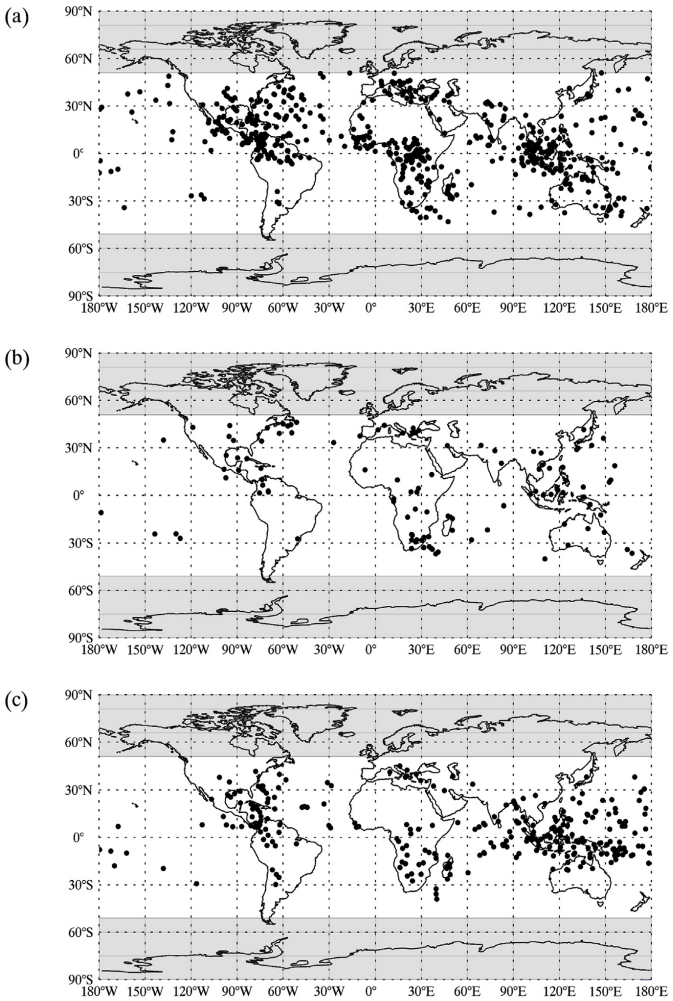

Fig. 4. (a) Global distribution of the identified 582 IC discharge events. (b), (c) Same as (a) except for the identified 93 +CG and 266 -CG discharge events, respectively. These lightning events were detected by JEM-GLIMS optical instruments in 2014.

does not show the same characteristics as that of the IC and -CG discharges. The number of identified + CG discharges in the tropics ($N_{tropics}$) (*i.e.,* 20°S - 20°N) and in the mid latitude (N_{mid}) (*i.e.,* 40°S - 20°S and 20°N - 40°N) is estimated to be ($N_{tropics}$:N_{mid}) = (0.92:1.0).

3.2. PH intensity ratio

Fig. 5 shows an example of a JEM-GLIMS + CG discharge event. This event was detected at 06:19:19.72434 UT on 25 September 2014, when JEM-GLIMS was located at (108.301°W, 29.998°N) over Mexico. Fig. 5(a) shows the light curve data obtained by PH with absolute intensity values. In this plot, $t = 0$ ms is the time at 06:19:19.72434 UT. Fig. 5(b) shows the logarithmic of PH intensity ratios of this lightning event derived from the light curve data in Fig. 5(a). For the further analysis, the logarithmic of PH intensity ratio at $t = 0$ ms was used.

Fig. 6(a), (b), and (c) are the histogram of the blue-to-red ratio of the PH intensities, *i.e.,* PH2/PH3, PH5/PH3, and PH6/PH3 ratios for the identified 582 IC, 93 + CG, and 266 -CG discharges, respectively. Fig. 6(d), (e), and (f) are the same as Fig. 6(a)–(c) except for the PH2/PH4, PH5/PH4, and PH6/PH4 ratios, respectively. The median value of the logarithmic PH intensity ratio is summarized in Table 1. As shown in Fig. 6 and Table 1, it is found that the PH intensity ratio for the +CG discharges is the highest in all cases. It is also clear that the PH intensity ratios of the IC and -CG discharges are smaller than that of the +CG discharges and that the ratio of -CG discharges is always the smallest. These results would be explained by the difference of the light source altitude of lightning discharges since the atmospheric transmittance in the blue and red wavelengths are different as shown in Fig. 1. The normal arc-type discharge channels of +CG discharges tend to occur at higher altitude near the cloud top (Lu et al., 2012). Thus, the PH intensity ratio becomes higher since both blue and red emissions can propagate from the +CG discharges to the JEM-GLIMS optical

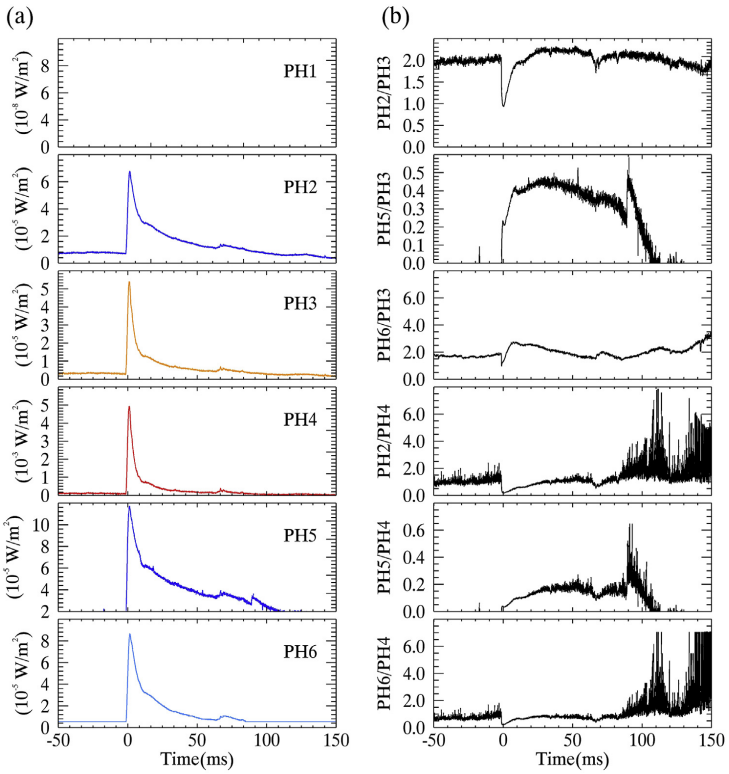

Fig. 5. An example of (a) light curve data obtained by the six PH channels at 06:19:19.72434 UT on 25 September 2014. (b) Intensity ratios between blue and red PH channels.

instruments with the relatively low attenuation rate. The high PH intensity ratio value can be found in IC discharges as the discharge channels generally located at the middle of the thunderclouds (López et al., 2016). In contrast, based on recent LMA/VHF studies (Sun et al., 2016; Lyu et al., 2016) and high-speed imaging (Ballarotti et al., 2005; Stolzenburg et al., 2013), the discharge channels of -CG discharges tend to occur at lower altitude or near the cloud bottom. Consequently, the PH intensity ratio of -CG discharges becomes lower than that of +CG and IC discharges because the red emission of -CG discharges can mainly arrive at the JEM-GLIMS optical instruments.

As shown in Fig. 6 and Table 1, the distribution of the PH intensity ratios of the IC, +CG, and -CG discharges show a clear difference. Especially, the difference of the PH2/PH3, PH2/PH4, and PH6/PH4 ratios among those discharges are the largest. Thus, we can conclude that these PH intensity ratios are useful proxy to distinguish the discharge type for others JEM-GLIMS lightning events detected during the mission period of 2012–2015.

3.3. LSI intensity ratio

The LSI intensity ratio (LSI-2/LSI-1) of the identified IC, +CG, and -CG discharges were also calculated. Fig. 7(a) and (b) are the example images of LSI-1 and LSI-2. This lightning event is the same event as Fig. 5(a). The strong lightning emission was measured by LSI-1. As shown in Fig. 7(b), the optical emissions are also confirmed in the LSI-2 image. Then, we calculated the LSI intensity ratio using the absolute optical intensity at the pixel where the highest optical intensity was detected in the LSI-2 image.

Fig. 8 is the histogram of the calculated LSI intensity ratio. The median value and standard deviation are provided in this figure and Table 1. Note that the lightning event number used for this LSI intensity ratio analysis (73 events) is smaller than that in the PH intensity ratio analysis. This is because the LSI-2 could detect lightning optical emissions only in 207 (19.6%) from 1057 lightning events since the lightning emission in 762 nm was almost entirely absorbed by the atmospheric oxygen molecules as shown in Fig. 1.

As shown in Fig. 8, the median values of IC, +CG and -CG discharges were estimated to be 0.080, 0.11, and 0.020, respectively. It is clear that the LSI intensity ratio of +CG discharges is the highest followed by IC and -CG discharges. These results well agree with the result of PH intensity ratios presented in section 3.2 and in Fig. 6. Although the LSI-1 is equipped with the wideband filter (768–830 nm) that mainly observes lightning emissions, the LSI-2 equipped with a narrowband filter (760–775 nm) tends to observe both the lightning-associated TLE emissions and the parent lightning emissions whose light source locates near the cloud top (Sato et al., 2015). Lu et al., (2012) pointed out that the normal discharge channels of +CG discharges tend to occur at the higher altitude in the thundercloud or near the cloud top. Consequently, the LSI intensity ratio of +CG discharges becomes the highest since the photons from +CG lightning discharges channel in the wavelength of 760–775 nm (LSI-2) escape to the ISS altitude. This can also happen in the IC discharges because the discharge channel of IC discharges tends to locate at the middle altitude of the thundercloud (López et al., 2016). In contrast, the normal discharge channels of -CG

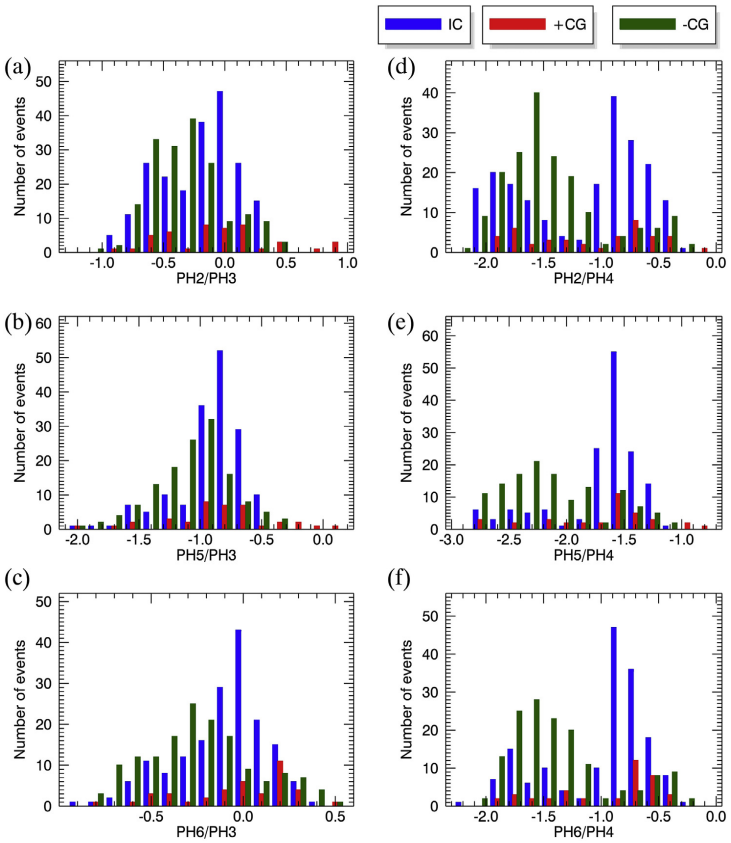

Fig. 6. Histograms of the logarithmic of PH intensity ratio. The blue, red and green bars show the ratio of PH2/PH3, PH5/PH3, PH6/PH3, PH2/PH4, PH5/PH4, PH6/PH4 of IC, +CG, and -CG discharges, respectively.

Table 1
Summary of the PH and LSI intensity ratios of +CG, IC, and -CG discharges. In this table, the median value of the logarithmic PH and LSI intensity ratios is presented.

	+CG	σ	IC	σ	-CG	σ
log(PH2/PH3)	0.010	0.42	−0.058	0.37	−0.31	0.28
log(PH5/PH3)	−0.65	0.51	−0.75	0.42	−1.0	0.45
log(PH6/PH3)	0.042	0.31	0.024	0.28	−0.22	0.31
log(PH2/PH4)	−0.69	0.65	−0.78	0.60	−1.5	0.43
log(PH5/PH4)	−1.4	0.62	−1.5	0.46	−2.2	0.47
log(PH6/PH4)	−0.69	0.50	−0.72	0.44	−1.5	0.46
LSI-2/LSI-1	0.11	0.061	0.080	0.050	0.020	0.070

discharges occurs at the lower altitude or near the cloud bottom (Mackerras, 1968). Consequently, the LSI intensity ratio of -CG discharges is lower than that of +CG and IC discharges because the optical emissions at the wavelength range of 760–775 nm (LSI-2) tend to be more absorbed.

4. Conclusion

A total of 1057 JEM-GLIMS lightning events detected over the land and oceanic regions in the latitudinal range from 51°S to 51°N were analyzed together with the ground-based lightning data by the JLDN, NLDN, WWLLN, and GEON and were classified into the IC, +CG and -CG discharges. The PH and the LSI intensity ratios of the peak lightning emissions were calculated, and their histograms were estimated. It is found that there is a difference in these histograms between the IC, +CG and -CG discharges. The median value of the PH and LSI intensity ratios of the identified + CG discharges was found to be the highest, while that of the IC discharges was found to be smaller than that of +CG charges but larger than that of -CG discharges. These facts are strongly related to the difference of the atmospheric transmission from the lightning discharges channels to the ISS. Consequently, these parameters, especially the PH2/PH3, PH2/PH4 and PH6/PH4 ratios, were found to be a useful proxy for distinguishing between discharge types for other JEM-GLIMS lightning events measured in 2012–2015 and for the lightning events measured by the future space missions, for example the Atmosphere-Space Interactions Monitor (ASIM) and the Tool for the Analysis of RAdiation from lightNIng and Sprites (TARANIS), in order to quantitatively estimate the latitudinal dependence of the IC-to-CG ratio (Z values). We aware that our research may have two limitations. The first is that this method may not be perfect for identifying the discharge type of a single lightning event only from the space-based observation data because the PH and LSI intensity ratios have wider distribution as shown in Figs. 6 and 8. The second is that this method may not be suitable for classifying between -CG discharge

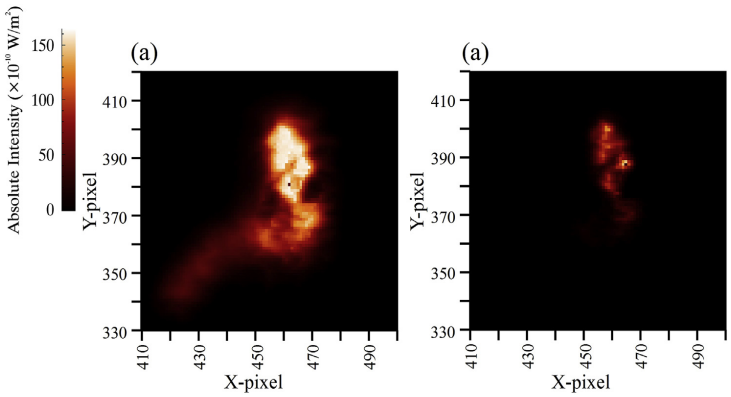

Fig. 7. An example of (a) LSI-1 lightning optical image at 06:19:19.72434 UT on 25 September 2014. (b) Same as (a) except for LSI-2. In Figure 7(b), the position of the maximum absolute intensity was at pixel X = 465 and Y = 378, and that intensity was used to calculate the LSI intensity ratio.

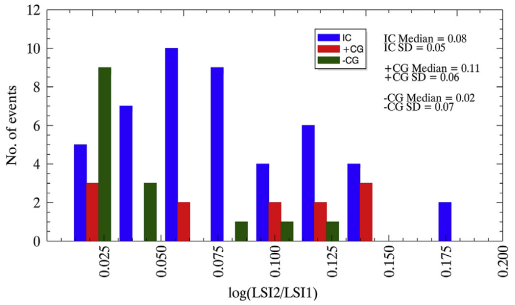

Fig. 8. Histograms of the LSI intensity ratio of 47 IC (blue), 12 +CG (red), and 14 -CG (green) discharges.

and +CG discharge that arise from the lower positive charge region. The discharge channel of this + CG discharge locates between the cloud bottom and the ground. Consequently, using the PH and LSI intensity ratio, the +CG discharge that initiats from the lower positive charge region might be identified as -CG discharge. From these limitations, it would be essential to utilize not only satellite data but also the ground-based lightning data.

Acknowledgments

This work was supported by JSPS KAKENHI Grant-in-Aid for Scientific Research (B) Number 16H04055 and 24340117, and MEXT KAKENHI Grant-in-Aid for Specially Promoted Research Number 19002002. We would like to thank the Japanese Lightning Detection Network, the National Lightning Detection Network, the World Wide Lightning Location Network, and the Global ELF Observation Network staffs for providing the lightning data. All data analyses and figures in this study were performed using the Interactive Data Language (IDL).

Appendix A. The spatial and temporal criteria

The horizontal distance (D) between the JEM-GLIMS nadir point and the ground-based lightning location, and the time difference (Δt) between the detection time of the JEM-GLIMS lightning event (T_{glims}) and the that of the ground-based lightning event (T_{ground}) were used to identify the coincidence between the JEM-GLIMS lightning events and ground-based lightning events. The time condition ($T_{glims} - T_{ground}$) < 1.5 ms was estimated by the delays time (0.2 ms) of light in thunderclouds due to the multi-path scattering (Koshak et al., 1994), and the optical propagation time (1.35 ms) from the cloud top at the altitude of 15 km to the JEM-GLIMS altitude of 411.0 km. Then, the expected detection time of the lightning emission at the ISS would be T_{ground} + 1.5 ms.

Secondly, condition D < 90 km was estimated from the location of JEM-GLIMS. A lightning event which occurred anywhere inside the FOV of the JEM-GLIMS optical instruments could be detected by JEM-GLIMS. As shown in Fig. A1, the radius of the FOV of the optical instruments is 160 km. But, for the selection of the lightning events in this study, we limited the radius of 80 km, which is the half of the FOV. The reason of this is that the intensities of the lightning blue emissions would be severely affected by the effect of the atmospheric transmittance if the lightning occurred near the edge of the FOV, which may cause the large error in the estimation of the blue-to-red intensity ratios. We also took into account the location error of the ground-based lightning detection network is 10.0 km (Hutchins et al., 2012; Matsui and Takano, 2010; Nag et al., 2011). Consequently, if the distance D is less than 90.0 km and the time difference between a JEM-GLIMS lightning event and a ground-based lightning event is less than 1.5 ms, it was defined to be the same event.

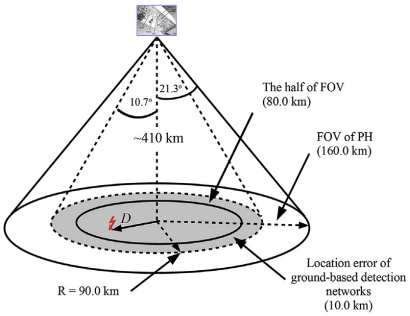

Fig. A1. Schematic illustration showing the FOV of PHs and a distance between JEM-GLIMS nadir point and a ground-based lightning event (*D*).

Appendix B. The absolute intensity of LSI image

JEM-GLIMS optical instruments have been calibrated with a known source in the laboratory before it was launched. Using calibration data, the raw count data are converted into the absolute intensity (W/m^2). As a first step, the relation between the absolute intensity (I_A) from a known light source and the relative intensity value (I_R) obtained by the JEM-GLIMS optical instruments was measured as shown in Table A1. Then, the variation of the absolute intensity is plotted toward the relative intensities, as shown in Fig. B1, in order to find an equation which shows the relation between the absolute intensity (I_A) and the relative intensity (I_R).

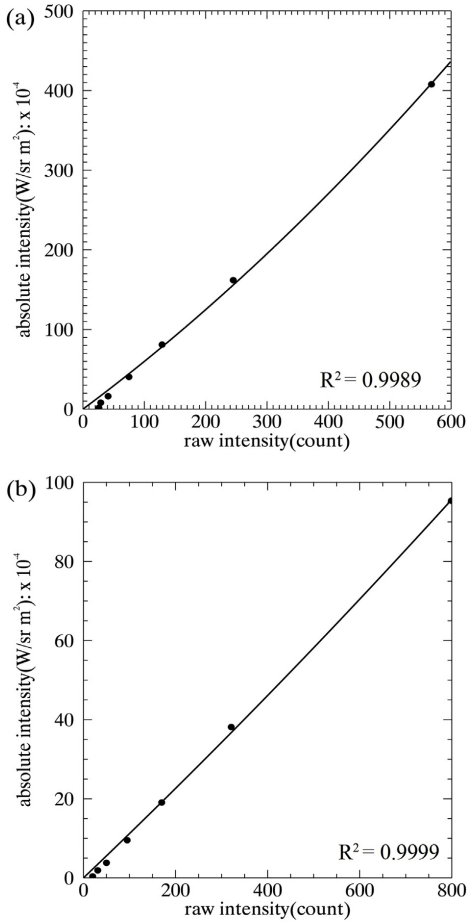

Fig. B1. The variation of the absolute and relative intensities for (a) LSI-1 and (b) LSI-2.

To perform the fitting, we used two functions: (i) the linear function, $f(x) = Ax + B$ and (ii) polynomial function, $f(x) = Ax^2 + Bx + C$, where A, B, and C are the parameter to be fitted. It is found that the coefficient of determination (R^2) is 0.99832 (linear) and 0.99897 (polynomial) for LSI-1 and 0.99984 (linear) and 0.99994 (polynomial) for LSI-2, respectively. Consequently, the polynomial function (equation (B1) and B2) was used to transform the relative intensity into the absolute intensity.

$$I_{(A_{LSI\ 1})} = 2.5937 \times 10^{-8} I^2_{(R_{LSI\ 2})} + 5.7251 \times 10^{-5} I_{(R_{LSI\ 1})}\ (\mathrm{W/m^2}) \quad \text{(B1)}$$

$$I_{(A_{LSI\ 2})} = 1.07833 \times 10^{-9} I^2_{(R_{LSI\ 2})} + 1.1097 \times 10^{-5} I_{(R_{LSI\ 2})}\ (\mathrm{W/m^2}) \quad \text{(B2)}$$

Appendix C. Supplementary data

Supplementary data to this article can be found online at https://doi.org/10.1016/j.jastp.2019.04.005.

Table A1
the absolute intensity from known light source (I_S) and the relative intensity (I_R) obtained by JEM-GLIMS optical instruments.

LSI-1		LSI-2	
I_s (W/sr·m²·nm)	I_R (counts)	I_s (W/sr·m²·nm)	I_R (counts)
5.0×10^{-4}	568	5.0×10^{-4}	799
2.0×10^{-4}	245	2.0×10^{-4}	321

(*continued on next page*)

Table A1 (*continued*)

LSI-1		LSI-2	
I_s (W/sr·m^2·nm)	I_R (counts)	I_s (W/sr·m^2·nm)	I_R (counts)
1.0×10^{-4}	129	1.0×10^{-4}	170
5.0×10^{-5}	75	5.0×10^{-5}	95
2.0×10^{-5}	41	2.0×10^{-5}	51
1.0×10^{-5}	29	1.0×10^{-5}	31
2.0×10^{-6}	26	2.0×10^{-6}	18

References

Adachi, T., Sato, M., Ushio, T., Yamazaki, A., Suzuki, M., Kikuchi, M., Takahashi, Y., Inan, U., Linscott, I., Hobara, Y., Frey, H.U., Mende, S.B., Chen, A.B., Hsu, R., Kusunoki, K., 2016. Identifying the occurrence of lightning and transient luminous events by nadir spectrophotometric observation. J. Atmos. Sol. Terr. Phys. 145, 85–97. https://doi.org/10.1016/j.jastp.2016.04.010.

Ballarotti, M.G., Saba, M.M.F., Pinto Jr., O., 2005. High-speed camera observations of negative ground flashes on a millisecond-scale. Geophys. Res. Lett. 32, L23802. https://doi.org/10.1029/2005GL023889.

Berk, A., Conforti, P., Kennett, R., Perkins, T., Hawes, F., van den Bosch, J., 2014. MODTRAN6: a major upgrade of the MODTRAN radiative transfer code. In: Proc. SPIE 9088, Algorithms and Technologies for Multispectral, Hyperspectral, and Ultraspectral Imagery, https://doi.org/10.1117/12.2050433. XX, 90880H.

Berk, A., Conforti, P., Hawes, F., 2015. An accelerated line-by-line option for MODTRAN combining on-the-fly generation of line center absorption with 0.1 cm-1 bins and pre-computed line tails, *Proc. SPIE 9471*. Algorithms and Technologies for Multispectral, Hyperspectral, and Ultraspectral Imagery XXI, 947217. https://doi.org/10.1117/12.2177444.

Blanc, E., Farges, T., Roche, R., Brebion, D., Hua, T., Labarthe, A., Melnikov, V., 2004. Nadir observations of sprites from the international space station. J. Geophys. Res. 109, A02306. https://doi.org/10.1029/2003JA009972.

Blanc, E., Farges, T., Belyaev, A.N., Alpatov, V.V., Brebion, D., Labarthe, A., Melnikov, V., 2007. Main Results of LSO (Lightning and Sprite Observations) on Board of the International Space Station. Microgravity Science and Technology 19. 80-84. 10.1007/BF02919458.

Boccippio, D.J., Cummins, K.L., Christian, H.J., Goodman, S.J., 2001. Combined satellite- and surface-based estimation of the intracloud–cloud-to-ground lightning ratio over the continental United States. Mon. Weather Rev 129, 108–129. https://doi.org/10.1175/1520-0493(2001)129<0108:CSASBE>2.0.CO;2.

Buechler, D.E., Driscoll, K.T., Goodman, S.J., Christian, H.J., 2000. Lightning activity within a tornadic thunderstorm observed by the Optical Transient Detector (OTD). Geophys. Res. Lett. 27, 2253–2256. https://doi.org/10.1029/2000GL011579.

Christian, H.J., et al., 2003. Global frequency and distribution of lightning as observed from space by the Optical Transient Detector. J. Geophys. Res. 108 (D1), 4005. https://doi.org/10.1029/2002JD002347.

Coleman, L.M., Marshall, T.C., Stolzenburg, M., Hamlin, T., Krehbiel, P.R., Rison, W., Thomas, R.J., 2003. Effects of charge and electrostatic potential on lightning propagation. J. Geophys. Res. 108 (D9), 4298. https://doi.org/10.1029/2002JD002718, 2003.

Cummins, K.L., Murphy, M.J., 2009. An overview of lightning locating systems: history, techniques, and data uses, with an in-depth look at the U.S. NLDN. IEEE Trans. Electromagn Compat. 51 (3), 499–518. https://doi.org/10.1109/TEMC.2009.2023450.

Davis, S.M., Suszcynsky, D.M., Light, T.E.L., 2002. FORTE observations of optical emissions from lightning: optical properties and discrimination capability. Journal of Geophysical Research Atmospheres 107 (21), 1–5. https://doi.org/10.1029/2002JD00243.

de Souza, P.E., Pinto, O., Pinto, I.R.C.A., Ferreira, N.J., dos Santos, A.F., 2009. The intracloud/cloud-to-ground lightning ratio in Southeastern Brazil. Atmos. Res. 91 (2–4), 491–499. https://doi.org/10.1016/j.atmosres.2008.06.011.

Ely, B.L., Orville, R.E., Carey, L.D., Hodapp, C.L., 2008. Evolution of total lightning structure in a leading-line, trailing stratiform mesoscale convective system over Houston. Texas. J. Geophys. Res. 113, D08114. https://doi.org/10.1029/2007JD008445.

Fuchs, B.R., Rutledge, S.A., 2018. Investigation of lightning flash locations in isolated convection using LMA observations. J. Geophys. Res.: Atmosphere 123. https://doi.org/10.1002/2017JD027569.

Goodman, S.J., Christian, H.J., Rust, W.D., 1988. A comparison of the optical pulse characteristics of intracloud and cloud-to-ground lightning as observed above clouds. J. Appl. Meteorol. 1369–1381. https://doi.org/10.1175/1520-0450(1988)027<1369:ACOTOP>2.0.

Greenberg, E., Price, C., 2004. A global lightning location algorithm based on the electromagnetic signature in the Schumann resonance band. J. Geophys. Res. D Atmos. 109 (21), 1–8. https://doi.org/10.1029/2004JD004845.

Hutchins, M.L., Holzworth, R.H., Brundell, J.B., Rodger, C.J., 2012. Relative detection efficiency of the World Wide lightning location network. Radio Sci. 47 (6), 1–9. https://doi.org/10.1029/2012RS005049.

Kitagawa, N., Brook, M., 1960. A comparison of intracloud and cloud-to-ground lightning discharges. J. Geophys. Res. 65 (4), 1189–1201. https://doi.org/10.1029/JZ065i004p01189.

Koshak, W.J., Solakiewicz, R.J., Phanord, D.D., Blakeslee, R.J., 1994. Diffusion model for lightning radiative transfer. J. Geophys. Res. 99 (7), 14361–14371 0148-0227/94/94JD-00022505.00.

Koshak, W.J., 2010. Optical characteristics of OTD flashes and the Implications for flash-type discrimination. J. Atmos. Ocean. Technol. 27 (11), 1822–1838. https://doi.org/10.1175/2010JTECHA1405.1.

López, J.A., Montanyà, J., Van Der Velde, O., Romero, D., Aranguren, H., Torres, H., Taborda, J., Martinez, J., 2016. First data of the Colombia lightning mapping array - COLMA. In: Proceeding of the 33rd International Conference on Lightning Protection, ICLP 2016, Estoril, Portugal, https://doi.org/10.1109/ICLP.2016.7791436.

Lu, G., Cummer, S.A., Blakeslee, R.J., Weiss, S., Beasley, W.H., 2012. Lightning morphology and impulse charge moment change of high peak current negative strokes. Journal of Geophysical Research Atmospheres 117 (4), 1–16. https://doi.org/10.1029/2011JD016890.

Lyu, F., Cummer, S.A., Lu, G., Zhou, X., Weinert, J., 2016. Imaging lightning intracloud initial stepped leaders by low-frequency interferometric lightning mapping array. Geophys. Res. Lett. 43, 5516–5523. https://doi.org/10.1002/2016GL069267.

Mackerras, D., 1968. A comparison of discharge processes in cloud and ground lightning flashes. J. Geophys. Res. 73, 1175–1183. https://doi.org/10.1029/JB073i004p01175.

Mackerras, D., Darveniza, M., 1994. Latitudinal variation of lightning occurrence characteristics. J. Geophys. Res.: Atmosphere 99 (D5), 10813–10821. https://doi.org/10.1029/94JD00018.

Mackerras, D., Darveniza, M., Orville, R.E., Williams, E.R., Goodman, S.J., 1998. Global lightning: total, cloud and ground flash estimates. J. Geophys. Res. 103 (16). https://doi.org/10.1029/98JD01461. 19,791-19,809.

Matsui, M., Takano, N., 2010. Evaluation of Lightning Location Accuracy of JLDN with a Lightning Video Camera System. Paper presented Asia-Pacific International Symposium on Electromagnetic Compatibility, Beijing, China.

Mecikalski, R.M., Carey, L.D., 2018. Radar reflectivity and altitude distributions of lightning flashes as a function of three main storm types. J. Geophys. Res. 123 (12). https://doi.org/10.1029/2018JD029238. 814–12,828.

Nag, A., et al., 2011. Evaluation of U.S. National Lightning Detection Network performance characteristics using rocket-triggered lightning data acquired in 2004-2009. J. Geophys. Res. 116, D02123. https://doi.org/10.1029/2010JD014929.

Olume, V., 2002. The north American lightning detection network (NALDN)— first results : 1998 – 2000. Mon. Weather Rev. 130, 2098–2109. https://doi.org/10.1175/1520-0493(2002)130.

Orville, R.E., Huffines, G.R., Burrows, W.R., Holle, R.L., Cummins, K.L., 2002. The north American lightning detection network (NALDN)-first results: 1998 – 2000. Mon. Weather Rev. 130, 2098–2109.

Quick, M.G., Krider, E.P., 2013. Optical power and energy radiated by natural lightning. Journal of Geophysical Research Atmospheres 118 (4), 1868–1879. https://doi.org/10.1002/jgrd.50182.

Rodger, C.J., Werner, S., Brundell, J.B., Lay, E.H., Thomson, N.R., Holzworth, R.H., Dowden, R.L., 2006. Detection efficiency of the VLF world-wide lightning location network (WWLLN): initial case study. Ann. Geophys. 24 (12), 3197–3214. https://doi.org/10.5194/angeo-24-3197-2006.

Rycroft, M.J., Odzimek, A., 2010. Effects of lightning and sprites on the ionospheric potential, and threshold effects on sprite initiation, obtained using an analog model of the global atmospheric electric circuit. J. Geophys. Res. 115, A00E37. https://doi.org/10.1029/2009JA014758.

Sato, M., Fukunishi, H., Kikuchi, M., Yamagishi, H., Lyons, W.A., 2003. Validation of sprite-inducing cloud-to-ground lightning based on ELF observations at Syowa station in Antarctica. J. Atmos. Sol. Terr. Phys. 65 (5), 607–614. https://doi.org/10.1016/S1364-6826(02)00327-9.

Sato, M., Takahashi, Y., Yoshida, A., Adachi, T., 2008. Global distribution of intense lightning discharges and their seasonal variations. J. Phys. D Appl. Phys. 41 (23). https://doi.org/10.1088/0022-3727/41/23/234011.

Sato, M., Takahashi, Y., Suzukim, M., Yamazaki, A., Ushio, T., 2011a. Six-channel spectrophotometers(PH) onboard JEM-GLIMS. IEEJ TRANS. Fundam. Meter. 131 (112), 1000–1005. https://doi.org/10.1541/ieejfms.131.1000.

Sato, M., Takahashi, Y., Kikuchi, M., Suzuki, M., Yamazaki, A., Ushio, T., 2011b. Lightning and sprite imager (LSI) on board JEM-GLIMS. IEEJ TRANS. F. M. 131 (112), 994–999. https://doi.org/10.1541/ieejfms.131.994.

Sato, M., et al., 2015. Overview and early results of the global lightning and sprite measurements mission. J.Geophys. Res. Atmos. 120, 3822–3851. https://doi.org/10.1002/2014JD022428.

Sato, M., et al., 2016. Horizontal distributions of sprites derived from the JEM-GLIMS. J. Geophys. Res. - Atmos. 121, 3171–3194. https://doi.org/10.1002/2015JD024311.
Schulz, W., Cummins, K., Diendorfer, G., Dorninger, M., 2005. Cloud-to-ground lightning in Austria: a 10-year study using data from a lightning location system. J. Geophys. Res. D Atmos. 110 (9), 1–20. https://doi.org/10.1029/2004JD005332.
Schumann, U., Huntrieser, H., 2007. The global lightning-induced nitrogen oxides source. Atmos. Chem. Phys. 7 (14), 3823–3907. https://doi.org/10.5194/acp-7-3823-2007.
Smith, D.A., Heavner, M.J., Jacobson, A.R., Shao, X.M., Massey, R.S., Sheldon, R.J., Wiens, K.C., 2004. A method for determining intracloud lightning and ionospheric heights from VLF/LF electric field records. Radio Sci. 39 (1). https://doi.org/10.1029/2002RS002790. n/a-n/a.
Soriano, L.R., de Pablo, F., 2007. Total flash density and the intracloud/cloud-to-ground lightning ratio over the Iberian Peninsula. Journal of Geophysical Research Atmospheres 112 (13), D13114. https://doi.org/10.1029/2006JD007624.
Stolzenburg, M., Marshall, T.C., Karunarathne, S., Karunarathna, N., Vickers, L.E., Warner, T.A., Orville, R.E., Betz, H.-D., 2013. Luminosity of initial breakdown in lightning. J. Geophys. Res. Atmos. 118, 2918–2937. https://doi.org/10.1029/2012JD018675.
Sun, Z., Qie, X., Liu, M., Jiang, R., Wang, Z., Zhang, H., 2016. Characteristics of anegative lightning with multiple-groundterminations observed by a VHF lightninglocation system. J. Geophys. Res. Atmos. 121, 413–426. https://doi.org/10.1002/2015JD023702.
Tan, Y.B., Tao, S.C., Zhu, B.Y., 2006. Fine-resolution simulation of the channel structures and propagation features of intracloud lightning. Geophys. Res. Lett. 33, L09809. https://doi.org/10.1029/2005GL025523.
Williams, E., Rothkin, K., Stevenson, D., Boccippio, D., 2000. Global lightning variations caused by changes in thunderstorm flash rate and by changes in the number of thunderstorms. J. Appl. Meteorol. 39, 2223–2230. https://doi.org/10.1175/1520-0450(2001)040<2223:GLVCBC>2.0.CO;2.
Yamashita, K., Takahashi, Y., Sato, M., Kase, H., 2011. Improvement in lightning geo-location by time-of-arrival method using global ELF network data. J. Geophys. Res.: Space Physics 116 (2), 1–12. https://doi.org/10.1029/2009JA014792.

Bibliography

Abarca, S., Corbosiero, K., and Galarneau, T. (2010). An evaluation of the world wide lightning location network (wwlln) using the national lightning detection network (nldn) as ground truth. Journal of Geophysical Research, 115.

Adachi, T., Sato, M., Ushio, T., Yamazaki, A., Suzuki, M., Kikuchi, M., Takahashi, Y., Inan, U., Linscott, I., Hobara, Y., Frey, H., Mende, S., Chen, A., Hsu, R.-R., and Kusunoki, K. (2016). Identifying the occurrence of lightning and transient luminous events by nadir spectrophotometric observation. Journal of Atmospheric and Solar-Terrestrial Physics, 145:85–97.

Ballarotti, M. and Saba, M. (2005). High-speed camera observations of negative ground flashes on a millisecond-scale. Geophysical Research Letters.

Bandholnopparat, K., Sato, M., Adachi, T., Ushio, T., and Takahashi, Y. (2019). Optical properties of intracloud and cloud-to-ground discharges derived from jem-glims lightning observations. Journal of Atmospheric and Solar-Terrestrial Physics, 189.

Baumgaertner, A., III, N., Lucas, G., and Thayer, J. (2013). Towards a comprehensive global electric circuit model: Conductivity and its variability in waccm model simulations. Journal of Geophysical Research: Atmospheres, 118:6670–6680.

Berger, K., Anderson, R., and Kröninger, H. (1975). Parameters of lightning flashes. Electra, 80:23–37.

Boccippio, D., L. Cummins, K., Christian, H., and Goodman, S. (1999). Combined satellite and surface-based estimation of the intracloud/ cloud-to-ground lightning ratio over the continental united states. Monthly Weather Review, 129.

Buechler, D., T. Driscoll, K., Goodman, S., and Christian, H. (2000). Lightning activity within a tornadic thunderstorm observed by the optical transient detector (otd). Geophysical Research Letters, 27.

Cecil, D. J., Buechler, D., and Blakeslee, R. (2013). Gridded lightning climatology from trmm-lis and otd: dataset description. Atmospheric Research, s 135–136.

Christian, H., Blakeslee, R., Boccippio, D., Boeck, W., Buechler, D., T. Driscoll, K., Goodman, S., M. Hall, J., J. Koshak, W., and Mach, D. (2003). Global frequency and distribution of lightning as observed from space by the optical transient detector. J. Geophys. Res., 108.

Christian, H., Blakeslee, R., Goodman, S., A. Mach, D., F. Stewart, M., Buechler, D., J. Koshak, W., M. Hall, J., Boeck, W., T. Driscoll, K., and Boccippio, D. (1999). The lightning imaging sensor.

Cummins, K., Cramer, J., Biagi, C., Krider, E., Jerauld, J., Uman, M., and Rakov, V. (2006). The u.s. national lightning detection network: Post-upgrade status. 86th AMS Annual Meeting.

Cummins, K. and Murphy, M. (2009). An overview of lightning locating systems: History, techniques, and data uses, with an in-depth look at the u.s. nldn. Electromagnetic Compatibility, IEEE Transactions on, 51:499 – 518.

Cummins, K., Murphy, M., Bardo, E., W., H., Pyle, R., and A., P. (1998). A combined toa/mdf technology upgrade of the u.s. national lightning detection network. J. Geophys. Res., 103:9038 – 9044.

de Souza, P., Pinto Jr, O., Pinto, I., Ferreira, N., and Frassoni, A. (2009). The intracloud/cloud-to-ground lightning ratio in southeastern brazil. Atmospheric Research, 91:491–499.

Dowden, R., Brundell, J., and Rodger, C. (2002). Vlf lightning location by time of group arrival (toga) at multiple sites. Journal of Atmospheric and Solar-Terrestrial Physics, 64:817–830.

Flaming, G. (2005). Global precipitation measurement update. page 4 pp.

Goodman, S., Buechler, D., Knupp, K., Driscoll, K., and W. McCaul, E. (2000). The 1997–98 el nino event and related wintertime lightning variations in the southeastern united states. Geophysical Research Letters - GEOPHYS RES LETT, 27.

Harrison, R. (2005). The global atmospheric electrical circuit and climate. Surveys in Geophysics, 25.

Harrison, R. (2012). The carnegie curve. Surveys in Geophysics, 34.

Heidler, F., Cvetic, J., and Stanic, B. (1999). Calculation of lightning current parameters. Power Delivery, IEEE Transactions on, 14:399 – 404.

Hou, A., Kakar, R., Neeck, S., Azarbarzin, A., Kummerow, C., Kojima, M., Oki, R., Nakamura, K., and Iguchi, T. (2014). The global precipitation measurement (gpm) mission. Bulletin of the American Meteorological Society, 95:701–722.

Hutchins, M., Holzworth, R., Brundell, J., and Rodger, C. (2012). Relative detection efficiency of the world wide lightning location network. Radio Science, 47.

Ishii, M., Saito, M., Fujii, F., Hojo, J.-I., Matsui, M., Itamoto, N., and Shinjo, K. (2005). Lemp from lightning discharges observed by jldn. Ieej Transactions on Power and Energy, 125:765–770.

Javor, V. (2009). On the choice of the lightning channel current decay constant in the modified transmission line model with exponential decay. Journal of Communications Software and Systems, 5:135.

Kidd, C. and Huffman, G. (2011). Global precipitation measurement. Meteorological Applications, 18:334 – 353.

Koshak, W., Solakiewicz, R., Phanord, D., and Blakeslee, R. (1994). Diffusion model for lightning radiative transfer. J. Geophys. Res., 99.

Koshak, W. J. (2010). Optical characteristics of otd flashes and the implications for flash-type discrimination. Journal of Atmospheric and Oceanic Technology - J ATMOS OCEAN TECHNOL, 27:1822–1838.

Kuleshov, Y., Mackerras, D., and Darveniza, M. (2006). Spatial distribution and frequency of lightning activity and lightning flash density maps for australia. Journal of Geophysical Research, 111.

Legates, D. and Willmott, C. (1990). Mean seasonal and spatial variability in gauge-corrected, global precipitation. International Journal of Climatology, 10:111 – 127.

Lhermitte, R. and Williams, E. (1983). Cloud electrification. Reviews of Geophysics and Space Physics, 21:984–992.

Liu, C., Williams, E., Zipser, E., and Burns, G. (2010). Diurnal variations of global thunderstorms and electrified shower clouds and their contribution to the global electrical circuit. Journal of The Atmospheric Sciences - J ATMOS SCI, 67.

Liu, C., Zipser, E., Cecil, D., Nesbitt, S., and Sherwood, S. (2008). A cloud and precipitation feature database from nine years of trmm observations. Journal of Applied Meteorology and Climatology - J APPL METEOROL CLIMATOL, 47:2712–2728.

López, J. A., Montanyà, J., Van Der Velde, O., Romero, D., Aranguren, H., Torres, H., Taborda, J., and Martinez, J. (2016). First data of the colombia lightning mapping array - colma. In Proceeding of the 33rd International Conference on Lightning Protection, ICLP 2016, Estoril, Portugal.

Lu, G., Cummer, S., Blakeslee, R., Weiss, S., and Beasley, W. (2012). Lightning morphology and impulse charge moment change of high peak current negative strokes. Journal of Geophysical Research (Atmospheres), 117:4212–.

Lyu, F., Cummer, S., Lu, G., Zhou, X., and Weinert, J. (2016). Imaging lightning intra-cloud initial stepped leaders by low-frequency interferometric lightning mapping array: (ic initial leader structure by lfi-lma). Geophysical Research Letters, 43.

Mach, D., Blakeslee, R., and Bateman, M. (2011). Global electric circuit implications of combined aircraft storm electric current measurements and satellite-based diurnal lightning statistics. Journal of Geophysical Research, 116.

Mach, D., Blakeslee, R., Bateman, M., and Bailey, J. (2009). Electric fields, conductivity, and estimated currents from aircraft overflights of electrified clouds. Journal of Geophysical Research, 114.

Mackerras, D. and Darveniza, M. (1994). Latitudinal variation of lightning occurrence characteristics. Journal of Geophysical Research, 991:10813–10822.

Mackerras, D., Darveniza, M., Orville, R., Williams, E., and Goodman, S. (1998). Global lightning: Total, cloud and ground flash estimates. Journal of Geophysical Research, 103:19791–19809.

Makino, M. and Ogawa, T. (1985). Quantitative estimation of global circuit. Journal of Geophysical Research, 90:5961–5966.

Mareev, E. and Volodin, E. (2014). Variation of the global electric circuit and ionospheric potential in a general circulation model. Geophysical Research Letters, 41.

Mareev, E. A., A. Yashunin, S., Davydenko, S., C. Marshall, T., Stolzenburg, M., and R. Maggio, C. (2008). On the role of transient currents in the global electric circuit. Geophysical Research Letters, 35:1–5.

Matsui, M. and Hara, Y. (2011). The number of strokes per flash measured by jldn. pages 248–253.

Matsui, M. and Takano, N. (2010). Evaluation of lightning location accuracy of jldn with a lightning video camera system. In 2010 Asia-Pacific International Symposium on Electromagnetic Compatibility, pages 1142–1145.

Mecikalski, R. M. and Carey, L. (2018). Radar reflectivity and altitude distributions of lightning flashes as a function of three main storm types. Journal of Geophysical Research: Atmospheres, 123.

Michaelides, S., Levizzani, V., Anagnostou, E., Bauer, P., Kasparis, T., and Lane, J. (2009). Precipitation: Measurement, remote sensing, climatology and modeling. Atmospheric Research, 94:512–533.

Minamoto, Y. and Kadokura, A. (2011). Extracting fair-weather data from atmospheric electric-field observations at syowa station, antarctica. Polar Science, 5:313–318.

Nag, A., Mallick, S., Rakov, V., S. Howard, J., Biagi, C., Hill, J., A. Uman, M., M. Jordan, D., Rambo, K., Jerauld, J., A. DeCarlo, B., and Cummins, K. (2011). Evaluation of u.s. national lightning detection network performance characteristics using rocket-triggered lightning data acquired in 2004–2009. Journal of Geophysical Research, 116.

Nag, A., Murphy, M., Cummins, K., E Pifer, A., and Cramer, J. (2014). Recent evolution of the u.s. national lightning detection network.

Nickolaenko, A., Galuk, Y., and Hayakawa, M. (2016). Vertical profile of atmospheric conductivity that matches schumann resonance observations. SpringerPlus, 5.

Nicoll, K. (2012). Measurements of atmospheric electricity aloft. Surveys in Geophysics, 33.

Norville, K., MB, B., and Latham, J. (1991). A numerical study of thunderstorm electrification - model development and case study. Journal of Geophysical Research, 96.

Orville, R. (1980). Daylight spectra of individual lightning flashes in the 370–690 nm region. Journal of Applied Meteorology, 19.

Orville, R. and Henderson, R. (1984). Absolute spectral irradiance measurements of lightning from 375 to 880 nm. Journal of the Atmospheric Sciences, 41.

Orville, R. and Huffines, G. (2001). Cloud-to-ground lightning in the united states: Nldn results in the first decade, 1989 98. Monthly Weather Review - MON WEATHER REV, 129.

Orville, R., Huffines, G., Burrows, W., Holle, R., and Cummins, K. (2001). The north american lightning detection network (naldn)—first results: 1998–2000. AGU Fall Meeting Abstracts, 130:0059–.

Orville, R. E. (1994). Cloud-to-ground lightning flash characteristics in the contiguous united states: 1989–1991. Journal of Geophysical Research: Atmospheres (1984–2012), 99:10 833–10 841.

Ott, L. E., Pickering, K., Stenchikov, G. L., Huntrieser, K., and Schumann, U. (2007). Effects of lightning nox production during the 21 july european light-

ning nitrogen oxides project storm studied with a three-dimensional cloud-scale chemical transport model. J. Geophys. Res., 112.

Pawar, S. and Kamra, A. (2004). Evolution of lightning and the possible initiation/triggering of lightning discharges by the lower positive charge centre in an isolated thundercloud in tropics. Journal of Geophysical Research, 109.

Pickering, K. E., Wang, Y., Tao, W.-K., Price, C., and Müller, J.-F. (1998). Vertical distributions of lightning nox for use in regional and global chemical transport models. Journal of Geophysical Research, 1033:31203–31216.

Pierce, E. T. (1970). Latitudinal variation of lightning parameters. Journal of Applied Meteorology, 9:194.

Pinto, O., Pinto, I., and Faria, H. (2003). A comparative analysis of lightning data from lightning networks and lis sensor in the north and southeast of brazil. Geophysical Research Letters - GEOPHYS RES LETT, 30.

Plooster, M. (1971). Numerical model of the return stroke of the lightning discharge. Physics of Fluids - PHYS FLUIDS, 14:2124–2133.

Prentice, S. A. and MacKerras, D. (1977). The ratio of cloud to cloud-ground lightning flashes in thunderstorms. Journal of Applied Meteorology - J APPL METEOROL, 16:545–550.

Quick, M. and Krider, E. (2013). Optical power and energy radiated by natural lightning. Journal of Geophysical Research: Atmospheres, 118.

Rakov, V., A. Uman, M., and P. Raizer, Y. (2004). Lightning: Physics and effects. Physics Today - PHYS TODAY, 57:63–64.

Rivas Soriano, L. and Dávila, F. (2007). Total flash density and the intracloud/cloud-to-ground lightning ratio over the iberian peninsula. Journal of Geophysical Research, 112.

Rodger, C., Brundell, J., Holzworth, R., and Lay, E. (2009). Growing detection efficiency of the world wide lightning location network. AIP Conf. Proc., 1118.

Roy, S. and Balling, R. (2013). Diurnal patterns in lightning activity in northern tropical africa. Physical Geography, 34:75–84.

Rust, W., MacGorman, D., and Arnold, R. (1981). Positive cloud-to-ground lightning flashes in severe storms. Geophysical Research Letters, 8.

Rycroft, M., Israelsson, S., and Price, C. (2000). The global atmospheric electric circuit, solar activity and climate change. Journal of Atmospheric and Solar-Terrestrial Physics, 62:1563–1576.

Rycroft, M. and Odzimek, A. (2010). Effects of lightning and sprites on the ionospheric potential, and threshold effects on sprite initiation, obtained using an analog model of the global atmospheric electric circuit. Journal of Geophysical Research, 115.

Rycroft, M., Odzimek, A., Arnold, N., Füllekrug, M., Kulak, A., and Neubert, T. (2007). New model simulations of the global atmospheric electric circuit driven by thunderstorms and electrified shower clouds: The roles of lightning and sprites. Journal of Atmospheric and Solar-terrestrial Physics - J ATMOS SOL-TERR PHYS, 69:2485–2509.

Sato, M. (2015). Overview and early results of the global lightning and sprite measurements mission. J. Geophys. Res. Atmos.

Sato, M., Fukunishi, H., Kikuchi, M., Yamagishi, H., and Lyons, W. (2003). Validation of sprite-inducing cloud-to-ground lightning based on elf observations at syowa station in antarctica. Journal of Atmospheric and Solar-Terrestrial Physics, 65:607–614.

Sato, M., Mihara, M., Adachi, T., Ushio, T., Morimoto, T., Kikuchi, M., Kikuchi, H., Suzuki, M., Yamazaki, A., Takahashi, Y., Inan, U., Linscott, I., Ishida, R.,

Sakamoto, Y., Yoshida, K., and Hobara, Y. (2016). Horizontal distributions of sprites derived from the jem-glims nadir observations. Journal of Geophysical Research: Atmospheres, 121:n/a–n/a.

Sato, M., Takahashi, Y., Kikuchi, M., Suzuki, M., Yamazaki, A., and Ushio, T. (2011a). Lightning and sprite imager (lsi) onboard jem-glims. IEEJ Transactions on Fundamentals and Materials, 131:994–999.

Sato, M., Takahashi, Y., Suzuki, M., Yamazaki, A., and Ushio, T. (2011b). Six-channel spectrophotometers (ph) onboard jem-glims. IEEJ Transactions on Fundamentals and Materials, 131:1000–1005.

Shindo, T. and Yokoyama, S. (1998). Lightning occurrence data observed with lightning location systems in japan: 1992-1995. Power Delivery, IEEE Transactions on, 13:1468 – 1474.

Soula, S. and Chauzy, S. (1997). Charge transfer by precipitation between thundercloud and ground. Journal of Geophysical Research, 1021:11061–11070.

Stolzenburg, M., Rust, W., and Marshall, T. (1998a). Electrical structure in thunderstorm convective regions 2. isolated storms. Journal of Geophysical Research, 1031:14079–14096.

Stolzenburg, M., Rust, W., and Marshall, T. (1998b). Electrical structure in thunderstorm convective regions 3. synthesis. Journal of Geophysical Research, 103:14097–14108.

Stolzenburg, M., Rust, W., Smull, B., and Marshall, T. (1998c). Electrical structure in thunderstorm convective regions 1. mesoscale convective systems. Journal of Geophysical Research, 1031:14059–14078.

Sun, Z., Qie, X., Liu, M., Jiang, R., Wang, Z., and Zhang, H. (2016). Characteristics of a negative lightning with multiple-groundterminations observed by a

vhf lightninglocation system. Journal of Geophysical Research (Atmospheres), 121:413–426.

Takahashi, T. (1984). Thunderstorm electrification–a numerical study. Journal of The Atmospheric Sciences - J ATMOS SCI, 41:2541–2558.

Velinov, P., Asenovksi, S., Kudela, K., Laštovička, J., Mateev, L., Mishev, A., and Tonev, P. (2013). Impact of cosmic rays and solar energetic particles on the earth's ionosphere and atmosphere. Journal of Space Weather and Space Climate, 3:14–.

Williams, E. (2009). The global electrical circuit: A review. Atmospheric Research, 91:140–152.

Williams, E., Boldi, B., Matlin, A., Weber, M., Hodanish, S., Sharp, D., Goodman, S., Raghavan, R., and Buechler, D. (1999). The behavior of total lightning activity in severe florida thunderstorms. Atmospheric Research, 51:245–265.

Williams, E., Zhang, R., and Rydock, J. (1991). Mixed-phase microphysics and cloud electrification. Journal of The Atmospheric Sciences - J ATMOS SCI, 48:2195–2203.

Williams, E. K., Rothkin, K., Stevenson, D., and Boccippio, D. (2000). Global lightning variations caused by changes in thunderstorm flash rate and by changes in number of thunderstorms. Journal of Applied Meteorology, 39.

Wilson, C. T. R. (1921). Investigations on lightning discharges and on the electric field of thunderstorms. Monthly Weather Review - MON WEATHER REV, 49.

Zhang, D., Cummins, K., Nag, A., Murphy, M., and Bitzer, P. (2016). Evaluation of the national lightning detection network upgrade using the lightning imaging sensor.

Zipser, E. (1994). Deep cumulonimbus cloud systems in the tropics with and without lightning. Monthly Weather Review, 122.

Zipser, E. and Lutz, K. (1994). The vertical profile of radar reflectivity of convective cells: A strong indicator of storm intensity and lightning probability? Monthly Weather Review, 122.